ABSTRACT

Title of dissertation: SIMULATIONS OF NONUNIFORM FLUIDS WITH LONG-RANGED AND SHORT-RANGED INTERACTIONS

Shule Liu, Doctor of Philosophy, 2012

Dissertation directed by: Professor John D. Weeks
Department of Chemistry and Biochemistry
Institute for Physical Science and Technology

The study of nonuniform fluids is of great importance in many areas of chemistry, biophysics, and materials science. Computer simulations of model systems have provided great insight into fundamental physical issues. We have studied two model systems: amphiphiles on a hydrophilic silica surface and charge overcompensation at the boundary of a colloid by multivalent ions. In the first model system, the organization of propionitrile and methanol near the surface has been studied via simulations. Both molecules can form highly organized bilayer-like structure near the surface. For propionitrile molecules, inside the bilayer-like structure hydrocarbon molecules intertwine with each other and form a closely packed structure. For methanol, molecules are strongly bonded to the silica surface with hydrogen bonds, resulting in much stronger hydrogen bonding than in the bulk and extremely slow dynamics.

In our second model system, we use the local molecular field (LMF) theory to calculate the structure and solvation free energy of the system with a highly

charged colloid immersed in trivalent salt. A mimic system with only short-ranged interactions was constructed using the LMF theory. By solving the LMF equation self-consistently, we have obtained the correct structure that indicates overcharging, where the charge of the colloid is overcompensated by the charge of trivalent ions. Then by taking a series of steps in a thermodynamic cycle, we have also calculated the solvation free energy of the colloid, using only results from the mimic system, and found very good agreement with more costly calculations carried out in the full long-ranged system.

SIMULATIONS OF NONUNIFORM FLUIDS WITH LONG-RANGED AND SHORT-RANGED INTERACTIONS

by

Shule Liu

Dissertation submitted to the Faculty of the Graduate School of the
University of Maryland, College Park in partial fulfillment
of the requirements for the degree of
Doctor of Philosophy
2012

Advisory Committee:
Professor John D. Weeks, Chair/Advisor
Professor Millard Alexander
Professor Christopher Jarzynski
Professor Devarajan Thirumalai
Professor Sergei Sukharev, Dean's Representative

Dedication

To my parents, for their support during all these years.

Acknowledgments

First, I would like to thank my advisor, Professor John Weeks, for his guidance during the past five years and for his help and suggestions on this thesis. It was from John's class that I first learned basic theories and simulations of liquids, a complicated but interesting area that I would still like to keep studying. John is very helpful and patient with my research all the time and he is always an optimist. What I learned from John during the past five years are not only knowledge in liquid theory, but also his attitude toward research, teaching, and etc.

I would also like to thank Professor Millard Alexander and Professor Christopher Jarzynski, for their inspiring and insightful courses, which serve as a solid foundation for my current and future research. Special thanks also goes to Professor Sergei Sukharev and Professor Devarajan Thirumalai for serving in the committee and reviewing this thesis. Your comments and suggestions are appreciated.

I am also grateful to Professor John Fourkas and Professor Robert Walker, for their helpful discussions and guidance in the CRC project during the past several years. It was from them I got to know the powerfulness of nonlinear spectroscopy and how simulations are closely related to experiments.

It was really lucky for me to be in a research group with lots of talented people. I owe a lot to past and current Weeks group members. I would like show my gratitude to Dr. Jocelyn Rodgers, Dr. Zhonghan Hu and Dr. Natalia Denesyuk. Without their previous excellent work all the stuff in this thesis would not exist. I also acknowledge Dr. Qiang Liu for helping me a lot on computational issues. I

am very grateful to Mr. Richard Remsing, from whom I really learned a lot. His diligence and enthusiasm in research always inspire me.

Finally, I would like to thank my parents, for their consistent support for me during all these years.

Table of Contents

List of Figures vii

List of Tables ix

List of Abbreviations x

1 Introduction 1
1.1 Overview . . . 1
1.2 Outline of the Dissertation . . . 7

2 Propionitrile near Hydrophilic Silica Wall 11
2.1 Introduction . . . 11
2.2 Simulation Details . . . 12
2.3 Singlet Densities . . . 15
2.4 Molecular Orientations . . . 19
2.4.1 CN Vector Orientations . . . 19
2.4.2 CT-C Vector Orientations . . . 24
2.4.3 Packing of the Hydrocarbon Groups . . . 26
2.5 Electrostatics . . . 29
2.6 Summary and Conclusions . . . 32

3 Methanol Near Hydrophilic Silica Wall 34
3.1 Introduction . . . 34
3.2 Simulation Details . . . 35
3.3 Density Profiles . . . 36
3.4 Molecular Orientation . . . 38
3.5 Hydrogen Bonds and Dynamics . . . 41
3.6 Electrostatics . . . 49
3.7 Summary and Conclusions . . . 50

4 LMF Treatment of Charge Inversion System: Structure 52
4.1 Local Molecular Field Theory for Electrostatic Interactions . . . 52
4.2 The Charge Inversion Phenomenon . . . 55
4.3 Simulation Details . . . 58
4.4 Results from Ewald Summation . . . 60
4.5 Strong-coupling Approximation . . . 62
4.6 Full Solution to the LMF Equation . . . 64
4.6.1 Solving LMF Equation via Simulations . . . 67
4.6.2 Solving LMF Equation via Linear Response . . . 71
4.6.3 The Choice of σ and Separation of Coulomb Potential . . . 75
4.7 Summary and Conclusions . . . 79

5 LMF Treatment of Charge Inversion System: Solvation Free Energy 80
5.1 Overview of The Solvation Free Energy Calculation Process 80
5.2 Derivation of ΔG_{LMF} Using LMF Theory 82
5.3 Calculating the Solvation Free Energy in Practice 88
5.3.1 The Free Energy of Inserting a Repulsive Sphere: ΔG_{HS} and $\Delta G_{R,HS}$ 88
5.3.2 Solvation Free Energy of Charging 90
5.3.3 $\Delta G_{\phi_{R1}}$, ΔG_{LMF} and $\Delta G_{R,sol}$ 95
5.4 The Charging Free Energy's Quadratic Dependence on the Colloid Charge 97
5.5 Summary and Conclusions 99

6 Conclusions and Future Work 102

A Stable k-space solution of LMF equation 106

Bibliography 109

List of Figures

1.1 Figure of Acetonitrile, Propionitrile and Methanol Molecule 3
1.2 Comparison of lattice sums and LMF treatment for Electrostatic Interactions 6

2.1 The Propionitrile Molecule and a Snapshot of the Model System . . . 13
2.2 Propionitrile Density 16
2.3 Arrow Plots of Propionitrile 17
2.4 Schematic plot showing the typical orientation of acetonitrile and propionitrile at the silica surface 18
2.5 Contour map plot of propionitrile joint distribution function 20
2.6 Contour plot of the radial/angular distribution function $g(r, \theta)$ in the LS, bulk and LV regions. 23
2.7 Contour map plot of propionitrile joint distribution function for CT-C vectors 25
2.8 Comparison of the CN density in acetonitrile and propionitrile, where z is the center of the CN bond. The density is normalized by the bulk density ρ_B. 26
2.9 2-D radial distribution function $g(r)$, where r is distance between CT-C bond center on the xy plane. 27
2.10 Contour Map plot 28
2.11 Comparison of the CN bond orientational TCF in the LS region for both acetonitrile (blue) and propionitrile (red). 29
2.12 Charge densities of propionitrile 31

3.1 Methanol Atom Density 37
3.2 Center of mass density of methanol and acetonitrile 39
3.3 Orientational Distribution of Methanol O-C Vector 40
3.4 Orientational Distribution of Methanol O-H Vector 41
3.5 Arrow plots of Methanol near Silica Surface 42
3.6 A Schematic Plot of Hydrogen Bond Chain in Bulk Methanol 42
3.7 Number of hydrogen bond per molecule as a function as distance away from the silica surface. 44
3.8 Visualization of hydrogen bonding at liquid/solid interface and in bulk methanol 45
3.9 Orientational time-correlation functions for methanol O-H and O-C bonds 47
3.10 Hydrogen bond TCFs in LS (red), bulk (green) and LV (blue) regions 49
3.11 Charge Density of Methanol and Acetonitrile 50

4.1 Demonstration of $1/r$ potential split with $\sigma = 1$. 53
4.2 Schematic drawing of the model system 56
4.3 Density profiles for the full system with Ewald summation 61
4.4 Density profiles for the mimic system with SCA and full LMF solution 65

4.5 Illustration of SCA's failure to get neutrality 66
4.6 The integrated charge of Ewald (blue) and LMF runs with the same $\mathcal{V}_R$ but different initial configuration (red).Greater fluctuations in the LMF system is visible. 69
4.7 Probability distribution of Φ_{R1} in Ewald (red) and LMF (green) configurations 70
4.8 Results of linear response iteration for $\sigma = 26.828\mathring{A}$ 74
4.9 Results of linear response iteration for $\sigma = 21.462\mathring{A}$ 76
4.10 Results for mimic system with external charges placed at the center of the colloid 78

5.1 Illustration of the solvation free energy calculation process in the full system 81
5.2 Illustration of the solvation free energy calculation process in the mimic system 82
5.3 Probability distribution of ΔU in Ewald and SCA charging process . 94
5.4 ΔG_{charge} as a function of the colloid charge Q 98
5.5 ΔG_{LMF} as a function of the colloid charge Q 100
5.6 $\Delta G_{\phi_{R1}}$ as a function of the colloid charge Q 100
5.7 $\Delta G_{\text{R,charge}}$ as a function of the colloid charge Q 101

List of Tables

2.1 OPLS-AA nonbonding parameters. 15
2.2 Silica nonbonding parameters. 15

3.1 OPLS-AA parameters for intermolecular interactions between methanol molecules. 36
3.2 Average number of molecules in the LS region and its sublayers for acetonitrile and methanol. 38
3.3 Estimated H-bond lifetime τ_{HB} for different regions 48

5.1 Components of $\Delta G_{R,sol}$ together with ΔG_{LMF}, in unit of k_BT. 96
5.2 Components of ΔG_{sol} in the full system, in unit of k_BT. 96

List of Abbreviations

BAR	Bennett Acceptance Ratio
EDL	Electrical Double Layer
FEP	Free Energy Perturbation
H-bond	Hydrogen Bond
HPLC	High-performance liquid chromatography
LMF	Local Molecular Field
LR	Linear Response
LS	Liquid-solid
LV	Liquid-vapor
MC	Monte Carlo
MD	Molecular Dynamics
μVT	Grand canonical ensemble
NPT	Isothermal-isobaric ensemble
NVT	Canonical ensemble
OCP	One-component plasma
OKE	Optical Kerr Effect
OPLS-AA	OPLS all-atom
PB	Poisson-Boltzmann
SCA	Strong-coupling Approximation
SHG	Second Harmonic Generation
TI	Thermodynamic Integration
TCF	Time-correlation Function
VSFG	Vibrational Sum-frequency Generation
WC	Wigner-Crystal
WCA	Weeks-Chandler-Andersen
YBG	Yvon-Born-Green

Chapter 1

Introduction

1.1 Overview

The study of non-uniform liquids has a broad application in physics, chemistry and biology. Using the principles of statistical mechanics and molecular simulations, various properties of non-uniform liquids can be extracted. In this thesis, we will focus on two areas of non-uniform liquids.

A. Amphiphiles at Hydrophilic Silica Surfaces

The interfacial organization and dynamics of polar molecular liquids play an important role in chemical and biological systems. Amphiphiles, such as alkyl cyanide and alcohols, feature a polar group and a nonpolar alkyl tail. These species are commonly used as solvents, and changing the tail length alters the relative influence of the polar and nonpolar groups on chemical structure and dynamics[1–12]. At hydrophilic surfaces, the polar groups of amphiphiles can interact strongly with surface charges and can accept hydrogen bonds, while the nonpolar groups present mainly an excluded volume region with weak Van der Waals attractions. An understanding of the detailed arrangements of different amphiphilic liquids at a hydrophilic silica surface can provide important information about physical and chemical properties that are relevant to catalysis, separations, and other chemical

processes.

Recently, the structure of acetonitrile (CH_3CN), the simplest alkyl cyanide, has been studied extensively both by experiment[6, 7, 13, 14] and simulation[15–19] at a hydrophilic silica surface and at its liquid-vapor interface. Acetonitrile has a highly polar cyanide group (CN) and a nonpolar methyl group (CH_3) and in bulk phase acetonitrile molecules have a tendency to choose antiparallel dipole pairing[20, 21]. However, at the hydrophilic surface such ordering of acetonitrile breaks down due to strong interactions with the surface. It has been observed both in experiments and simulations that at hydrophilic silica surface acetonitrile forms highly organized bilayer-like structure with molecules in the first sublayer pointing their cyanide groups toward the silica surface and second sublayer pointing their cyanide groups away from the silica surface. Moreover, the inhomogeneity induced by the silica wall can extend more than 30 Å into the bulk.

In this thesis, we will focus on the study of propionitrile (CH_3CH_2CN) and methanol (CH_3OH) at a hydrophilic silica surface. Our simulations studies are combined with nonlinear optical studies of the interface, such as vibrational sum-frequency generation (VSFG) and optical Kerr effect (OKE)[22]. Both molecules can be derived from the structure of acetonitrile by adding or replacing certain functional groups(Fig. 1.1): Propionitrile is obtained by adding a methylene (CH_2) group to acetonitrile and it has larger excluded volume; Methanol is obtained by replacing the cyanide group with a hydroxyl group and this enables methanol to serve as both a hydrogen bond donor and acceptor. By doing this we could study the influence of different functional groups on the organization of amphiphiles near

a hydrophilic surface. Moreover, acetonitrile is commonly used as the mobile phase in high-performance liquid chromatography (HPLC). In the year 2008 there was a worldwide shortage of acetonitrile[23] and people are trying hard to find suitable alternatives to acetonitrile. Therefore, the study of propionitrile and methanol at silica surface might provide insight in finding alternatives to acetonitrile.

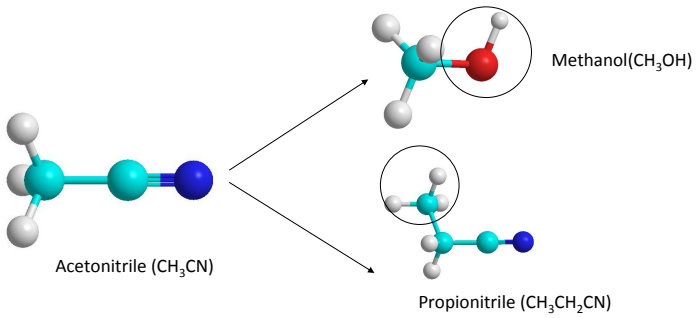

Figure 1.1: Acetonitrile, propionitrile and methanol molecule. White: hydrogen; Cyan: carbon; Red: oxygen; Blue: nitrogen. The hydroxyl group in methanol and methyl group in propionitrile are circled in order to show their difference from acetonitrile.

B. Local Molecular Field Theory

The Local Molecular Field (LMF) theory developed by Weeks and coworkers [24–30] is a mean-field based approach that has been successfully applied to a variety of systems. The theory is based on the idea that the original system (full system) of interest with long-ranged interactions can be mapped onto a simpler mimic system with only the short-ranged part of the particle-particle interactions of the original

system, but which has similar structural properties.

$$\begin{array}{ccc} \text{Full} & & \text{Mimic} \\ \left\{ \begin{array}{c} w(r) \\ \\ \phi(\mathbf{r}) \end{array} \right\} & \xrightarrow{\text{LMF}} & \left\{ \begin{array}{c} u_0(r) \\ \\ \phi_R(\mathbf{r}) \end{array} \right\}. \end{array} \tag{1.1}$$

To be more explicit, consider a nonuniform system with long-ranged intermolecular interactions $w(r)$ in an external field $\phi(r)$, which can represent the interactions with fixed objects such as walls or solutes. The LMF theory asserts that with a suitable choice of short-ranged interaction $u_0(r)$ and a renormalized external potential $\phi_R(\mathbf{r})$, the nonuniform density of the short-ranged mimic system (denoted by the subscript R) can be made equal to that of the original system, i.e.

$$\rho_R(\mathbf{r}; [\phi_R]) = \rho(\mathbf{r}; [\phi]). \tag{1.2}$$

Here both $\rho(\mathbf{r})$ and $\rho_R(\mathbf{r})$ have implicit dependence on the external field. Moreover, thermodynamic properties of the original system can also be determined from those of the mimic system[31].

An explicit equation for $\phi_R(\mathbf{r})$ can be derived by subtracting the first equations of the exact Yvon-Born-Green (YBG) hierarchy that relate the gradient of singlet density to forces in the full and mimic systems. As argued in Refs. [26, 27, 32], when $u_1(r) \equiv w(r) - u_0(r)$ is chosen to be slowly varying over the typical distances between neighboring molecules, the renormalized external field $\phi_R(\mathbf{r})$ can be accurately determined by integrating the YBG equation, taking advantage of the slowly

varying nature of the $u_1(r)$. The result is the self-consistent LMF equation

$$\phi_R(\mathbf{r}) = \phi(\mathbf{r}) + \int d\mathbf{r}' \rho_R(\mathbf{r}'; [\phi_R]) u_1(|\mathbf{r}' - \mathbf{r}|) + C, \tag{1.3}$$

where C is a constant of integration. Note that this has the form of a simple mean field approximation, but it is derived using physically motivated and controlled approximations about the nature of intermolecular forces.

LMF theory was first devised for treatment of Lennard-Jones interactions and proved to be successful [33–35], but then it is found to be even more powerful when dealing with Coulomb interactions, whose long-ranged behavior has caused many problems in computer simulations. In molecular simulations with periodic boundary conditions, applying minimum image conventions to Coulomb interactions is known to be inaccurate and some lattice sums technique, such as Ewald summation[36], is needed. For lattice sums, the electrostatic interaction between the center cell and all its periodic images must be calculated, as shown schematically in Fig. 1.2(a), and this would greatly boost the computational cost. For direct Ewald sums, the computational cost usually scales as $\mathcal{O}(N^2)$[37], where N is the total number of particles in the system, while for LMF treatment of electrostatic interactions, because the full system with long-ranged interactions is mapped to the mimic system with short-ranged system, minimum image convention can be applied to the system, as shown schematically in Fig. 1.2(b), and this reduces the computational cost to $\mathcal{O}(N)$.

The idea of separating the Coulomb potential into short-ranged and long-

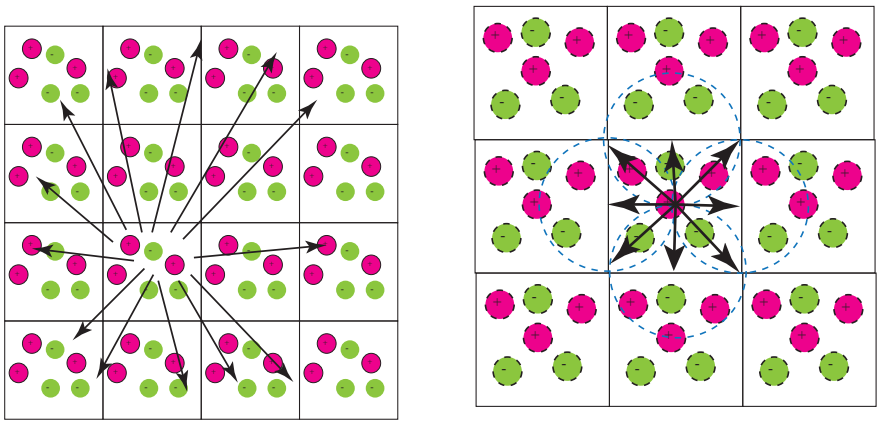

(a) (b)

Figure 1.2: (a) Schematic plot of lattice sums for calculation of electrostatic interactions using periodic boundary condition in the full system: The electrostatic interaction between the main simulation box and all its periodic images must be calculated. (b) Schematic plot of applying minimum image convention for simulation in the mimic system constructed based on LMF theory: The main simulation box only has to interact with its neighboring periodic images. All the particles are drawn with dashed lines to represent short-ranged pair interactions. Circles suggest that half simulation box length is chosen as the cutoff radius.

ranged parts enables LMF theory to capture the short-ranged electrostatic correlations in a convenient way, which has triggered lots of interesting problems in both physics and biology, such as attractions between two like-charged plates mediated by counterions[38–40] and mobility reversal of highly charged colloids in salt solutions[41, 42]. All these phenomena can be ascribed to the electrostatic correlations between counterions near a highly oppositely charged surface: due to the strong counterion-counterion and counterion-surface interactions, counterions do not distribute randomly over the space, but form highly ordered structure on the charged surface[43, 44]. This strong electrostatic correlation cannot be captured by conventional mean-field method such as the Poisson-Boltzmann (PB) equation[43, 44]. However, the mean-field based LMF theory can handle this correctly by incorpo-

rating short-ranged correlations in the mimic system. Recently, the LMF theory has been successfully applied to the system with two like-charged walls mediated by counterions[26, 27], where the LMF treatment could yield the attractions between two walls correctly. In this thesis, we will use LMF theory to tackle the problem of charge inversion, where multivalent counterions can locally overcompensate the charge of a highly-charged solute. We will show that LMF can not only get the structure correct, but also yield accurate results in the calculation of solvation free energy.

1.2 Outline of the Dissertation

This thesis can be divided into two parts. The first part, including Chapter 2 and Chapter 3, discusses the structure and dynamics of amphiphiles (propionitrile and methanol) near a hydrophilic silica wall and at the liquid/vapor interface. The work in Chapter 2, simulation of propionitrile near a silica wall, is an extension of previous work on acetonitrile[1, 5]: By adding an additional methylene group to the acetonitrile molecule, we would expect to see a different organization at the silica wall. For the propionitrile/silica system, first we analyzed the molecule densities and orientation of polar CN groups exactly in the same way as was done for acetonitrile/silica system. We again found a bilayer-like structure like that found at acetonitrile/silica interface, with opposite CN group orientations in two sublayers. This again shows that the structure of propionitrile at silica surface is dominated by the dipole-dipole interactions and the dipole-surface interactions. Then we studied

the organization of nonpolar alkyl groups. Combining the orientation of methyl-methylene bond vectors with the probability distribution of methylene carbon's projection on the surface, we find that hydrocarbon groups in both sublayers form a highly intertwined structure, which is similar to the interdigitation of methyl groups for acetonitrile/silica interface, but the hydrocarbon groups at propionitrile/silica interface are more tightly bound. As a result, compared with acetonitrile, the CN bonds in the sublayer closest to the silica wall are more parallel to the silica wall, and the CN bond reorientation dynamics at the propionitrile/silica interface is even slower. In the last section, we briefly describe the charge density of the system and use the Gaussian-smoothed charge density as a tool to explore the dipole layering at liquid/solid and liquid/vapor interfaces.

Chapter 3 gives the analysis of methanol/silica interface. We extend methods earlier used for acetonitrile to study the arrangement of methanol molecules near silica wall. Surprisingly, even though methanol exhibits bilayer-like structure near the silica surface, the density in the second sublayer is extremely low, while correspondingly this results in a very high density in the first sublayer. Orientational analysis shows that in the sublayer closest to the silica surface, methanol molecules point their methyl groups perpendicular to the silica surface and the silica surface together with this tightly absorbed sublayer of methanol molecules actually transforms the originally polar surface into a nonpolar surface. Therefore, both density and orientation analysis suggest the existence of strong hydrogen bonding between methanol and surface silanol groups. To characterize the hydrogen bonding we calculated the number we have calculated number of hydrogen bonds (H-bonds) per

molecule, orientational time-correlation functions (TCFs) and H-bond TCFs. All the analysis indicates that at the methanol/silica surface each methanol molecule on average can participate in more than two H-bonds. These H-bonds are very difficult to break and their lifetime can last for tens of picoseconds. Finally we considered electrostatic effects and showed how the dipole field of the silica surface is effectively screened by the surface layer of methanol.

The second part of the thesis includes Chapter 4 and Chapter 5. It discusses the application of LMF theory to a model system that exhibits charge inversion. Chapter 4 mainly discusses solving the LMF equation for the model system. A brief description of the LMF equation in systems with long-ranged Coulomb potential is given first. Then we discuss the phenomenon of charge inversion, where the charge of a colloid is overcompensated by multivalent counterions around it. The charge inversion arises from strong counterion-counterion and counterion-colloid correlations, which mean-field theories such as Poisson-Boltzmann (PB) cannot account for. We started by solving the LMF equation for the model system with the strong-coupling approximation (SCA), where only the short-ranged part of the external field was taken into account. Because SCA includes correlations between nearest neighbors, the simulation based on it has successfully showed a region with charge reversal near the colloid. However, SCA failed to keep track of the neutrality of the system since it has omitted long-ranged interactions. Based on simulations of SCA, we iterated the self-consistent LMF equation using both simulations and a highly efficient linear response method, and both methods give accurate results on the charge density and neutrality is also attained.

Chapter 5 is about calculating the solvation free energy of the full system using simulations in the mimic system. Using the LMF theory, we obtained a good approximation to the free energy difference between the mimic system and full system. Then the solvation free energy calculation of the colloid in our charge inversion model system was calculated, by decomposing the solvation free energy into different parts. The solvation free energy obtained from mimic system with LMF theory is in good agreement with that obtained in the full system using Ewald summation, but the calculation in the short-ranged mimic system is less computationally expensive.

Chapter 2

Propionitrile near Hydrophilic Silica Wall

The material in this chapter heavily depends on the paper "Structure of Liquid Propionitrile at Interfaces. 1. Molecular Dynamics Simulations" by Liu, Hu, Weeks and Fourkas [45].

2.1 Introduction

Recent work at the University of Maryland reported a combination of molecular dynamics (MD) simulations and vibrational sum-frequency generation (VSFG) spectroscopy experiments that revealed detailed structural information regarding acetonitrile at a hydrophilic silica surface [1, 5]. Those simulations showed that at a planar silica surface acetonitrile takes on a lipid-bilayer-like structure consisting of two sublayers with opposite dipole orientations. Surprisingly, signatures of this bilayer structure propagate for more than 20 Å from the silica surface.

In this chapter we focus on the next member of this family of molecules, propionitrile (ethyl cyanide, CH_3CH_2CN). Propionitrile has an extra methylene group as compared with acetonitrile, and the methyl group in propionitrile is angled away from the CN head orientation. These structural features increase the volume and change the shape of the nonpolar region of the molecule, which is expected to influence the intermolecular ordering of propionitrile at interfaces. To address this issue,

we have performed MD simulations to study the structure of liquid propionitrile at a planar silica surface and at its liquid/vapor interface. The simulation study is combined with VSFG and optical Kerr effect (OKE) spectroscopy[22].

Characterizing the various arrangements and orientations of an extended asymmetric molecule such as propionitrile in a condensed phase is a challenging task. Full multi-dimensional molecular distribution functions describing all intra and intermolecular correlations are difficult to determine, and the interplay among the many degrees of freedom hinders the development of a simple physical picture. Here we approach this problem by considering several reduced distribution functions involving only one or two scalar variables describing the positions and orientations of various parts of the propionitrile molecule. As we will see below, when these distribution functions are well chosen we can gain considerable insight into many features of the nonuniform liquid structure.

2.2 Simulation Details

We follow the approach of Hu *et al.* [5], in which the silica force field is constructed using a four-layer silica surface with an idealized β-cristobalite (C9) crystal structure [46]. The silica surface is terminated with hydroxyl groups to make it hydrophilic and the hydroxyl density is $4.54/\text{nm}^2$. A snapshot of the silica surface is given in Fig. 2.1(b). The system consists of 960 propionitrile molecules with the hydrophilic silica wall's top oxygen layer placed at $z = 0$ and a repulsive wall placed at $z = 100$ Å. Periodic boundary conditions were employed with $L_x = 45.60$ Å,

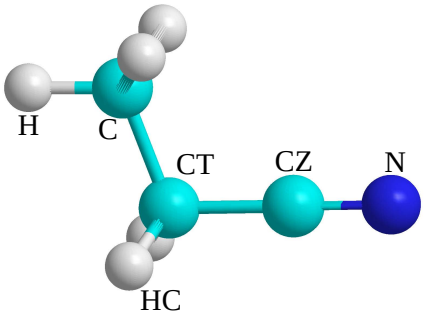

(a)

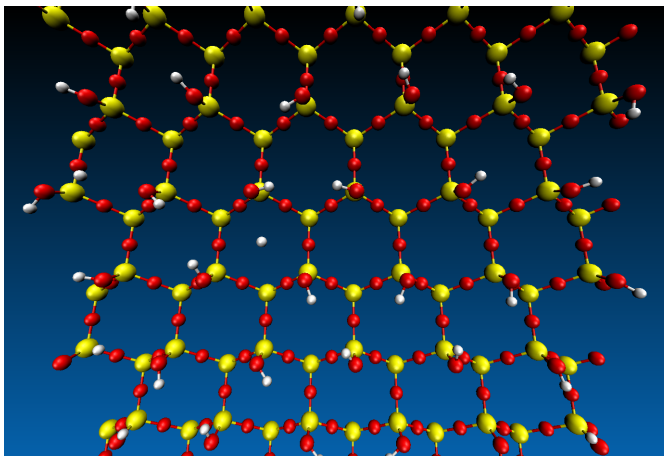

(b)

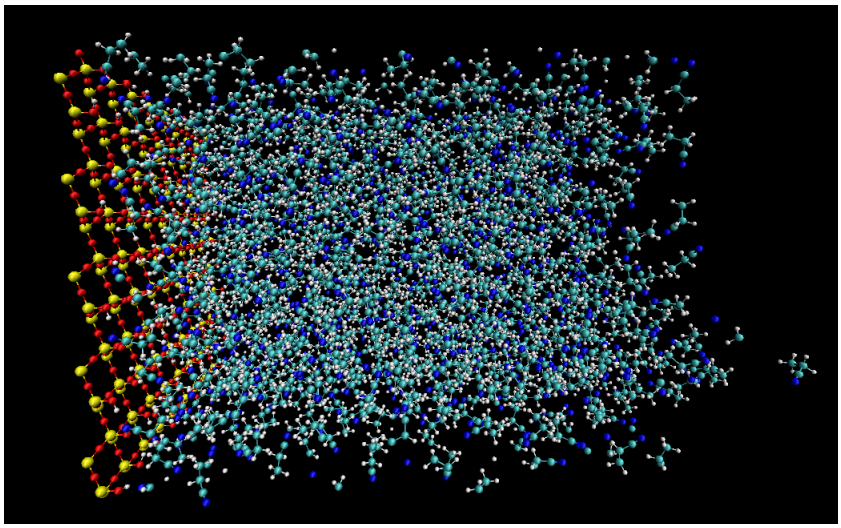

(c)

Figure 2.1: (a) The structure of the propionitrile molecule and the notations used here for its atoms. (b) A snapshot of the silica surface terminated with hydroxyl groups. Yellow: silicon; Red: oxygen; White: hydrogen. (c) A snapshot of the model system, where the silica surface is placed at the left side of the figure.

L_y = 43.88 Å and L_z = 200 Å. Slab-corrected Ewald 3D sums [47] were used for treatment of electrostatic interactions in our system. The screening parameter for the Ewald summation is 0.26 $Å^{-1}$, and the numbers of k-space vectors for the Ewald summation were 15, 15 and 45 for x, y and z directions, respectively. The cutoff distances for the Van der Waals and the short-ranged part of the corrected Ewald summation were both 15 Å. A snapshot of our model system is given in Fig. 2.1(c).

Parameters from the OPLS all-atom (OPLS-AA) model [48] were used to describe the intramolecular interactions and the interactions among propionitrile molecules. OPLS-AA nonbonding parameters for propionitrile are given in Table 2.1. We use the notations "N" for the nitrogen atom, "CZ" for the carbon atom in the nitrile group, "CT" for the methylene carbon, "HC" for the hydrogen atoms in the methylene group, "C" for the methyl carbon and "H" for the hydrogen atoms in the methyl group. A schematic structure of a propionitrile molecule with the notations for the atoms is shown in Fig. 2.1(a). We have also listed the nonbonding parameters for the atoms that make up the silica surface in Table 2.2. For Lennard-Jones interactions between propionitrile molecules, we used the OPLS combining rules $\sigma_{ij} = \sqrt{\sigma_i \sigma_j}$ and $\epsilon_{ij} = \sqrt{\epsilon_i \epsilon_j}$. For Lennard-Jones interactions between propionitrile and atoms on the silica wall, the Lorentz-Berthelot mixing rules $\sigma_{ij} = (\sigma_i + \sigma_j)/2$ and $\epsilon_{ij} = \sqrt{\epsilon_i \epsilon_j}$ were used . MD simulations in the NVT ensemble were performed using the DL_POLY 2.18 [49] package with a time step of 1 fs. After the system had been equilibrated at T=298K for 300 ps, configurations of the system were recorded every 15 fs. The total sampling lasted for 450,000 steps and gave a trajectory file with a total of 30,000 configurations for analysis.

Atom	q (e_0)	ϵ_{LJ} (kcal/mol)	σ_{LJ} (Å)
N	-0.56	0.170	3.20
CZ	0.46	0.063	3.30
CT	-0.02	0.063	3.30
HC	0.06	0.015	2.50
C	-0.18	0.063	3.50
H	0.06	0.030	2.50

Table 2.1: OPLS-AA nonbonding parameters.

Atom	q (e_0)	ϵ_{LJ} (kcal/mol)	σ_{LJ} (Å)
H(surface)	0.40	...	...
O(surface)	-0.71	0.1544	3.154
Si(surface)	0.31	0.1270	3.795
O(wall)	...	0.1544	3.154
Si(wall)	...	0.1270	3.795

Table 2.2: Silica nonbonding parameters.

2.3 Singlet Densities

In Fig. 2.2 we show the singlet densities arising from three different definitions of molecular positions: the center of mass (cm), the center of the CN bond (z_{CN}) and the center of the CT-C bond (z_{CC}). Molecular densities defined by bond centers can be related to molecular orientations, as we will discuss below. All curves show high peaks near the silica surface, consistent with strong polar interactions between the hydrophilic silica surface and the first layer of propionitrile.

Based on the peaks in the CN bond-center density profiles we define the first layer of the liquid-solid (LS) interface as extending from 0 to 4.9 Å. This first layer can be divided further into two sublayers at 2.5 Å (first sublayer: $0 < z < 2.5$ Å; second sublayer 2.5 Å$< z < 4.9$ Å), where the CN bond center density profile has a minimum. Molecules in the first sublayer have the cyanide group close to

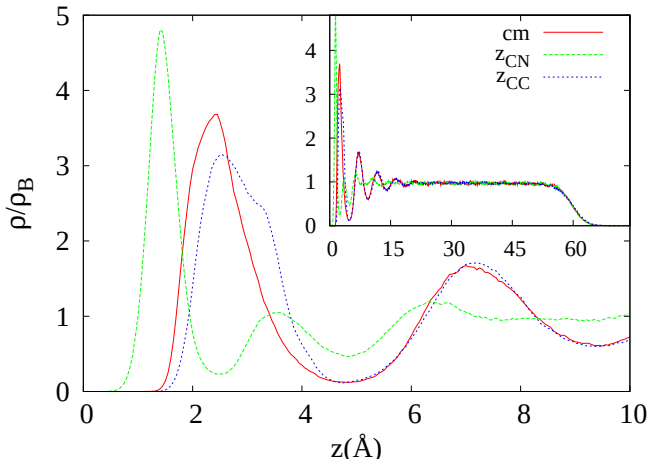

Figure 2.2: Molecular densities in the region $z < 10$ Å for different definitions of molecular positions: the center of mass (red line), the center of the CN bond (green line) and the center of the CT-C bond (blue line). The inset shows the molecular densities of the entire system ($0 < z < 80$ Å). The density is normalized to the bulk density ρ_B.

the surface, which is consistent with strong polar interactions. As shown below, molecules in the second sublayer have the cyanide group pointing away from the surface. This bilayer structure allows the methyl groups of both classes of molecules to cluster in the middle of the sublayers, as indicated by the peak of the the CT-C bond profile at about 3 Å. Indications of layering are seen more than 20 Å from the silica surface in the inset of Fig. 2.2, as was also the case for acetonitrile[1, 5].

This picture can be verified by the arrow plots in Fig. 2.3, which depict the bond locations and orientations for propionitrile in a typical configuration in the region $0 < z < 6$ Å. Here the CN vectors, with the arrowhead on the nitrogen atom (Fig. 2.3(a)), and CT-C vectors, with the arrowhead on the methyl carbon atom (Fig. 2.3(b)), are projected onto the xz plane. Note that vectors separated in the y direction can overlap in these plots, and so only information about the orientations and z positions of the individual bonds is meaningful.

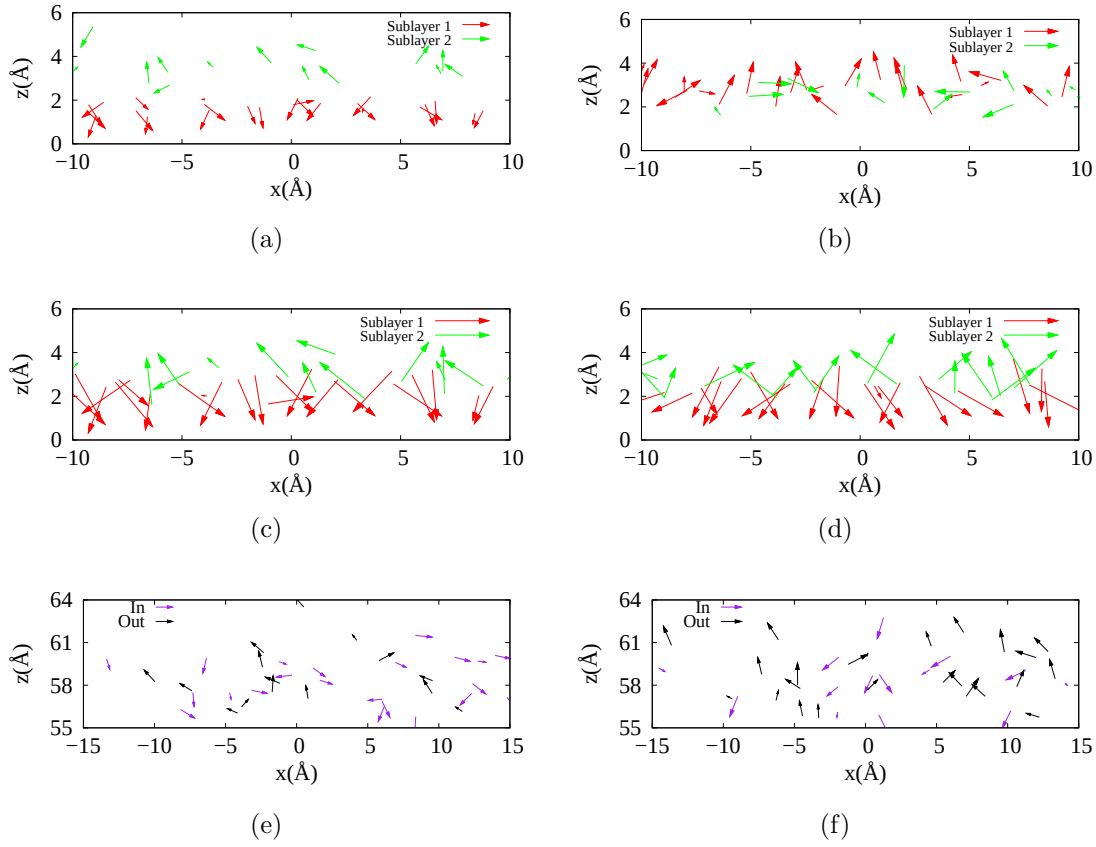

Figure 2.3: (a) Arrow plot of the CN vector arrangement in a typical configuration of propionitrile of in the first sublayer (red) and in the second sublayer (green). The head of each arrow represents the nitrogen atom. (b) Arrow plot of the CT-C vector configuration in the first sublayer (red) and the second sublayer (green). The head of each arrow represents the methyl carbon atom. (c) Arrow plot of the CT-N vector arrangement in the first sublayer (red) and in the second sublayer (green). The head of each arrow represents the nitrogen atom. (d) Arrow plot of CT-N vector arrangement in the first sublayer (red) and in the second sublayer (red) for the acetonitrile-silica system studied previously[5]. The head of each arrow represents the nitrogen atom and the tail of each arrow represents the methyl carbon atom. (e) Arrow plot of the CN vector arrangement at the liquid-vapor interface of propionitrile. Arrows with $\theta > 90°$ are marked as "In" (purple) and those with $\theta < 90°$ are marked as "Out" (black), where θ is the angle between CN vector and surface normal. (f) Arrow plot of the CT-C vector arrangement at the liquid-vapor interface of propionitrile. Arrows with $\theta > 90°$ are marked as "In" (purple) and those with $\theta < 90°$ are marked as "Out" (black), where θ is the angle between CT-C vector and the surface normal. All six plots are projected onto the xz plane, so some vectors are foreshortened and atoms indicated by arrowheads that are necessarily separated in the y direction by excluded volume interactions can appear to overlap. The legend of each plot gives the in-plane length of the bond vector. Each plot uses the same scale for the x- and z- axis.

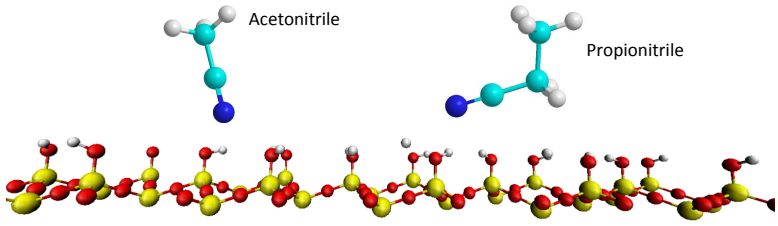

Figure 2.4: Schematic plot showing the typical orientation of acetonitrile and propionitrile at the silica surface: The CN bond in propionitrile tends to align more parallel to the surface than in acetonitrile. This figure serves as a visualization of arrow plots in Fig. 2.3.

Fig. 2.3(a) shows that at the liquid-solid interface the CN vectors form two sublayers. The density of CN groups in the outer sublayer is less than that in the surface sublayer. The CN vectors in the surface sublayer are also considerably more ordered than those in the outer sublayer. There is a clear region between the sublayers in which the density of CN groups is very low.

Fig. 2.3(b) shows that this region between the two CN sublayers is filled by alkyl groups, and that there is complete vertical mixing of the alkyl groups from the two sublayers. The alkyl groups from molecules in the surface sublayer tend to point away from the silica surface and to be farther from this surface than the alkyl groups from the outer sublayer. In contrast, the orientations of the alkyl groups for molecules in the outer sublayer tend to be more parallel to the silica surface. Fig. 2.3(b) demonstrates that, in contrast to the interdigitated alkyl region of the bilayer observed previously for acetonitrile[1, 5, 17, 18], the alkyl region of the surface bilayer in propionitrile is highly entangled.

The liquid-vapor (LV) interface is defined as the region over which the density of the CN bond centers decreases from 90% to 10% of the bulk density[5, 16], and

therefore extends from 56 Å to 63 Å. In the calculations of the orientational profiles below, we use a conservative definition for the bulk region as extending from 30 Å to 50 Å.

2.4 Molecular Orientations

To characterize the orientation of the fixed CN vector in the propionitrile molecule as a function of distance from the surface, we define a joint distribution function $h(z, \theta)$ [1]

$$h_{CN}(z, \theta) = \frac{1}{N_c} \sum_{i=1}^{N} \langle \delta(z - z_i) \delta(\theta - \theta_i) \rangle, \tag{2.1}$$

where $\delta(z)$ and $\delta(\theta)$ are Dirac delta functions, z is the position of the CN bond center in the molecule, θ is the angle between the vector and the surface normal and N_c is a normalization constant chosen such that $h_{CN}(z, \theta)$ is unity in the bulk fluid.

Here we analyze the orientation of propionitrile near the silica surface in terms of the CN vector orientation, the CT-C vector orientation, and other joint distribution functions.

2.4.1 CN Vector Orientations

We use the CN vector to study the orientation of the cyanide portion of the propionitrile molecule. These orientations can be directly compared to similar results for acetonitrile. Unlike acetonitrile, the dipole moment of propionitrile does not align strictly opposite to the CN vector, but the deviation is small. Thus studying

the orientation of CN vector in both cases provides information about the influence of dipole-dipole interactions on molecular orientations.

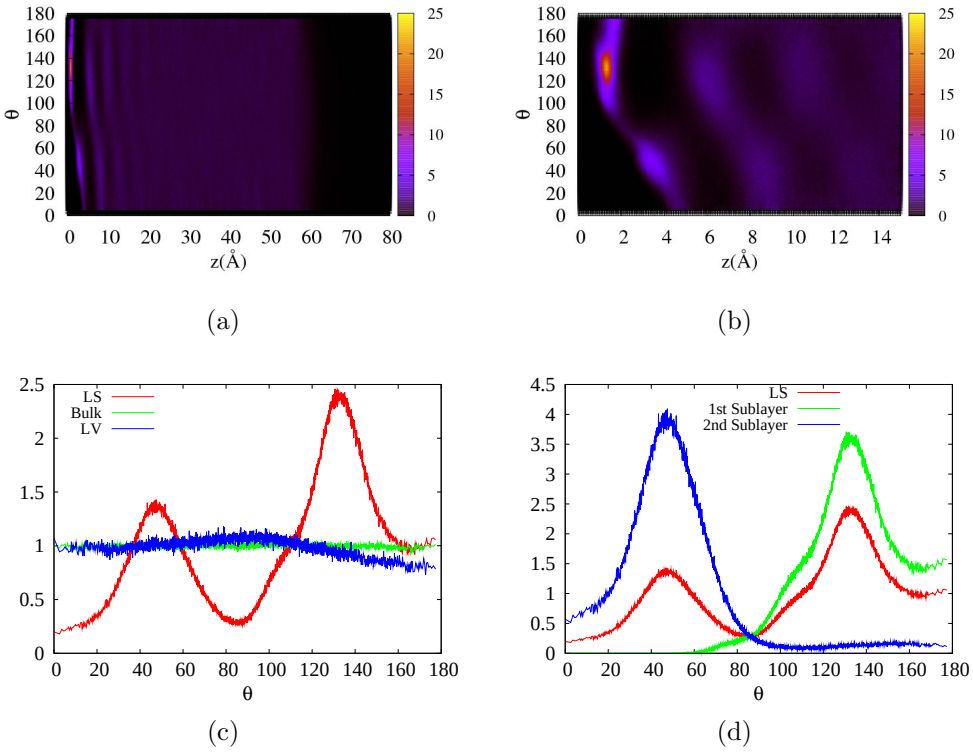

Figure 2.5: (a) Contour map of the joint distribution function $h_{CN}(z,\theta)$. (b) Zoom-in of the contour map in the region between $z = 0$ and $z = 15$ Å. (c) Angular distribution of the CN vector in the LS ($z < 4.9$ Å, red), bulk (30 Å$< z <$ 50 Å, green) and LV (56 Å$< z <$ 63 Å, blue) regions. (d) Angular distribution of the CN vector in the LS region (red) and its sublayers (first sublayer: $z < 2.5$ Å, green; second sublayer: 2.5 Å$< z <$ 4.9 Å, blue) .

Using the general definition in Eq. (2.1), we show in Fig. 2.5(a) a contour map of $h_{CN}(z,\theta)$, where θ is the angle between the CN vector and the surface normal. Similar to earlier results on acetonitrile[1], we see sigmoidal patterns in the contours of $h_{CN}(z,\theta)$ that propagate into the bulk for tens of angstroms, which is indicative of lipid-bilayer-like structures. The sigmoidal shape shows that the molecules closest to the silica surface tend to have their cyanide groups pointing towards the surface,

whereas for the next closest group of molecules the cyanide groups tend to point in the opposite direction, as seen in Fig. 2.3(a). This repeating pattern is washed out gradually on moving away from the silica surface. Propionitrile molecules form such bilayer-like structures in part to cancel the dipole field generated by the polar silica surface.

The angular distribution in the first LS layer shows two peaks, one centered around 45° and the other centered around 135°, indicating that there are two sublayers with opposite CN vector orientations. This conclusion is in general agreement with the arrow plot in Fig. 2.3(a). Such sublayer structure also indicates strong parallel correlations between CN vectors in the same sublayer, which is quite different from the antiparallel correlation seen in the bulk[48, 50].To show this parallel correlation function,we have calculated the radial/angular correlation function for CN vectors in a given region (liquid-solid, bulk or LV), which is defined as[5]

$$g(r,\theta) = \frac{1}{N_c}\sum_{i=1}^{N}\sum_{j=1}^{N}{}'\langle\delta(r-r_{ij})\delta(\theta-\theta_{ij})\rangle, \tag{2.2}$$

where N_c is the number of molecules contained in this region, r is the distance between center of mass of two molecules and θ is the angle between the CN vectors in between two propionitrile molecules. Contour plots of $g(r,\theta)$ in different regions are shown in Fig. 2.6. Compared with the typical antiparallel structure in the bulk and LV region, the $g(r,\theta)$ of first LS layer shows both parallel correlation at $\theta = 0°$, indicating angular correlation within the same sublayer, and antiparallel correlation at $\theta = 180°$, indicating correlation between molecules in one sublayer

with molecules in another sublayer. In the bulk there is only strong antiparallel correlation near $\theta = 180°$, because such an arrangement minimizes the interactions between molecular dipoles. The antiparallel correlation is stronger in the LV region than in the bulk, as was seen previously for acetonitrile[5].

It is interesting to contrast this bilayer structure with the structure that we have observed previously for acetonitrile at the silica interface[5]. In both cases, the CN vector on average has a approximately opposite orientation in the two sublayers. However, the angular distribution in the sublayer closest to the silica surface in propionitrile ($0 < z < 2.5$ Å) differs from that of acetonitrile [5]. Although the peaks in the angular distribution of the first sublayer for both acetonitrile and propionitrile are centered roughly around 135°, acetonitrile has a large distribution of CN orientations between 120° and 180°, while the CN orientations of propionitrile molecules tend to be distributed between 100° and 150°(Fig. 2.5(d)). This result shows that, compared with acetonitrile, propionitrile molecules tend to align their cyanide groups somewhat more parallel to the silica surface (Fig. 2.4), which is indicative of the influence of the packing and geometrical constraints imposed by its more complex hydrocarbon tail.

More insight is provided by comparing the CT-N vector arrow plot for propionitrile in Fig. 2.3(c) with that of acetonitrile in Fig. 2.3(d). Propionitrile clearly has a lower density in the second sublayer, but the vector orientations and the widths of the sublayers are similar. This result suggests that despite the longer and more complex hydrocarbon tail, propionitrile molecules tend to maintain the same location and thickness of the bilayers as acetonitrile. This structure requires that the

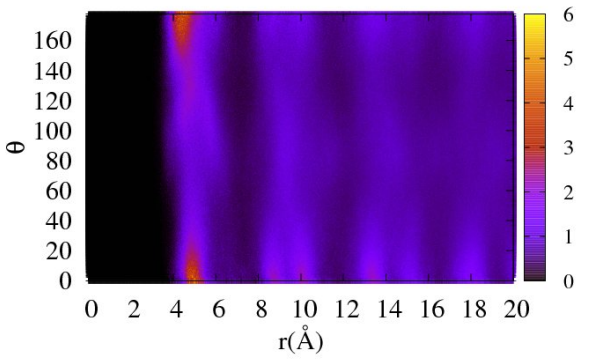

(a) LS

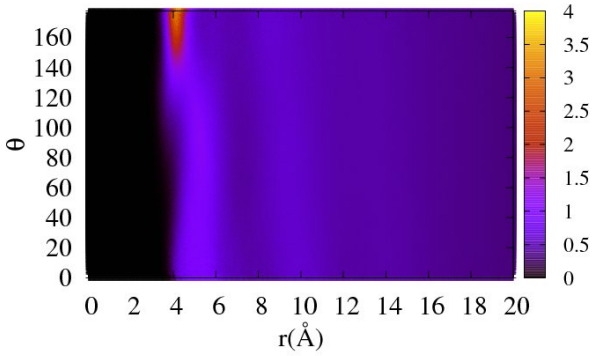

(b) Bulk

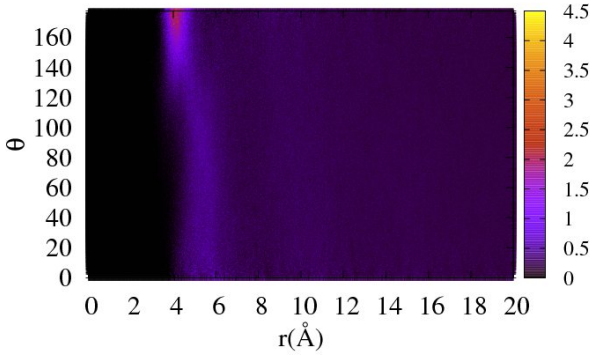

(c) LV

Figure 2.6: Contour plot of the radial/angular distribution function $g(r, \theta)$ in the LS, bulk and LV regions. r is the distance between the centers of mass of a pair of molecules and θ is the angle between their CN vectors.

CN bond of a typical propionitrile molecule to be more a tilted toward the surface in the first sublayer and that the entangled structure of the hydrocarbon groups in the intermediate hydrocarbon sublayer for propionitrile to be more closely packed than the interdigitated structure in acetonitrile. These structural features of the propionitrile bilayer are discussed in more detail below.

2.4.2 CT-C Vector Orientations

The orientational analysis of the CT-C vector, which points from the methylene carbon to the methyl carbon, is similar to that for the CN vector. The joint distribution function $h_{CC}(z, \theta)$ is akin to the one defined in Eq. (2.1), but in this case z is the center of the CN bond and θ is the angle between the CT-C vector and the surface normal. This distribution function is plotted in Fig. 2.7.

As is shown in Fig. 2.7(b) and Fig. 2.7(d), at the silica-propionitrile interface, the CT-C orientations in the first sublayer ($0 < z < 2.5$ Å) show a broad distribution from 0° to 120°, with high probability around 0°. This result indicates that propionitrile tends to keep its nonpolar methyl group away from the polar surface, with the CT-C vector almost parallel to the surface normal. The second sublayer (2.5 Å$< z < 4.9$ Å) has a significantly lower density of molecules and a broad distribution of CT-C orientations. This distribution ranges from about 40° to 180° and peaks around 70°, indicating that CT-C vectors have a tendency to lie parallel to the silica surface. This finding is in agreement with the arrow plot in Fig. 2.3(b).

As is shown in Fig. 2.7(c), at the LV interface the area of the CT-C orienta-

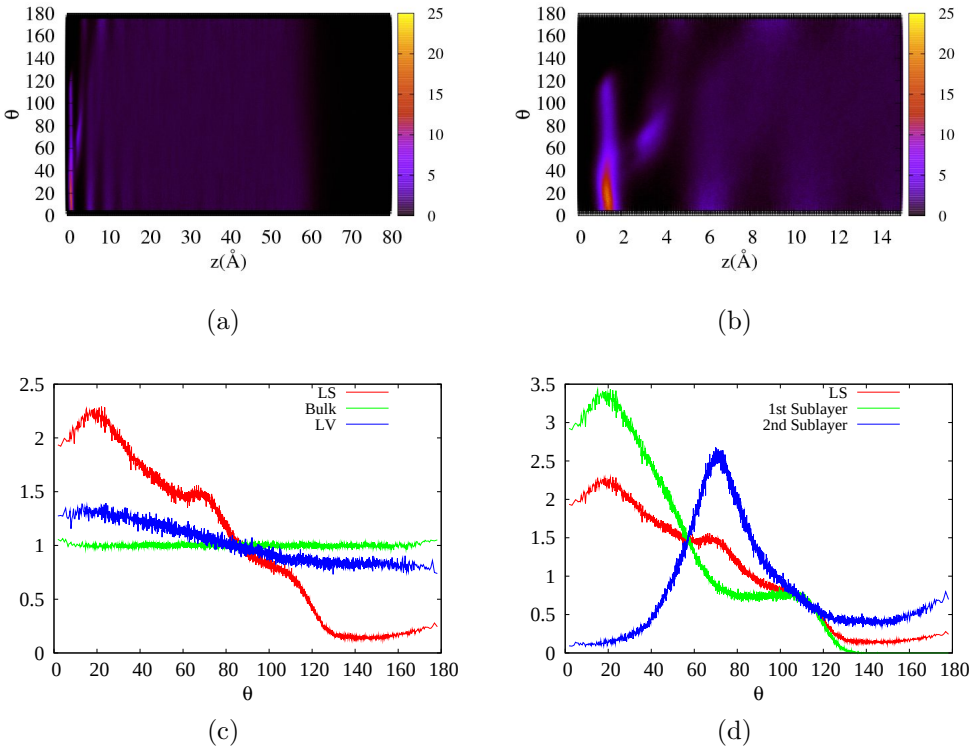

Figure 2.7: (a) Contour plot of the joint distribution function $h_{CC}(z, \theta)$, where z is the center of CN bond and θ is the angle between the CT-C vector and the surface normal. (b) Zoom-in of the contour plot that shows the region between $z = 0$ and $z = 15$ Å.(c) Angular distribution of the CT-C vector in the LS ($z < 4.9$ Å, red), bulk (30 Å$< z < 50$ Å, green) and LV (56 Å$< z < 63$ Å, blue) regions. (d) Angular distribution of the CT-C vector in the LS region (red) and its sublayers (first sublayer: $z < 2.5$ Å, green; second sublayer: 2.5 Å$< z < 4.9$ Å, blue) .

tional distribution below 90° is larger than that above 90°, indicating that molecules tend to point their methyl groups into the vapor phase. This finding can be also verified by the arrow plot of CT-C vector in Fig. 2.3(f). The simulated CT-C vector orientations in both the first LS layer and the LV region are supported by the VSFG experiments[22].

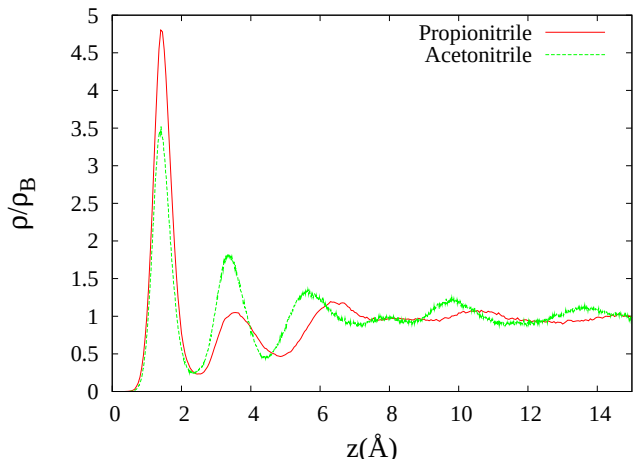

Figure 2.8: Comparison of the CN density in acetonitrile and propionitrile, where z is the center of the CN bond. The density is normalized by the bulk density ρ_B.

2.4.3 Packing of the Hydrocarbon Groups

Repulsive core forces prevent the overlap of alkyl groups of acetonitrile and propionitrile in the hydrocarbon-rich region between the two polar sublayers. Fig. 2.8 compares the sublayer structure for the acetonitrile and propionitrile systems as measured by the center of the CN bond. We find that the first sublayer in propionitrile has a much higher density than the second sublayer. Indeed, the peak height for the first sublayer is notably greater in propionitrile than in acetonitrile, although the latter liquid has a higher density in the second sublayer. These differences cannot be primarily associated with more favorable polar bonding to the surface, because propionitrile and acetonitrile have similar dipole moments (in our simulation model propionitrile's dipole moment is 4.20 Debye and acetonitrile's dipole moment is 3.95 Debye[50]). Presumably these differences in packing arise from effects associated with incorporating the asymmetrically bonded hydrocarbon groups in propionitrile in the intermediate hydrocarbon layer.

First we have calculated the 2-D radial distribution function of the CT-C bond center in the LS region, shown in Fig. 2.9. The $g(r)$ in the LS region and its sublayer show long-ranged order that propagates for more than 20 Å. This indicates that hydrocarbon groups of propionitrile in the LS region have formed well ordered 2-D structure, presumably in accordance with the periodic structure of the silica surface.

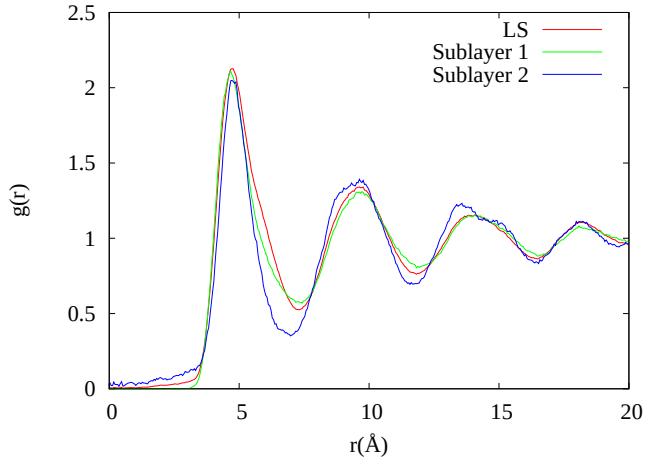

Figure 2.9: 2-D radial distribution function $g(r)$, where r is distance between CT-C bond center on the xy plane.

To provide more information about the interplay among the hydrocarbon energetics and packing and the surface-induced ordering of the polar groups in the sublayers, we have projected the positions of the CT atoms in the LS region onto the surface xy plane. The probability distribution for these CT projections from propionitrile molecules in the two sublayers is presented in Fig. 2.10(a) as a contour plot. The colored regions denote areas in which the probability distribution value is above 20% of its local maximum, i.e. positions where the CT atoms are most likely to appear. In Fig. 2.10(b), projections of CT atoms from the first sublayer (green)

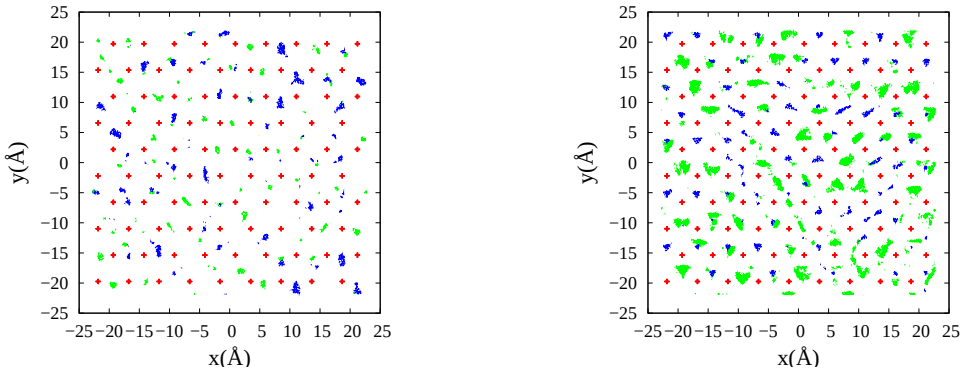

(a) (b)

Figure 2.10: Probability distribution of the CT atom's projection onto the silica surface for (a) propionitrile and (b) acetonitrile. The probability distribution is represented by contour lines that are green for molecules in the first sublayer and blue for molecules in the second sublayer. The red crosses represents the sites of surface oxygen atoms.

occupy most available sites, leaving relatively few transient vacancies. These vacancies tend to be filled by CT atoms from molecules in the second sublayer (blue), thus resulting in a surprisingly well ordered and closely packed 2D structure.

A similar closely packed structure also exists at the acetonitrile-silica interface, as is shown in Fig. 2.10(b) (here "CT" is the methyl carbon atom of acetonitrile). However, comparing Fig. 2.10(a) with Fig. 2.10(b), we see that propionitrile has a higher density with smaller fluctuations of polar groups in the first sublayer, as is also supported by the comparison of the CN center densities for these two liquids in Fig. 2.8. Moreover fluctuations of the CT atoms in the dense and entangled hydrocarbon layer of propionitrile are significantly smaller than those for acetonitrile.

Such closely packed structure can also be verified by reorientation dynamics. Here we have calculated the orientational time-correlation function (TCF) for the CN vector for both acetonitrile and propionitrile in the LS region. The orientational

TCF is defined as the dot product of unit CN vector at time 0 with the same vector at time t.

$$C(t) = \frac{1}{N_c} \sum_{i}^{N_c} \langle \mathbf{v}_i^{CN}(0) \cdot \mathbf{v}_i^{CN}(t) \rangle, \tag{2.3}$$

where N_c is the number of molecules in the given region. As shown in Fig. 2.11, since the hydrocarbon groups in propionitrile LS region are more compactly packed, this induces a slower reorientation dynamics of the CN group.

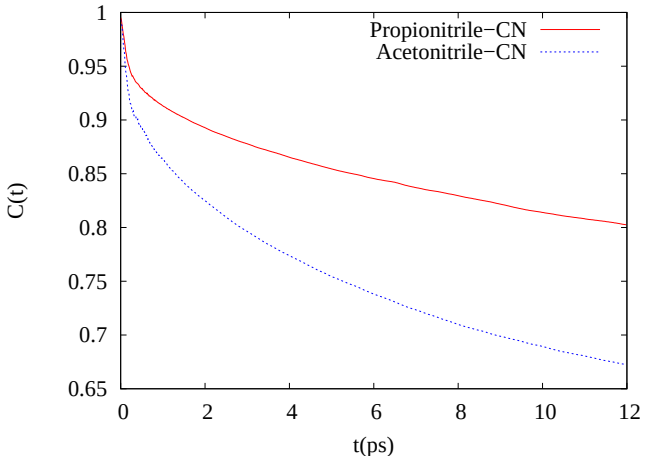

Figure 2.11: Comparison of the CN bond orientational TCF in the LS region for both acetonitrile (blue) and propionitrile (red).

2.5 Electrostatics

Electrostatics plays a key role in the surface induced ordering seen in Fig. 2.10. The microscopic charge density $\rho^q(z)$ from mobile propionitrile molecules is plotted in Fig. 2.12(a). The deep negative well and high peak suggest the existence of dipolar ordering that partially cancels the fixed dipole field of the hydrophilic surface, which is consistent with the acceptance of surface hydrogen bonds. This layered structure propagates into the bulk for tens of Ångstroms. As is shown in

the inset of Fig. 2.12(a), the profile of $\rho^q(z)$ in the LV region is too noisy to discern any structure.

As was the case for acetonitrile [1, 5], the Gaussian-smoothed charge density[29, 30, 51] can be used to develop a deeper understand of the underlying long-range features of the electrostatics. The Gaussian-smoothed charge density ($\rho^{q\sigma}$) associated with a given microscopic charge density $\rho^q(\mathbf{r}')$ is defined as

$$\rho^{q\sigma}(\mathbf{r}) \equiv \int d\mathbf{r}' \rho^q(\mathbf{r}') \rho_G(|\mathbf{r} - \mathbf{r}'|), \tag{2.4}$$

where $\rho_G(\mathbf{r})$ is a unit Gaussian charge distribution with width σ, defined as

$$\rho_G(\mathbf{r}) = \frac{1}{\pi^{\frac{3}{2}}\sigma^3} \exp(-\frac{r^2}{\sigma^2}), \tag{2.5}$$

where σ is a smoothing length of the order of a typical nearest neighbor-spacing, which here we take to be 4.0 Å.

Fig. 2.12(b) shows the smoothed charge density of propionitrile only (red solid line) and the total smoothed charge density (green dashed line), which includes the fixed charges on the silica surface. Upon smoothing, the random noise in the original charge density cancels out. The smoothed charge density is two orders of magnitude smaller than the original microscopic charge density but clearly reveals long ranged electrostatic features. The smoothed charge density indeed indicates that there is weak dipolar ordering in the LV region (47 Å- 75 Å), with more CN vectors pointing into the liquid phase. At the silica/liquid interface there are strong oscillations in

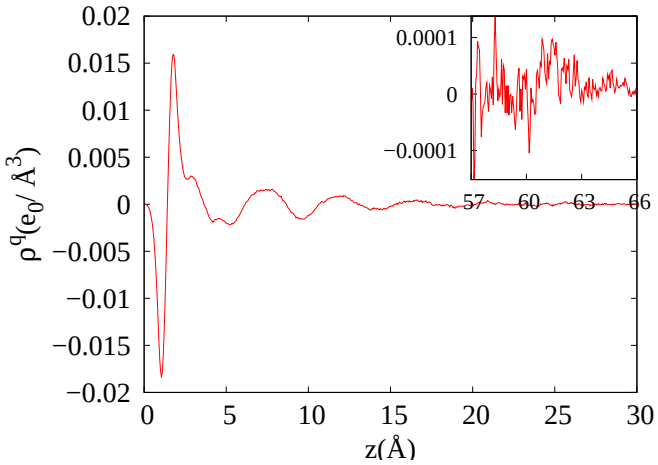

(a)

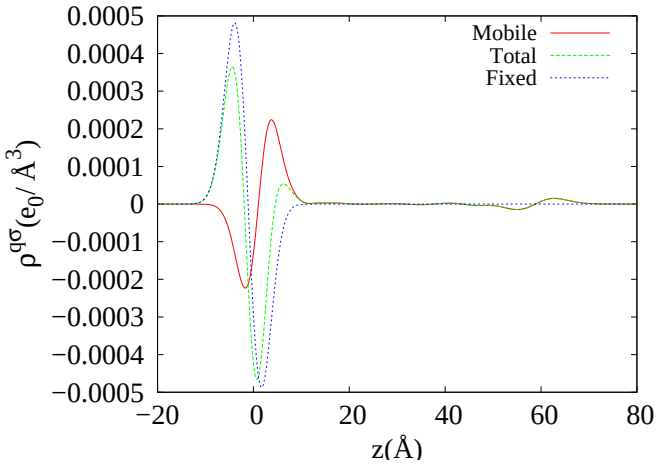

(b)

Figure 2.12: (a) The charge density of the mobile species (propionitrile) $\rho^q(z)$ in the region $0 < z < 30$ Å. The inset shows $\rho^q(z)$ in the liquid/vapor region (56 Å$< z <$ 63 Å). (b) The Gaussian smoothed charge density ($\sigma = 4.0$ Å) of the propionitrile charge density (red), the total charge density (green) and the fixed charge density of the silica surface (blue).

the smoothed charge density profile of propionitrile, induced by (and out of phase with) the smoothed charge density of the fixed charges on the silica surface.

2.6 Summary and Conclusions

The structure and organization of propionitrile at a planar hydrophilic silica surface and at its LV interface have been studied by MD simulations. Similar to the case of acetonitrile, a lipid-bilayer-like structure exists at the propionitrile-silica interface. However, the CN vector of the cyanide group tends to be more parallel to the surface in propionitrile than in acetonitrile. Analysis of methylene-methyl vector orientations shows that in the first sublayer layer of the LS region, most propionitrile molecules point their methyl groups roughly along the surface normal. In contrast, the methyl groups in the outer sublayer are closer to the surface than the methyl groups in the surface sublayer and tend to lie perpendicular to the surface normal. These effects lead to a surface bilayer with highly entangled alkyl groups. As a result, when compared to the overall molecular dimensions, the propionitrile bilayer is more compact and ordered than the corresponding acetonitrile bilayer. These results are consistent with the VSFG and OKE data.

At the LV interface, propionitrile molecules have a slight tendency to point their methyl groups into the vapor phase. This result is also in agreement with the experimental data.

The results of this study suggest that lipid-bilayer-like structures at silica surfaces may be a common feature of alkyl cyanide liquids. However, it is also

clear that the structure of the alkyl tail plays an important role in determining the nature of the bilayer. Simulations of the interfacial behavior of related molecules will provide further insights into the interplay between electrostatic and dispersion interactions and the packing of nonpolar groups in lipid-bilayer-like structures.

Chapter 3

Methanol Near Hydrophilic Silica Wall

This chapter partially depends on the paper "Nonpolar adsorption at the silica/methanol interface: surface mediated polarity and solvent density across a strongly associating solid/liquid boundary"by Roy, Liu, Siler, Woods, Fourkas, Weeks and Walker[52], submitted to the Journal of Physical Chemistry.

3.1 Introduction

The simulation and analysis of the methanol-silica system are similar to that for propionitrile-silica system. However, the hydroxyl groups in methanol molecules enable methanol molecules to form mutual hydrogen bonds (H-bonds). Moreover, near the silica surface this makes methanol not only a H-bond acceptor, like nitriles, but also a H-bond donor. Therefore the structure of the methanol-silica interface is expected to be very different from the nitrile-silica interface.

Recently, molecular dynamics (MD) and Monte Carlo (MC) simulations have been performed for systems with methanol in silica nanopores[53–55]. In these simulations, methanol molecules are strongly bonded to the silica surface via hydrogen bonds with silanol groups, thus inducing slower reorientation and translation dynamics at the methanol/silica interface. However, for methanol confined in silica nanopores, the liquid structure depends on both general properties of the silica sur-

face and on details of the confined geometry, and the relative importance of these contributions cannot be decoupled in a straightforward way. In the simulations reported here, we examined the simpler case of a slab of liquid methanol at liquid-vapor coexistence near an idealized flat silica surface. Our simulation serves as a reference for second harmonic generation (SHG) and time resolved fluorescence emission study of the methanol/silica interface[52].

3.2 Simulation Details

The system consists of the same silica surface used in acetonitrile and propionitrile simulations and 1000 methanol molecules. We use the OPLS all-atom (OPLS-AA) model[56] to describe the intra and intermolecular interactions between methanol molecules. In the OPLS-AA model of methanol, "CT"represents the carbon atom, "HC"represents hydrogen atom in the methyl group, "O"represents the oxygen atom and "H"represents the hydrogen atom in the OH group. OPLS-AA nonbonding parameters for methanol are given in Table 3.2. For Lennard-Jones interactions between methanol molecules, we use the combining rules for OPLS model: $\sigma_{ij} = \sqrt{\sigma_i \sigma_j}$ and $\epsilon_{ij} = \sqrt{\epsilon_i \epsilon_j}$. For the Lennard-Jones interactions between methanol and atoms on the silica wall, Lorentz-Berthelot mixing rules were utilized: $\sigma_{ij} = (\sigma_i + \sigma_j)/2$ and $\epsilon_{ij} = \sqrt{\epsilon_i \epsilon_j}$. We employed periodic boundary conditions with $L_x = 45.60$ Å, $L_y = 43.88$ Å and $L_z = 150$ Å. Treatment of electrostatic and Van der Waals interactions is exactly in the same way as we did in the propionitrile system. MD simulations in the NVT ensemble were performed using the DL_POLY

2.18[49] package with timestep 1 fs. After the system has been equilibrated for 300 ps at T = 298 K, configurations of the system were recorded every 15 fs. The total sampling lasted for 450000 steps and gave a trajectory file with a total of 30000 configurations for analysis.

Atom	q	ϵ_{LJ},kcal/mol	σ_{LJ},Å
CT	0.145	0.066	3.500
HC	0.040	0.030	2.500
O	-0.683	0.170	3.120
H	0.418	0.000	0.000

Table 3.1: OPLS-AA parameters for intermolecular interactions between methanol molecules.

3.3 Density Profiles

Similar to the treatment for propionitrile, to study the layering structure near the methanol/silica interface more effectively, density profiles with different molecular definitions, including the center of mass, the center of the O-H bond and the carbon atom density are plotted in Fig. 3.1. This simulation data show that near the silica surface, all densities drop to their minimum at about 3.1 Å, indicating the existence of a tightly-bound layer at the methanol-silica interface, which is defined as the first layer of liquid/solid (LS) interface. The O-H density (green line) inside this layer exhibit two peaks: one very high peak near the silica surface, indicating strong hydrogen bonding between methanol and surface hydroxyl groups, and a very small second peak, which presumably maintains the hydrogen bonding between methanol molecules in the surface layer and those in the bulk. Therefore, the O-H density

profile indeed suggests that at the methanol-silica liquid-solid interface, there exist sublayer structures. We may separate these two peaks at 1.5 Å, so as to study the sublayer structure. Similar to the case of propionitrile, we may define the bulk region where the O-H density is between 20 Å and 30 Å, and the liquid-vapor (LV) interface region that extends from 32 Å to 40 Å.

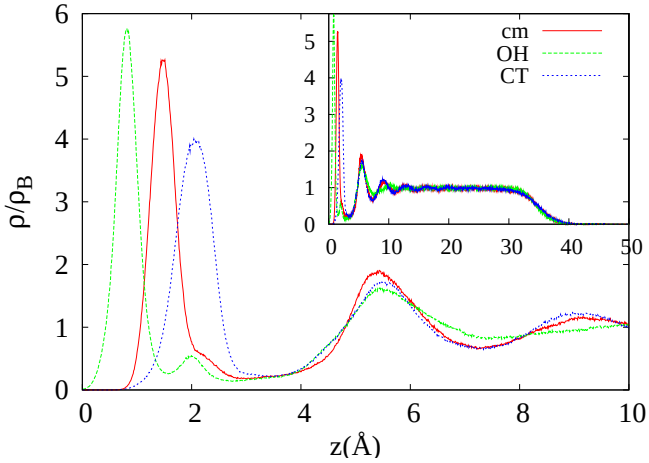

Figure 3.1: Methanol density defined by the center of mass (cm, red line) and the center of the O-H bond (green line). The carbon atom density (blue line) is also given. The inset figure gives density profiles of the whole system (0-50 Å), where we can also see the transition from the liquid to vapor phase about 35 Å from the substrate. The density is normalized by the bulk density ρ_B.

Comparing the interfacial center of mass densities of methanol and acetonitrile is instructive(Fig. 3.2). At the silica surface, the methanol center of mass density is significantly higher than that of acetonitrile, indicating that more methanol molecules are tightly absorbed to the silica surface due to the strong hydrogen bonding. One notable feature of methanol density profile at LS interface is that the density in the first sublayer is extremely high while the density in the second sublayer is almost negligible. To interpret this, we have calculated the average number of molecules in the LS region and its sublayers for acetonitrile and methanol, re-

spectively, as shown in Table 3.2. In spite of huge difference in number of molecules in sublayers, the average number of molecules in both acetonitrile and methanol LS region are to be very close to each other. This can be related to the packing of hydrocarbon groups discussed in Section 2.4.3. In the LS region for both acetonitrile and methanol, methyl groups form highly ordered interdigitated structure in accordance with the 2-D periodicity of the silica surface. However, due to the periodicity of the silica surface and hard core repulsion between methyl groups, at the 2-D level only a finite number of sites can be occupied by methyl groups. Therefore, when strong hydrogen bonds make more methanol absorbed to the surface and form the first sublayer, very few sites are available for the methyl groups in the second sublayer to form interdigitating structures with methyl groups from the first sublayer, and this explains the extreme low density in the second sublayer.

	Sublayer 1	Sublayer 2	LS
Acetonitrile	52.46	45.55	98.01
Methanol	86.58	13.16	99.74

Table 3.2: Average number of molecules in the LS region and its sublayers for acetonitrile and methanol.

3.4 Molecular Orientation

Similar to the case of propionitrile, the orientation of methanol molecules in different regions can be illustrated by calculating the orientational distribution of O-C and O-H bonds.

In Fig. 3.3(a), we have plotted the O-C vector orientation in the LS, bulk

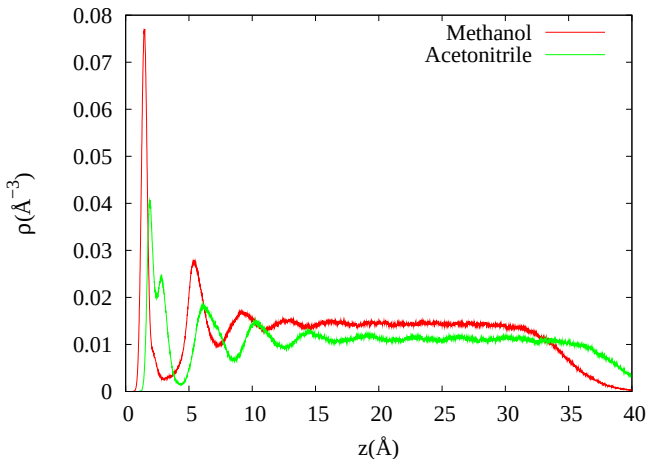

Figure 3.2: Center of mass density of liquid methanol at the silica surface (red) and liquid acetonitrile at the silica surface (green) from our previous work[1, 5].

and LV regions. At the liquid/vapor interface, the area of the O-C orientational distribution below 90° is larger than that above 90°, showing that there are more methanol molecules pointing their nonpolar methyl groups into the vapor phase, such that they could still maintain the hydrogen bonding with molecules in the liquid phase. In the LS region, the orientational distribution can be further calculated in its sublayers (Fig. 3.3(b)). In the sublayer closest to the silica surface ($z < 1.5$ Å), the O-C vector orientation distribution has a very high intensity near 0°, indicating most O-C vectors point perpendicularly away from the surface. In the second sublayer (1.5 Å$< z <$ 3.1 Å), the O-C bond has a broad distribution centered at about $\theta = 104.5°$.

We can calculate the orientational distribution for O-H bond as well, shown in Fig. 3.4. At the LV interface, more methanol molecules would point their O-H bonds into the bulk to maintain hydrogen bonding (Fig. 3.4(a)). At the LS interface, in the first sublayer the O-H orientation distribution centers at about $\theta = 107.5°$, so as

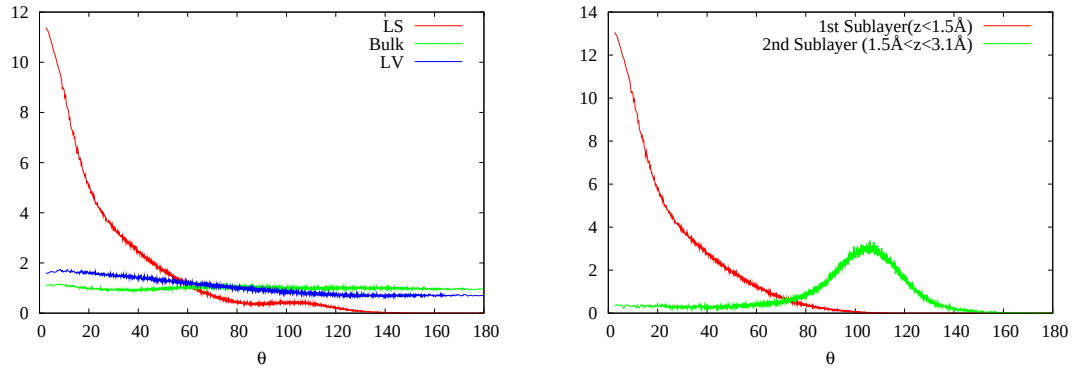

(a) (b)

Figure 3.3: (a) Orientation distribution of the O-C vector in LS, bulk and LV region, where θ is the angle between surface normal and O-C vector. (b) Orientation distribution of the O-C vector in two sublayers at the methanol/silica interface. In both figures the boundaries of regions are defined by the position of O-H bond center and the angular distribution density has been scaled by a constant such that it is unity for the bulk.

to form hydrogen bonds with surface hydroxyl groups. In the second sublayer, the orientation distribution of the O-H bond centers at about $\theta = 148.2°$, suggesting that O-H bonds in this sublayer tend to point towards methanol molecules in the first sublayer so as to form additional hydrogen bonds rather than exploit Van der Waals attractions between methyl groups in adjacent sublayers. One can visualize this orientation feature by means of a vector plot of bond orientations in a typical configuration, shown in Fig. 3.5. From Fig. 3.5 one observes that the strong hydrogen bonding of the methanol O-H to the silica surface results in the methyl group pointing upward and forming an effective hydrocarbon surface, as is shown by the green arrow layer in Fig 3.5. Such an effective hydrocarbon surface has also been verified in time resolved fluorescence spectroscopy experiment[52], in which the Coumarin 151 molecule feels a nonpolar environment at the methanol/silica interface that is totally different from methanol bulk. Molecules in the lower-density, second

sublayer can be recognized only by those few red arrows embedded in the green arrow layers where the second sublayer inserts methyl groups into the hydrocarbon layer to enhance Van der Waals interactions and points hydroxyl groups toward the surface to donate hydrogen bonds to molecules in the first sublayer.

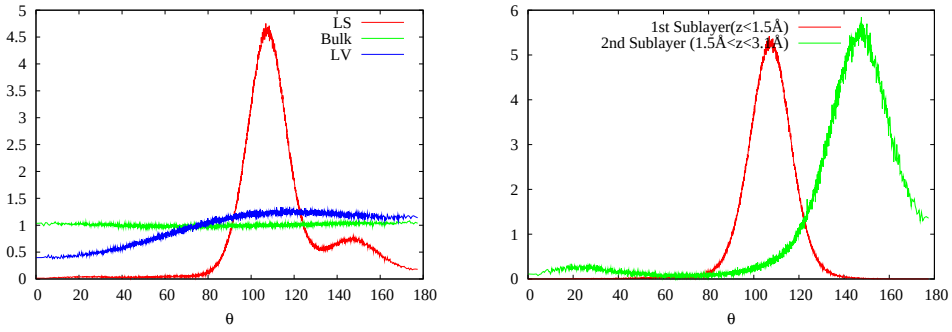

(a) (b)

Figure 3.4: (a) Orientation distribution of the O-H vector in LS, bulk and LV region, where θ is the angle between surface normal and O-H vector. (b) Orientation distribution of the O-H vector in two sublayers at the methanol/silica interface. In both figures the boundaries of regions are defined by the position of O-H bond center and the angular distribution density has been scaled by a constant such that it is unity for the bulk.

3.5 Hydrogen Bonds and Dynamics

Since our study of density and orientation at LS interface suggests strong hydrogen bonding between methanol molecules and surface hydroxyl groups, it will be interesting to analyze hydrogen bonds in the LS region quantitatively. Unlike water, which can form four H-bonds with neighboring molecules and maintain a tetrahedral H-bond network in the bulk[57], in the bulk phase methanol molecules can participate in two H-bonds with nearby molecules at most, thus forming H-bond chains[58], as shown in Fig. 3.6. The number of molecules in such H-bond

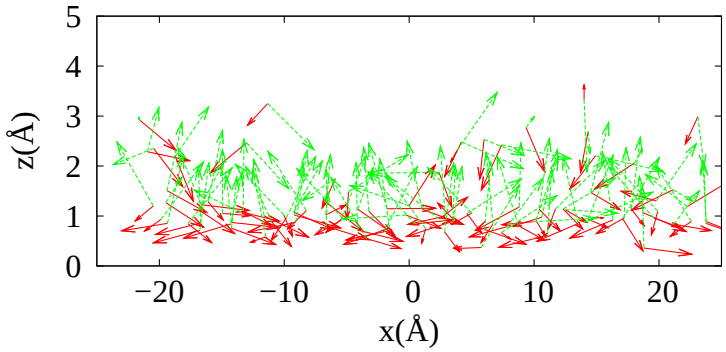

Figure 3.5: Arrow plot of O-C (green) and O-H (red) vectors in the methanol/silica interface region. The ends of both green and red arrows represent the oxygen atom, and heads of green and red arrows represent carbon and hydrogen atom, respectively. Vectors are projected onto the xz plane, so in the y direction they can appear to overlap.

chains may vary from 5 to 20 molecules, depending on the specific model used in the simulation[59]. Also, in bulk methanol, not all the molecules can participate in two H-bonds[58], so the average number of H-bond per molecule is roughly between 1.7 and 1.9, depending on specific model and definition of H-bond.

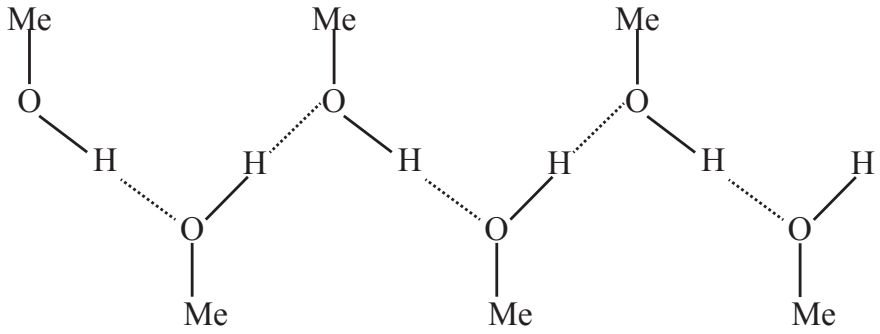

Figure 3.6: A schematic illustration of H-bond chains in bulk methanol based on Ref. [58], each methanol molecule can participate in two H-bonds and the methyl group is represented with the symbol "Me".

At the hydrophilic silica surface, methanol can also form H-bonds with sur-

face hydroxyl groups by either accepting or donating H-bonds. Compared with acetonitrile, which can only accept H-bonds from the surface, the hydrogen bonding between the methanol molecules and silica surface is much stronger. Moreover, since the surface hydroxyl density is very high ($4.54/\text{nm}^2$), it is likely that each methanol molecule may form more than two H-bonds with surface hydroxyl groups. Here we have calculated the average number of hydrogen bonds per molecule at a given distance away from the surface. For the definition of a H-bond, we used the geometric criterion of previous work[55]: r(O...O) is smaller than 3.4 Å and $\angle HO...O$ is smaller than 30°. The number of H-bonds per molecule as a function of distance away from the surface is plotted in Fig. 3.7. The peak near the surface indicates that methanol molecules in the first sublayer participate in slightly more than two H-bonds per molecule on average and this is visualized in Fig. 3.8(a). In Fig. 3.8(a), we have shown all hydroxyl groups in the LS region, from both methanol and surface silanols, and H-bonds between them (red dashed lines). It is obvious that hydroxyl groups together with silanol groups form H-bond chains that are much longer than those formed in the bulk (Fig. 3.8(b)). In other words, silanol groups serve as joints that connect H-bond chains such that most methanol molecules can form two H-bonds. Combined with the fact that a small portion of molecules can form more than two H-bonds, we find that the average number of H-bonds per molecule in the first sublayer is greater than two. Our analysis also shows that for the hydrogen bonding between the first sublayer and silanol groups on the surface, methanol molecules have equal chances to serve as a H-bond donor or acceptor. However in the second sublayer, the curve in Fig. 3.7 drops to a min-

imum less than 1, indicating that methanol molecules in the second sublayer are unable to form multiple H-bonds with molecules in the first sublayer or in the bulk. Thus the silica surface combined with tightly bound methanol molecules in the first sublayer is indeed nonpolar and the interfacial solvent is restricted from interacting strongly with the rest of the system. In the bulk, since the length of H-bond chains is shorter (Fig. 3.8(b)) and fewer molecules are participating in two H-bonds, the average number of H-bonds per molecule is about 1.72, given by the plateau in Fig. 3.7.

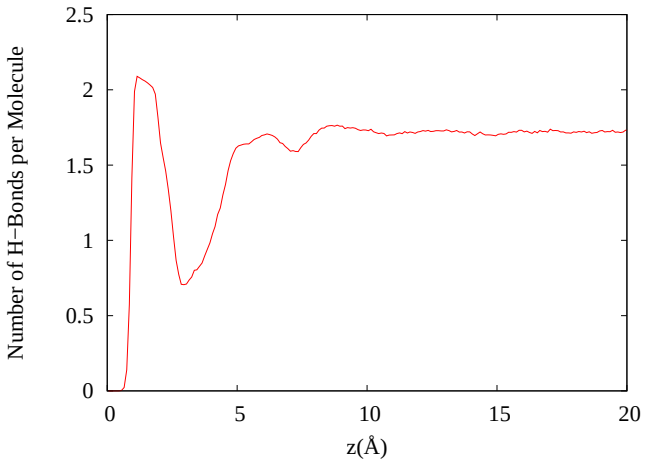

Figure 3.7: Number of hydrogen bond per molecule as a function as distance away from the silica surface.

Orientational time-correlation functions (TCFs) provide another powerful measure of the strong hydrogen bonding between methanol and the silica surface. We consider here the orientational time-correlation functions that has already been defined in Eq. (2.3), for both O-C and O-H vectors. In Fig. 3.9(a) and 3.9(b), we have plotted the orientational TCFs for methanol O-H and O-C vectors in LS, bulk and LV regions. Apparently at the LS interface, reorientation dynamics is much

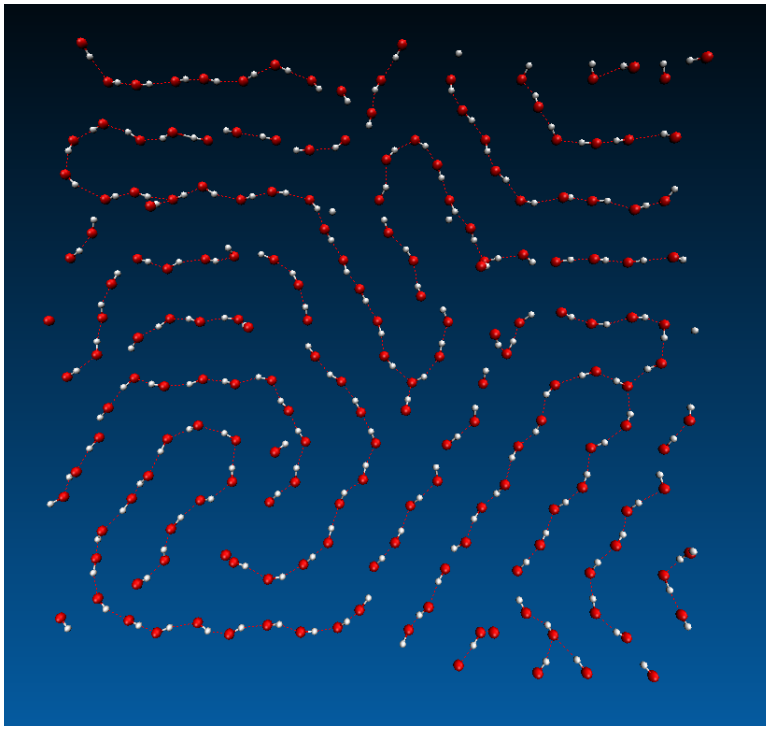

(a)

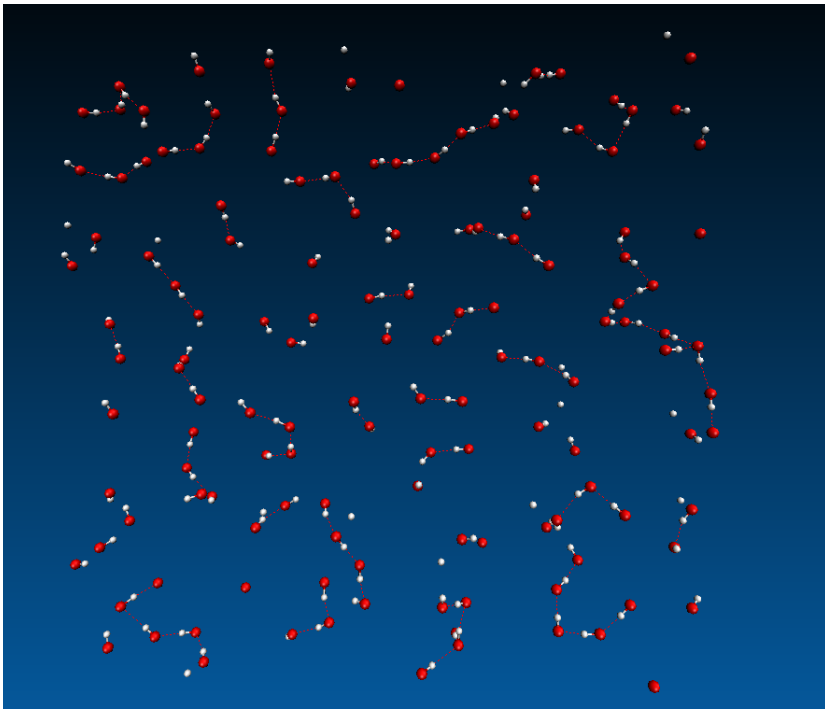

(b)

Figure 3.8: (a) Hydroxyl groups (white:hydrogen; red:oxygen) in the LS region, including hydroxyl groups from both the silica surface and methanol molecules. The hydrogen bond is represented by red dash lines. (b)Hydroxyl groups (white:hydrogen; red:oxygen) in the bulk region (20 Å$< z <$ 25 Å). The hydrogen bond is represented by red dash lines.

slower due to strong hydrogen bonding between methanol and silica surface, while at the LV interface, molecules have more freedom to reorientate themselves in a more dilute environment, resulting in faster reorientation dynamics.

It would also be very interesting to compare the orientational TCFs of methanol with that of acetonitrile. In Fig. 3.9(c) we have plotted the orientational TCFs of methanol O-H bond and acetonitrile C-N bond in the LS region, both of which are the polar part of the molecule that is in direct interaction with the silica surface. At the silica surface the O-H orientational TCFs decays much more slowly than the C-N orientational TCF of acetonitrile, indicating that the interaction between methanol hydroxyl groups and surface silanol groups is much stronger and more directional than that of acetonitrile. Moreover, the methanol O-H reorientation dynamics is even slower than that of the propionitrile C-N bond, which has been convinced to be slower than acetonitrile in Section 2.4.3 due to close packing of hydrocarbon groups. This indeed shows that mutual hydrogen bonding with the surface would create more binding to the surface molecules than the hydrophobic interactions between nonpolar groups. We have also compared the methanol O-C orientational TCF with the acetonitrile C-C (the bond that connecting two carbon atoms) orientational TCF at the LS interface, shown in Fig. 3.9(d). Both bonds can be viewed as the bridge connecting the polar and the nonpolar part of the molecule. The O-C vector orientational dynamics of methanol at the LS interface are not distinctly slower than that of the acetonitrile C-N vector reorientation. In the case of acetonitrile, the majority of surface orientational dynamics occurs without breaking of hydrogen bonds with silanol groups[14]. The calculated TCFs shown in Fig. 3.9

predict that the same argument should hold true for methanol hydrogen bonded to the silica surface.

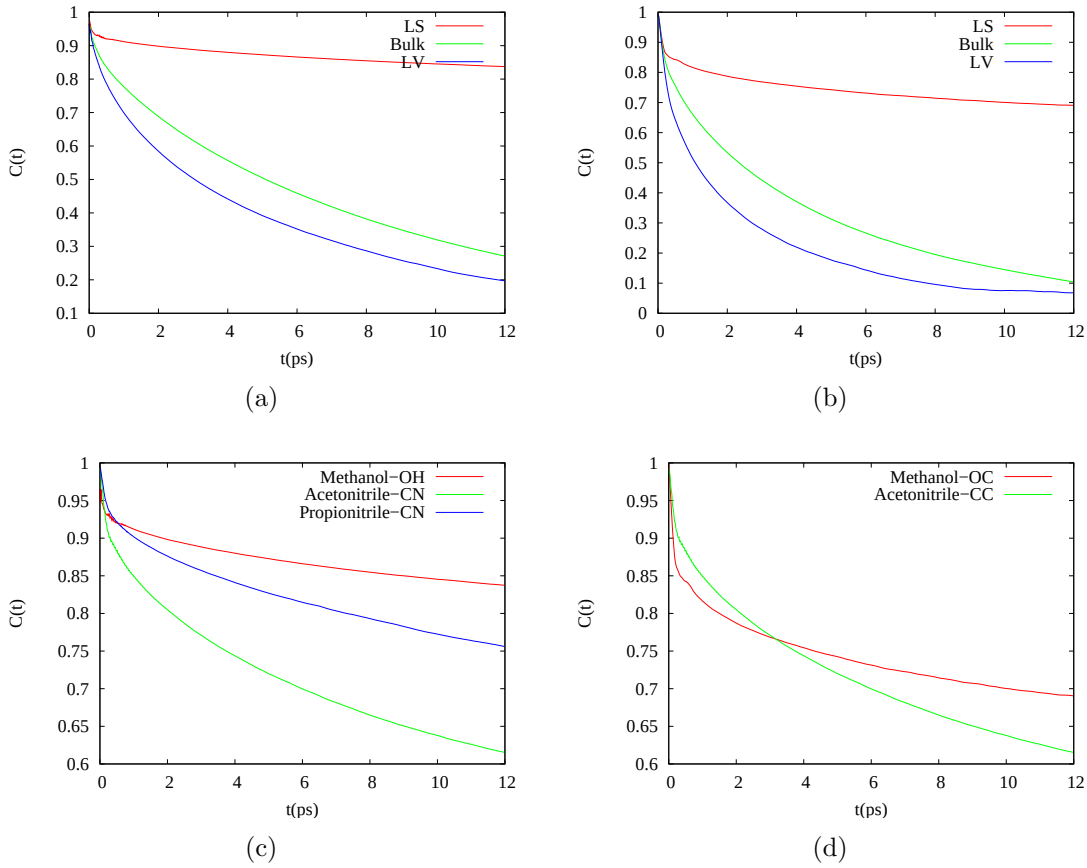

Figure 3.9: (a) Orientational TCFs for methanol OH vector in LS (red), bulk (green) and LV (blue) region. (b) Orientational TCFs for methanol OC vector in LS (red), bulk (green) and LV (blue) region. (c) Comparison of orientational TCFs of polar groups in the LS region: Red: methanol OH bond; Green: acetonitrile CN bond; blue: propionitrile CN bond. (d) Comparison of orientational TCFs of methanol O-C bond (red) and acetonitrile C-C bond (green) in the LS region.

Besides orientational TCFs, we have also calculated the H-bond TCF, which is defined as [60, 61]

$$C_{HB}(t) = \frac{\langle \sum_{ij} s_{ij}(0) \cdot s_{ij}(t) \rangle}{\langle \sum_{ij} s_{ij}(0) \cdot s_{ij}(0) \rangle}, \tag{3.1}$$

where $s_{ij}(t)$ is defined as

$$s_{ij}(t) = \begin{cases} 1 & \text{bonded} \\ \\ 0 & \text{nonbonded.} \end{cases} \tag{3.2}$$

In our calculation, we used the "intermittent"[61] definition of H-bond TCF, i.e. the H-bond pair may break and reconnect during sampling. We have shown profiles of H-bond TCFs in Fig. 3.10, and not to our surprise, the H-bond dynamics is much slower in the LS region, and faster in the LV region than in the bulk. By fitting $C_{HB}(t)$ to an exponential decay form

$$C_{HB}(t) = \exp(-\frac{t}{\tau_{HB}}), \tag{3.3}$$

we can estimate H-bond lifetime τ_{HB} in each region, as given in Table 3.3. Our estimated H-bond life time in the bulk is on the same scale as reported previously[59], while in the LS region, the H-bond lifetime is extremely long.

Region	τ_{HB}(ps)
LS	79.18
Bulk	3.30
LV	2.55

Table 3.3: Estimated H-bond lifetime τ_{HB} for different regions

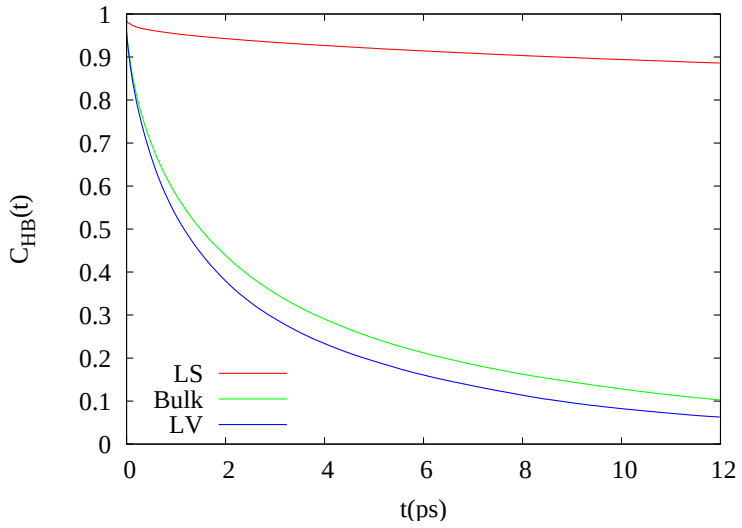

Figure 3.10: Hydrogen bond TCFs in LS (red), bulk (green) and LV (blue) regions

3.6 Electrostatics

A less distinct feature of the methanol density(Fig. 3.2) is that it reaches its bulk value approximately 20 Å away from the surface while inhomogeneities in the acetonitrile density propagate for more than 25 Å. This result implies that surface methanol molecules screen the field from the silica surface more effectively than a surface acetonitrile solvent. To illustrate this point, we have plotted the mobile charge density of the methanol-silica and acetonitrile-silica systems in Fig. 3.11. Methanol molecules acting as both hydrogen bond donors and acceptors to the silica surface generate a large positive peak in the charge density near the surface, followed by a very negative peak (red curve) arising from contributions of the oxygen atoms. This positive-negative structure suggests the formation of a dipole layer that points toward the surface and partially cancels the dipole moments from the surface that point nominally along the surface normal. A consequence of this opposing

dipole structure is that the dipole field does not propagate far into the bulk. In contrast, at the silica-acetonitrile interface, acetonitrile molecules can only accept hydrogen bonds. Thus the induced dipole moments point in the same direction as the surface dipoles, so that the surface dipoles are actually enhanced, leading to a greater influence of the surface dipole field on the acetonitrile liquid structure.

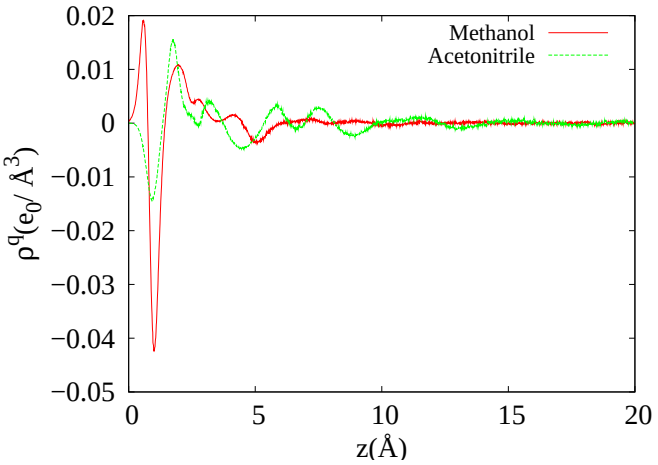

Figure 3.11: Mobile charge density for methanol/silica system (red) and acetonitrile/silica system (green)

3.7 Summary and Conclusions

In this chapter we have performed MD simulations of methanol molecules on a hydrophilic silica surface. As both a hydrogen bond donor and acceptor, the hydrogen bonding between methanol and surface silanol groups are much stronger than what we observed at acetonitrile/silica interface. The average number of hydrogen bonds per molecule is much more than that in bulk methanol. This results in a surface sublayer with extremely high density in which methanol molecules point their methyl groups into the bulk almost perpendicularly. Orientational TCFs also

show much slower reorientation dynamics at the LS interface and this reorientation dynamics is even slower than that at the propionitrile/silica interface, suggesting that hydrogen bonding imposes much greater hindrance to molecular reorientation than hydrophobic interactions of nonpolar groups. Also, the charge density profile shows that near the silica surface methanol molecules form a dipole layer that tends to cancel the dipole field of the silica surface. This causes the inhomogeneity of methanol density to propagate less far into the bulk than acetonitrile. These simulation results are in qualitative agreement with spectroscopy experiment studies.

Chapter 4

LMF Treatment of Charge Inversion System: Structure

4.1 Local Molecular Field Theory for Electrostatic Interactions

To obtain the LMF equation for systems with electrostatic interactions, we consider a nonuniform system with M species of charged particle; the ith species has charge q_i. The spherically symmetric pair interaction between the ith and jth species involves both non-electrostatic and electrostatic components.

$$w_{ij}(r) = w_{\mathrm{ne},ij}(r) + \frac{q_i q_j}{\epsilon r}, \tag{4.1}$$

where ϵ is the dielectric constant. The external potential for the ith species also include non-electrostatic terms and electrostatic interactions

$$\phi_i(\mathbf{r}) = \phi_{\mathrm{ne},i}(\mathbf{r}) + q_i \mathcal{V}(\mathbf{r}), \tag{4.2}$$

where $\mathcal{V}(\mathbf{r})$ is the electrostatic potential from an external charge distribution $\rho^q_{\mathrm{ext}}(\mathbf{r})$.

To construct the mimic system using the LMF theory (Eq. (1.1) and Eq. (1.3)), usually it is advantageous to divide the Coulomb potential $1/r$ into short-

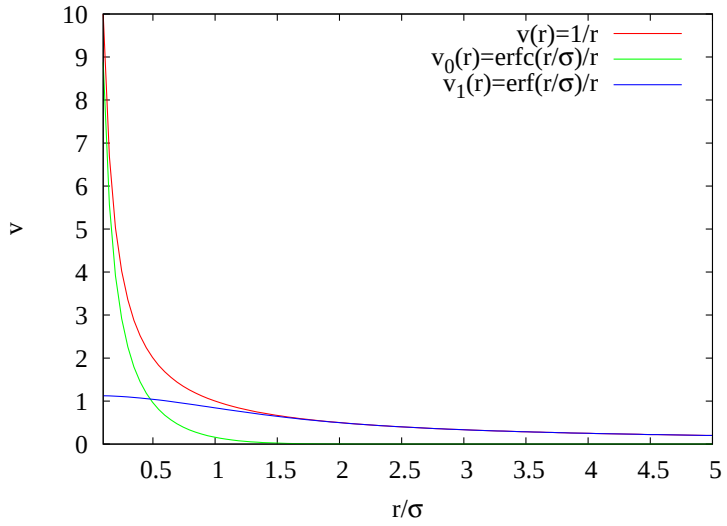

Figure 4.1: Demonstration of $1/r$ potential split with $\sigma = 1$.

and long-ranged parts in the following way:

$$v(r) = \frac{1}{r} = \frac{\text{erfc}(r/\sigma)}{r} + \frac{\text{erf}(r/\sigma)}{r} \equiv v_0(r,\sigma) + v_1(r,\sigma), \tag{4.3}$$

where $\text{erf}(x) = \frac{2}{\sqrt{\pi}} \int_0^x e^{-t^2} dt$ is the error function and $\text{erfc}(x) = 1 - \text{erf}(x)$ is the complementary error function. The parameter σ is a properly chosen length which ensures that $v_0(r)$ contains all the strong nearest neighbor forces and the long-ranged $v_1(r)$ is correspondingly slowly-varying over those characteristic nearest neighbor distances. Here $v_1(r)$ is defined as the electrostatic potential corresponding to a unit Gaussian charge distribution with width σ

$$\rho_G(\mathbf{r}) = \frac{1}{\pi^{3/2}\sigma^3} \exp(-\frac{r^2}{\sigma^2}). \tag{4.4}$$

An example for $\sigma = 1$ of the Coulomb potential separation is given in Fig. 4.1. With such separation of the Coulomb potential, then the short-ranged pair-

pair interaction between the ith and jth species in the mimic system is

$$u_{0,ij}(r) = w_{\mathrm{ne},ij}(r) + \frac{q_i q_j v_0(r)}{\epsilon}, \tag{4.5}$$

and the long-ranged part of the full pair-pair interaction is

$$\begin{aligned} u_{1,ij}(r) &= w_{ij}(r) - u_{0,ij}(r) \\ &= \frac{q_i q_j v_1(r)}{\epsilon}. \end{aligned} \tag{4.6}$$

Then the LMF equation that determines the renormalized external potential for the ith species can be written as

$$\begin{aligned} \phi_{R,i}(\mathbf{r}) &= \phi_i(\mathbf{r}) + \sum_j^M \frac{q_i q_j}{\epsilon} \int d\mathbf{r}' \rho_{R,j}(\mathbf{r}') v_1(|\mathbf{r} - \mathbf{r}'|) \\ &= \phi_i(\mathbf{r}) + \frac{q_i}{\epsilon} \int d\mathbf{r}' \rho_R^q(\mathbf{r}') v_1(|\mathbf{r} - \mathbf{r}'|), \end{aligned} \tag{4.7}$$

where $\rho_{R,j}$ is the singlet density of the jth component and $\rho_R^q = \sum_{j=1}^M q_j \rho_{R,j}$ is defined as the total charge density of mobile species. Since $\phi_i(\mathbf{r})$ can also be separated into non-electrostatic and electrostatic part as shown in Eq. (4.2), the LMF equation (4.7) can be further written as

$$\begin{aligned} \phi_{R,i}(\mathbf{r}) &= \phi_{\mathrm{ne},i}(\mathbf{r}) + q_i [\mathcal{V}(\mathbf{r}) + \frac{1}{\epsilon} \int d\mathbf{r}' \rho_R^q(\mathbf{r}') v_1(|\mathbf{r} - \mathbf{r}'|)] \\ &= \phi_{\mathrm{ne},i}(\mathbf{r}) + q_i \mathcal{V}_R(r), \end{aligned} \tag{4.8}$$

where

$$\mathcal{V}_R(\mathbf{r}) \equiv \mathcal{V}(\mathbf{r}) + \frac{1}{\epsilon}\int d\mathbf{r}'\rho_R^q(\mathbf{r}')v_1(|\mathbf{r}-\mathbf{r}'|) \tag{4.9}$$

is the renormalized electrostatic potential. Eq. (4.9) will be the primary equation we are solving for Coulomb systems.

Since the singlet density ρ_R has an implicit dependence on ϕ_R, it is hard to get ρ_R for a general ϕ_R straightforwardly, and in general we have to use either simulations, or the linear response method[62], which we shall explain later, to iterate the LMF equation and obtain self-consistent solutions of ϕ_R and ρ_R [25, 32], i.e.

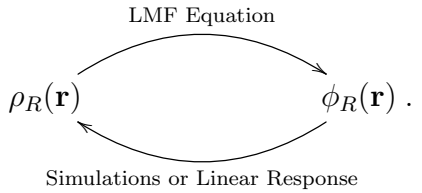

4.2 The Charge Inversion Phenomenon

Charge inversion of colloid and polyelectrolytes is of great interest in biological systems [43, 44]. The problem arises from the observation that when highly charged colloids are placed in multivalent salt solutions, the electrophoretic mobility of the colloid can change sign and therefore they will move in the direction opposite to the one expected based purely on its chemical charge when an external electric field is applied [42, 63, 64], suggesting an unusual distribution of counterions around the colloid. The unusual distribution of counterions can be characterized by the quantity called the "integrated charge", which is the total charge inside a sphere centered at

the origin with radius r, defined as

$$Q(r) = Q_c + \int_0^r dr' 4\pi r'^2 \rho^q(r'), \tag{4.10}$$

where Q_c is the charge of the colloid and ρ^q is the charge density of mobile species. As is shown in Fig. 4.3(a), there is a region where the $Q(r)$ has opposite sign to the charge of the colloid. If the total charge inside the shear plane (usually at the distance of an ion diameter away from the colloid surface[65]) changes sign, then in electrophoresis experiments there will be a mobility reversal, as schematically shown in Fig. 4.2.

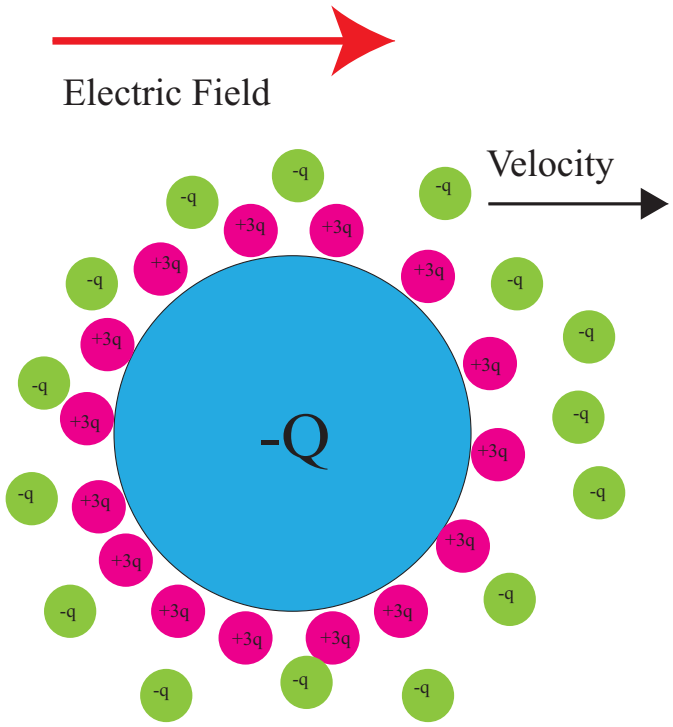

Figure 4.2: A schematic drawing of the model system in our simulations: a colloid with charge $-Q$, +3 counterions and -1 coions. The plot also schematically shows that due to charge inversion from the tightly bound counterions, the colloid will have a mobility reversal, i.e. under an electric field the colloid will move in the direction that is opposite to what is determined by its bare charge.

The usual way of describing the ionic sphere around the colloid is the classical electrical double layer (EDL) model [66], which makes use of the mean-field Poisson-Boltzmann (PB) method. The PB method always predicts a monotonic decay of the induced charge density and thus never shows an effective charge with opposite sign. After all, the PB has neglected correlations between all charged species and therefore can be valid only for dilute and weak-coupling systems. In the case of overcharging of a colloid, the change of sign of the effective charge results from strong correlations between positive and negative charges. Therefore, in order to explain this counter-intuitive phenomenon, a new theory must take into account electrostatic correlations.

A number of theories have been suggested to explain this phenomenon. Based on an analogy to Wigner-Crystals (WC), Shklovskii and coworkers [43, 67, 68] suggest that the counterions form a strongly correlated liquid at the surface of the colloid and the correlations between these ions in the liquid layer induce extra counterions to be absorbed to the surface of the colloid, leading to overcharging. This Wigner-Crystal based theory yields accurate results at low temperature ($T \to 0$) and in the strong coupling limit (high counterion density and valence). Its applications has also been extended to more complicated circumstances in further work [44, 69]. However, the WC approach is based on the one-component plasma (OCP), consisting of point charges in a uniform neutralizing background . In fact the phenomenon of overcharging is a synergic effect, and many parameters, such as excluded volume and concentration of monovalent salt [70], may come into play as well. For example, Holm and coworkers have illustrated the influence of excluded volumes

[71] on charge inversion and incorporated this effect into Density Functional Theory (DFT) [72]. All these factors can be handled by the LMF theory in a proper way. Nonetheless, for simple systems not involving multiple salts and polyelectrolytes, electrostatic correlations still play a major role in charge inversion. Therefore, in our LMF study we will mainly focus on such correlations, even though other factors such as excluded volume have also been incorporated into the theory implicitly.

4.3 Simulation Details

The model system is built up based on the previous work by Levin and coworkers[65]. The model system consists of a charged colloid with radius $R_c = 30$ Å and charge -110q placed at the center of a cubic simulation box, which contains 883 counterions with charge +3q and 2539 coions with charge -1q to ensure global neutrality, where q is the charge of the proton. A schematic plot of the model system is given in Fig. 4.2. For treatment of electrostatic interactions, standard Ewald sums[36] were used. The screening parameter for the Ewald summation is 0.0308 Å^{-1}, and the number of k-space vectors for Ewald summation are 8, 8 and 8 for x, y,z directions, respectively. Besides electrostatic interactions, the repulsive core repulsions between ions are described by the Weeks-Chandler-Andersen (WCA) potential[73], and all the ions have the same WCA parameters, with $\sigma_{\mathrm{WCA}} = 4.0$ Å and $\epsilon_{\mathrm{WCA}} = 2.4775$ kJ/mol. The strong repulsion between the colloid and ions is

defined by the shifted WCA potential.

$$\phi_{\rm ne}(\mathbf{r}) = \begin{cases} 4\epsilon_{rep}[(\frac{\sigma_{rep}}{r-R_c})^{12} - (\frac{\sigma_{rep}}{r-R_c})^{6}] + \epsilon_{rep} & \text{if } r \leq 2^{\frac{1}{6}}\sigma_{rep} + R_c \\ 0 & \text{if } r > 2^{\frac{1}{6}}\sigma_{rep} + R_c \end{cases} \tag{4.11}$$

Here σ_{rep} = 2.0 Å and ϵ_{rep} = 183.13 kJ/mol, which ensures that cations won't penetrate the shell of the colloid.

MD simulations are performed in the isothermal-isobaric (NPT) ensemble using the DL_POLY 2.16 package with T = 298 K. In the full system with Ewald summation, the pressure is 7.37 atm, while for the mimic system, the pressure is 7.59 atm. Our choice of pressure in both full and mimic system will ensure that at the edge of the simulation box, the concentration of +3 counterions will be equal to 0.106 M, which is the same as that used in Ref. [65]. The Berendsen thermostat and barostat [74] was used to control the temperature and pressure, with relaxation time 0.5 ps for the thermostat and 0.1 ps for the barostat. The volume of the simulation box is allowed to vary during the simulation and in equilibrium the average box length is about 240 Å. The cutoff distances for the Van der Waals and the short-ranged part of the Ewald summation were both 110 Å. We set the dielectric constant ϵ = 78 to represent the aqueous solution environment. The system has been equilibrated for 15 ps with timestep of 0.5 fs. After the equilibration, configurations of the system were recorded every 5 fs. The total sampling lasted for 200,000 steps and gave a trajectory file with a total of 20,000 configurations for analysis.

4.4 Results from Ewald Summation

The simulation using Ewald summation calculating electrostatic interactions serves as the benchmark for simulations in the mimic system. Results of simulations in the full system are briefly summarized in Fig. 4.3. For reference purpose we also give the charge density from linearized PB, i.e. the Debye-Hückel theory[75]

$$\rho_D^q(r) = -\frac{Q_c e^{-\frac{r}{\lambda_D}}}{4\pi\lambda_D^2 r} \cdot \frac{e^{\frac{R_{\text{eff}}}{\lambda_D}}}{1+\frac{R_{\text{eff}}}{\lambda_D}}, \tag{4.12}$$

where $R_{\text{eff}} = R_c + \frac{\sigma_{\text{WCA}}}{2}$ is the effective radius of the colloid and λ_D is the Debye length

$$\lambda_D = \sqrt{\frac{k_B T\epsilon}{\rho_+ q_+^2 + \rho_- q_-^2}}, \tag{4.13}$$

where ρ^+ and ρ^- are the densities of plus and minus ions, and q^+ and q^- are the charges of plus and minus ions respectively. In our case $\lambda_D = 3.80$ Å.

As shown in Fig. 4.3, the simulation results give complete features of overcharging. First of all, the integrated charge profile (Fig. 4.3(a)) shows a region near the colloid with charge reversal, while this is not predicted by the linearized PB. When it comes to ion densities, Fig. 4.3(b) shows that the overcharging comes from the extreme high density of counterions (more than 50 times of the bulk density) near the colloid. Moreover, the mobile charge density (Fig. 4.3(c)) near the colloid is greater than the absolute value of the colloid surface charge density, thus giving charge inversion. Moreover, the integrated charge $Q(r)$ will go back to zero after having reached its maximum, and this suggests that correspondingly the mobile

charge density will cross over zero and become negative after a given point, as is shown in the inset of Fig. 4.3(c). However, such crossover of charge density is not predicted by the linearized PB, which only decays monotonically.

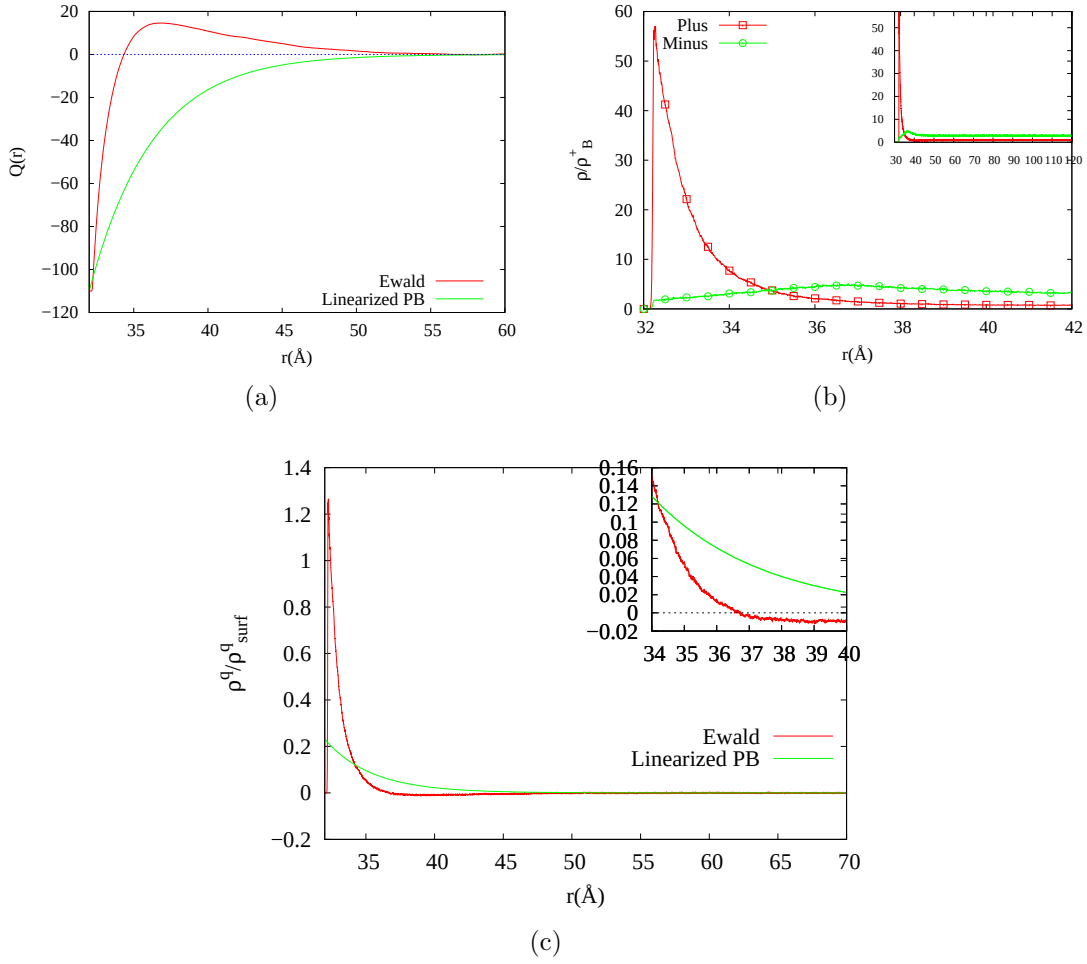

Figure 4.3: (a) The integrated charge of the full system with Ewald summation (red) and the one obtained from linearized PB (green). (b) The plus (red square) and minus (green circle) ion density, both of which has been scaled by the bulk density of plus ion, ρ_B^+. The inset figure gives the density profile in the whole system. (c) The mobile charge density of the full system with Ewald summation (red) and the one obtained from the linearized PB (green). The inset figure gives the charge density profile between 34 Å and 40 Å. The charge density has been scaled by the surface charge density of the colloid, ρ^q_{surf}.

4.5 Strong-coupling Approximation

To solve the LMF equation (4.9), a proper separation of the Coulomb potential using Eq. (4.3) is necessary. Here we have chosen $\sigma = 2.5a = 26.828$ Å as the parameter for Coulomb potential split, where a is the nearest neighbor distance defined as

$$\frac{4}{3}\pi a^3(\rho^+ + \rho^-) = 1. \tag{4.14}$$

We will see later that $\sigma = 2.5a$ is not the minimum σ we can use, actually with $\sigma = 2a = 21.462$ Å we may also reach the self-consistent solution of the LMF equation (4.9).

For convenience, usually the starting point of the LMF iteration process is to approximate the renormalized electrostatic potential $\mathcal{V}_R(\mathbf{r})$ with only the short-ranged part of the external electrostatic potential, which we called $\mathcal{V}_0$, and this approximation is called the "Strong-coupling approximation" (SCA). To be more specific, in our model system, the external electrostatic potential is

$$\begin{aligned}\mathcal{V}(\mathbf{r}) &= \frac{Q_c}{\epsilon r} \\ &= \frac{1}{\epsilon}\int d\mathbf{r}'\rho^q_{\text{ext}}(\mathbf{r}')\frac{1}{|\mathbf{r}-\mathbf{r}'|},\end{aligned} \tag{4.15}$$

where $\rho^q_{\text{ext}}(\mathbf{r})$ is the external charge density from the colloid

$$\rho^q_{\text{ext}}(\mathbf{r}) = \frac{Q_c}{4\pi R_c^2}\delta(r - R_c), \tag{4.16}$$

which represents the charge distribution with charge Q_c uniformly smeared over the colloid surface. Then the $\mathcal{V}_0(\mathbf{r})$ in SCA is the convolution of $\rho^q_{\text{ext}}(\mathbf{r})$ and $v_0(\mathbf{r})$

$$\begin{aligned}\mathcal{V}_0(\mathbf{r}) &= \frac{1}{\epsilon}\int d\mathbf{r}'\rho^q_{\text{ext}}(\mathbf{r}')v_0(|\mathbf{r}-\mathbf{r}'|) \\ &= \frac{1}{r\epsilon} - \frac{1}{2rR_c\epsilon}[(r+R_c)\,\text{erf}(\frac{r+R_c}{\sigma}) + \frac{\sigma}{\sqrt{\pi}}e^{-(\frac{r+R_c}{\sigma})^2} \\ &- (r-R_c)\,\text{erf}(\frac{r-R_c}{\sigma}) - \frac{\sigma}{\sqrt{\pi}}e^{-(\frac{r-R_c}{\sigma})^2}]. \end{aligned} \tag{4.17}$$

The simulation of SCA serves not only as a starting point of the iterative solution to the LMF equation, but also a good estimate of the structure of the model system. This is because there is a cancellation of long-ranged forces in the full system and SCA can sometimes give a very good description of the static structure, especially in the bulk[25]. In Fig. 4.4, we have shown results from SCA simulations. At first glance, both ion densities and charge densities of SCA are in good agreement with results from Ewald summation. This is not surprising because overcharging is induced by strong counterion-counterion and counterion-colloid correlations, and in SCA we have chosen a σ that is large enough to incorporate most nearest neighbor correlations.

However, in Fig. 4.4(a) and Fig. 4.4(c), the peak of cation density and mobile charge density in SCA is lower than that of Ewald, showing that SCA did not get enough counterions in the layer closest to the colloid surface because of the neglect of long-ranged interactions. Moreover, such defects in densities can be magnified by the integrated charge profile in Fig. 4.4(d), in which SCA indeed shows overcharging,

but its $Q(r)$ is unable to go back to zero as r increases, even when r has reached the edge of the simulation box. This can be illustrated with the help of Fig. 4.5. By constructing the cubic simulation box we have already imposed a global neutrality condition to the system. In other words, the whole simulation box would be neutral at all times. However, when we integrate the charge density radially, even if we have reached the edge of the simulation box as shown in Fig. 4.5 where the blue sphere represents the region of integration, we still could not get the total charge inside the blue sphere to be zero. This indicates that there is one or more counterions lingering at the corner of the cubic simulation box, represented by red spheres in Fig. 4.5. These "ghost" counterions missing from the blue sphere result in incomplete screening of the colloid and failure to get local neutrality.

Therefore by only considering the short-ranged part of Coulomb interactions in the mimic system we could not get the correct counterion density, though SCA works perfectly well for bulk liquids. The failure of SCA has also observed in other nonuniform systems such as Gaussian-truncated water molecules between hydrophobic walls[30], where SCA did not get the correct dipole layering in the bulk. Thus the long-ranged part of $\mathcal{V}_R$ is required to generate the correct electrostatic structure in the SCA system.

4.6 Full Solution to the LMF Equation

As mentioned in Section 4.1, the LMF equation for $\mathcal{V}_R(\mathbf{r})$ (Eq. (4.9)) for the model system will be solved via iterations. Since the starting point of our iteration

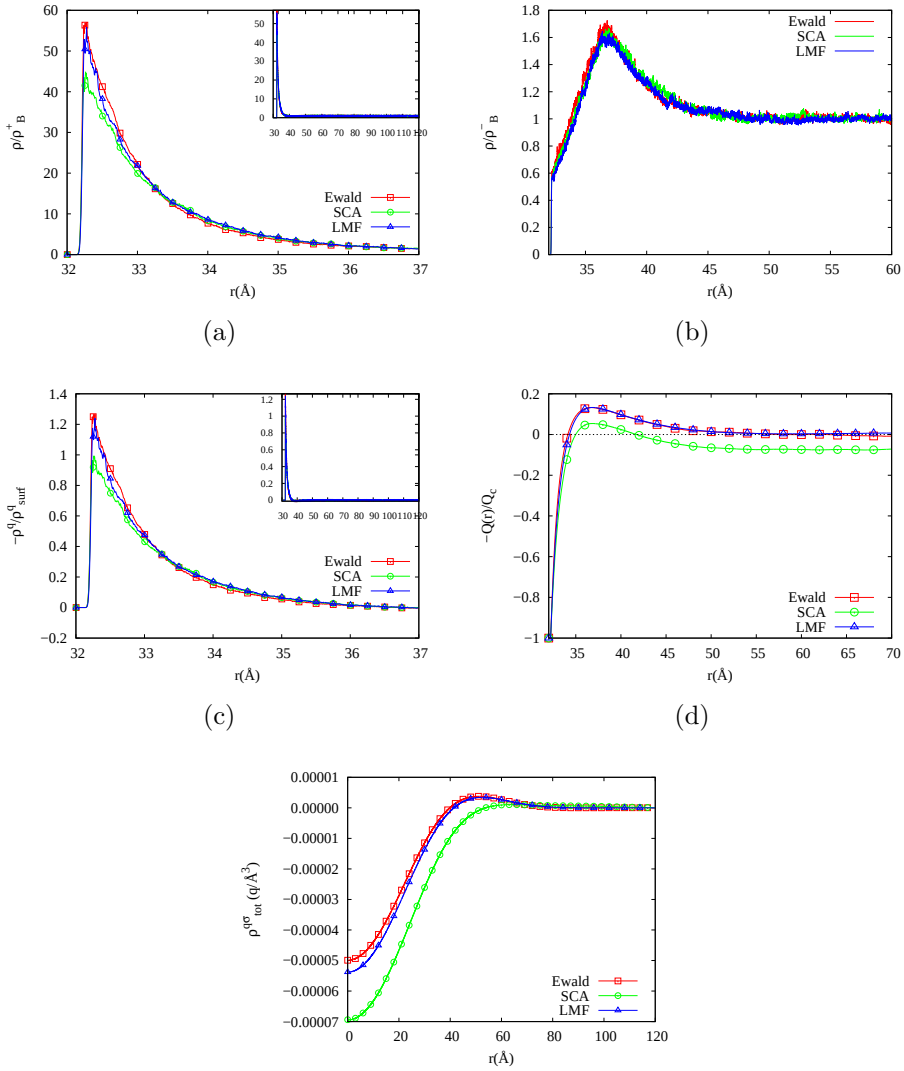

Figure 4.4: (a) The plus ion density for system with full Ewald summation (red square), SCA (green circle) and self-consistent LMF solution via simulations (blue triangle). The density has been scaled by the bulk plus ion density ρ_B^+. The inset figure gives the density profile in the whole system. (b) The minus ion density for system with full Ewald summation (red), SCA (green) and self-consistent LMF solution via simulations (blue). The density has been scaled by the bulk minus ion density ρ_B^-. (c) The mobile charge density for system with full Ewald summation (red square), SCA (green circle) and self-consistent LMF solution via simulations (blue triangle). The charge density has been scaled by the surface charge density of the colloid, ρ_{surf}^q. The inset figure gives the density profile in the whole system. (d) The integrated for system with full Ewald summation (red square), SCA (green circle) and self-consistent LMF solution via simulations (blue triangle). $Q(r)$ has been scaled by the charge of the colloid with a negative sign, $-Q_c$. (e) The Gaussian-smoothed charge density for system with full Ewald summation (red square), SCA (green circle) and self-consistent LMF solution via simulations (blue triangle).

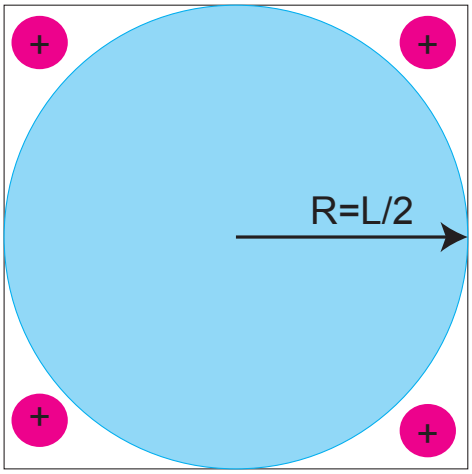

Figure 4.5: An illustration of SCA's failure to get neutrality. When we integrate the total charges in the simulation box radially, even when we have reached the edge of the simulation the box (shown by the blue sphere), the total charge inside sphere is not zero. Therefore there are on average one or more cations staying at the corner of the cubic box, which should not be the case if the charge of the colloid has been completely screened.

is SCA, where $\mathcal{V}_R(\mathbf{r}) \simeq \mathcal{V}_0(\mathbf{r})$, we just need to find the long-ranged part of $\mathcal{V}_R$, which we called $\mathcal{V}_{R1}$. This means that the LMF equation (4.9) can be further written as

$$\mathcal{V}_R(\mathbf{r}) = \mathcal{V}_0(\mathbf{r}) + \mathcal{V}_{R1}(\mathbf{r}), \tag{4.18}$$

with

$$\begin{aligned} \mathcal{V}_{R1}(\mathbf{r}) &= \frac{1}{\epsilon} \int d\mathbf{r}' \rho^q_{R,tot}(\mathbf{r}') \cdot v_1(|\mathbf{r} - \mathbf{r}'|) \\ &= \frac{1}{\epsilon} \int d\mathbf{r}' \rho^{q\sigma}_{R,tot}(\mathbf{r}') \cdot \frac{1}{|\mathbf{r} - \mathbf{r}'|}, \end{aligned} \tag{4.19}$$

where $\rho^q_{R,tot}(\mathbf{r}) = \rho^q_R(\mathbf{r}) + \rho^q_{ext}(\mathbf{r})$ is the total charge density that includes both the mobile charge density and charge density from the external charge distribution,

and $\rho^{q\sigma}_{R,tot}$ is what we called the Gaussian-smoothed charge density, which is the convolution of the total charge density and a Gaussian charge distribution ρ_G with width σ

$$\rho^{q\sigma}_{R,tot}(\mathbf{r}) \equiv \int d\mathbf{r}' \rho^{q}_{R,tot}(\mathbf{r}')\rho_G(|\mathbf{r}-\mathbf{r}'|). \tag{4.20}$$

The Gaussian smoothing removes most of the simulation noise in the bare charge density and more clearly displays the underlying electrostatics. Note that the magnitude of the smoothed charge density depends on our choice of σ, and here is more than three orders of magnitude smaller that the bare charge density[5, 30, 45]. Defects in the SCA's charge density can be more clearly identified by Gaussian smoothing. For example, in our system, although the charge density of SCA is only slightly different from that of Ewald(Fig. 4.4(c)), the smoothed charge density deviates substantially from that of Ewald (Fig. 4.4(e)).

Eq. (4.19) can also be written in the form of Poisson's equation

$$\nabla^2 \mathcal{V}_{R1}(\mathbf{r}) = -\frac{4\pi}{\epsilon}\rho^{q\sigma}_{R,tot}(\mathbf{r}). \tag{4.21}$$

In other words, solving the full LMF equation is to equivalent to finding the self-consistent solution of Poisson's equation with a Gaussian-smoothed charge density.

4.6.1 Solving LMF Equation via Simulations

An iterative solution to the LMF equation via simulations is the most straightforward way of solving the equation. By updating ϕ_R and ρ_R in the LMF equation

after each simulation converged solutions can be reached. Here we discuss such an iterative solution of the LMF equation for our model system using simulations with SCA as the starting point. In the next subsection we will discuss a much more efficient way of solving the LMF equation, but several technical issues are best understood using standard iteration. In particular, solving the LMF equation (4.19) in systems with Coulomb interactions should be handled with care. This is because the starting point of the iteration process, e.g. the SCA, whose charge density does not get the zeroth and higher moments correct[25, 76], may have difficulties in getting the iteration process to converge. Therefore, we have used the so-called "stable" iteration method, as described in detail in Appendix A, to iterate the LMF equation. The "stable" iteration method will drive the total charge density toward neutrality.

Results from simulations in the mimic system with self-consistent LMF solutions are also given in Fig. 4.4, shown by the blue curve in each plot. The solution given here is the one after three iterations, which has already converged. We can see that full LMF has successfully corrected the defect in counterion density and charge density near the colloid, and maintains neutrality in the integrated charge curve(Fig. 4.4(d)).

One technical issue with simulations in full LMF system is the size of fluctuations. This can be shown by the integrated charge profile at a smaller scale. As is shown in Fig. 4.6, we have performed simulations in full LMF system for multiple runs. For each run we use the same the renormalized electrostatic potential $\mathcal{V}_R$ but different initial configurations, and all the runs lasted for 15 ps. For each run, the integrated charge $Q(r)$ has greater oscillations in the bulk ($r > 70$ Å) than the

Ewald, which was also run for 15 ps. This suggest that there exist greater density fluctuations in the full LMF system than Ewald. Such density fluctuations persist as r increases, as a result, we may seem to find that $Q(r)$ is not exactly zero at the edge of the simulation box for the full LMF system and it can be either positive or negative due to the randomness of fluctuations. Therefore, to reconcile this issue and make $Q(r)$ approach zero at the edge of the simulation box, usually we run several parallel simulations and average over them to cancel the fluctuations[32]. In fact the $Q(r)$ profile in Fig. 4.4(d) is also obtained by averaging over 10 parallel simulations.

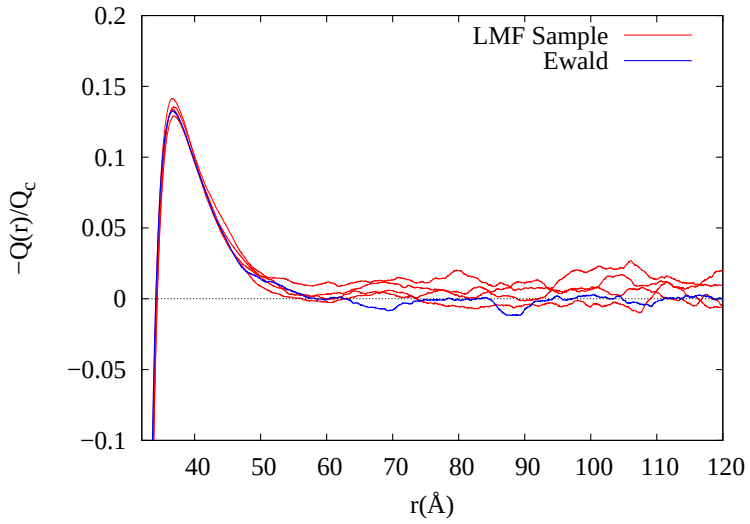

Figure 4.6: The integrated charge of Ewald (blue) and LMF runs with the same $\mathcal{V}_R$ but different initial configuration (red).Greater fluctuations in the LMF system is visible.

We may also observe greater energy fluctuations in the full LMF system by calculating the probability distribution of Φ_{R1}, the total long-ranged potential energy of the system with detailed definition in Eq. (4.24). In Fig. 4.7 we have plotted the probability distribution of $\beta\Phi_{R1}$ in full LMF system and Ewald system,

where $\beta = 1/k_BT$. Apparently $P(\beta\Phi_{R1})$ in both systems are Gaussian with the same mean, but the width of Gaussian in LMF system is larger than that of Ewald, indicating greater energy fluctuations.

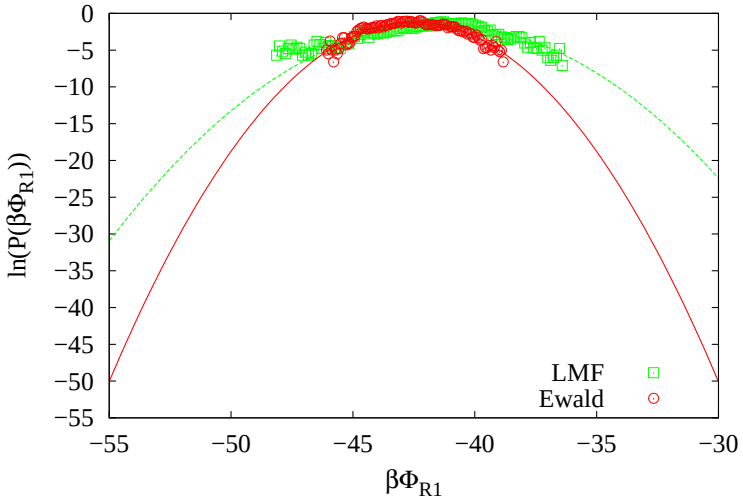

Figure 4.7: Probability distribution of Φ_{R1} in Ewald (red) and LMF (green) configurations. Lines are drawn by fitting $\ln(P(\beta\Phi_{R1}))$ to a parabola function.

Greater fluctuations in the LMF system than in Ewald have also been observed previously[32], for water between walls. As discussed in Ref. [32], for any instantaneous charge density fluctuations, the long-ranged forces originating from these fluctuations will have a damping effect and tend to pull the instantaneous configuration back to the equilibrium state. In the Ewald summation, the instantaneous fluctuations are duplicated on all images and thus will have an overdamping effect on the fluctuations. This overdamping is in part an artifact of the strictly periodic images used in the Ewald sums. However, in short-ranged LMF systems, the influence of long-ranged forces has been averaged and represented by the static $\mathcal{V}_R$. Thus there are no long-ranged forces from instantaneous fluctuations that drive

the system back to equilibrium.

Therefore, the fluctuations in the LMF systems may drive the r-dependent charge density away from neutrality slightly. To obtain better neutrality, averaging over an ensemble of simulations might be needed. This is not a very efficient way to obtain the structure of the system if accuracy is required. To overcome this shortcoming, in the next section, we use the linear response method to iterate the LMF equation and our results show that charge density with neutrality can be obtained in a quick and accurate way.

4.6.2 Solving LMF Equation via Linear Response

Solving the LMF equation via simulation may take several simulations to get self-consistency, as shown in the last section. However, if the initial guess of the LMF solution, e.g. SCA, already gives a very good estimation of the structure, then it is possible that the LMF equation could be iteratively solved using configurations from the initial guess based on static linear response theory[62], without doing further simulations.

First start with the singlet density of the ith species in SCA written in the form of an ensemble average over microscopic configurations

$$\rho_i(\mathbf{r};[\{\phi_{0,i}\}]) \equiv \langle \rho_i(\mathbf{r},\overline{\mathbf{R}})\rangle_{\phi_0}, \tag{4.22}$$

where $\overline{\mathbf{R}} \equiv \{\mathbf{r}_i\}$ denotes the microscopic configuration of all particles and $\rho_i(\mathbf{r},\overline{\mathbf{R}})$

is the microscopic density

$$\rho_i(\mathbf{r}, \overline{\mathbf{R}}) \equiv \sum_{j=1}^{N_i} \delta(\mathbf{r} - \mathbf{r}_{i,j}), \tag{4.23}$$

where N_i is total number of particles for the ith species. Now consider the full LMF system with long-ranged correction $\{\phi_{R1,i}(\mathbf{r})\}$. The total potential energy associated with $\{\phi_{R1,i}(\mathbf{r})\}$ in a microscopic configuration is

$$\Phi_{R1}(\overline{\mathbf{R}}) = \sum_{i=1}^{M} \int d\mathbf{r} \rho_i(\mathbf{r}, \overline{\mathbf{R}}) \phi_{R1,i}(\mathbf{r}). \tag{4.24}$$

Similarly, by defining $U_0(\overline{\mathbf{R}})$ as the total intermolecular potential energy and $\Phi_0(\overline{\mathbf{R}})$ as the total potential energy from $\{\phi_{0,i}\}$ for a microscopic configuration $\overline{\mathbf{R}}$, we may write the density of the ith species in the full LMF system as ensemble averages in the SCA system

$$\begin{aligned} \langle \rho_i(\mathbf{r}, \overline{\mathbf{R}}) \rangle_{\phi_R} &= \frac{\int d\overline{\mathbf{R}} \rho_i(\mathbf{r}, \overline{\mathbf{R}}) e^{-\beta[U_0(\overline{\mathbf{R}}) + \Phi_0(\overline{\mathbf{R}}) + \Phi_{R1}(\overline{\mathbf{R}})]}}{\int d\overline{\mathbf{R}} e^{-\beta[U_0(\overline{\mathbf{R}}) + \Phi_0((\overline{\mathbf{R}}) + \Phi_{R1}(\overline{\mathbf{R}})]}} \\ &= \frac{\langle \rho_i(\mathbf{r}, \overline{\mathbf{R}}) e^{-\beta \Phi_{R1}(\overline{\mathbf{R}})} \rangle_{\phi_0}}{\langle e^{-\beta \Phi_{R1}(\overline{\mathbf{R}})} \rangle_{\phi_0}}. \end{aligned} \tag{4.25}$$

Eq. (4.25) is an exact expression for singlet densities in the full LMF system. Usually averaging over exponentials as in Eq. (4.25) is difficult and some special techniques such as umbrella sampling[36] are needed. However, in our case, there is good overlap between the configurations of SCA and that of full LMF, as we shall show later. Therefore it is possible to use Eq. (4.25) together with the LMF

equation to obtain the self-consistent solution. Furthermore, by defining $\delta\Phi_{R1}(\overline{\mathbf{R}}) \equiv \Phi_{R1}(\overline{\mathbf{R}}) - \langle\Phi_{R1}(\overline{\mathbf{R}})\rangle_{\phi_0}$ and $\delta\rho_i(\mathbf{r},\overline{\mathbf{R}}) \equiv \rho_i(\mathbf{r},\overline{\mathbf{R}}) - \langle\rho_i(\mathbf{r},\overline{\mathbf{R}})\rangle_{\phi_0}$, Eq. (4.25) can be linearized

$$\langle\rho_i(\mathbf{r},\overline{\mathbf{R}})\rangle_{\phi_R} \simeq \langle\rho_i(\mathbf{r},\overline{\mathbf{R}})\rangle_{\phi_0} - \beta\langle\delta\rho_i(\mathbf{r},\overline{\mathbf{R}})\delta\Phi_{R1}(\overline{\mathbf{R}})\rangle_{\phi_0}. \tag{4.26}$$

This is the linear response (LR) formula we are using to iterate the LMF equation.

With Eq. (4.26), we have iterated the LMF equation using the trajectory file of SCA with 20000 configurations. For a single trajectory file, the iteration process was performed 100 times to ensure convergence. To ensure accuracy, we may further run another simulation using the $\mathcal{V}_{R1}$ obtained from previous iteration, and use the configurations of the simulation to do a second linear response iteration. Results from both the first and the second LR iterations are shown in Fig. 4.8. First we have shown the probability distribution of Φ_{R1} in configurations of SCA and that from simulation after the 1st LR. Clearly both distributions can be approximated by a Gaussian and the overlap between two distributions is sufficient to ensure that either Eq. (4.25) or (4.26) can work effectively to calculate the density response to the change of external field using configurations of SCA. For the integrated charge $Q(r)$ (Fig. 4.8(b)), the first LR is in good agreement with the Ewald at the peak of the curve and maintains neutrality, though some oscillations in the bulk are still visible. The second LR has corrected the first LR a bit, in both integrated charge and Gaussian-smoothed charge density, but in general the first LR has already reached a very good solution to the LMF equation, in terms of both the charge density and $\mathcal{V}_{R1}$ (Fig. 4.8(d)).

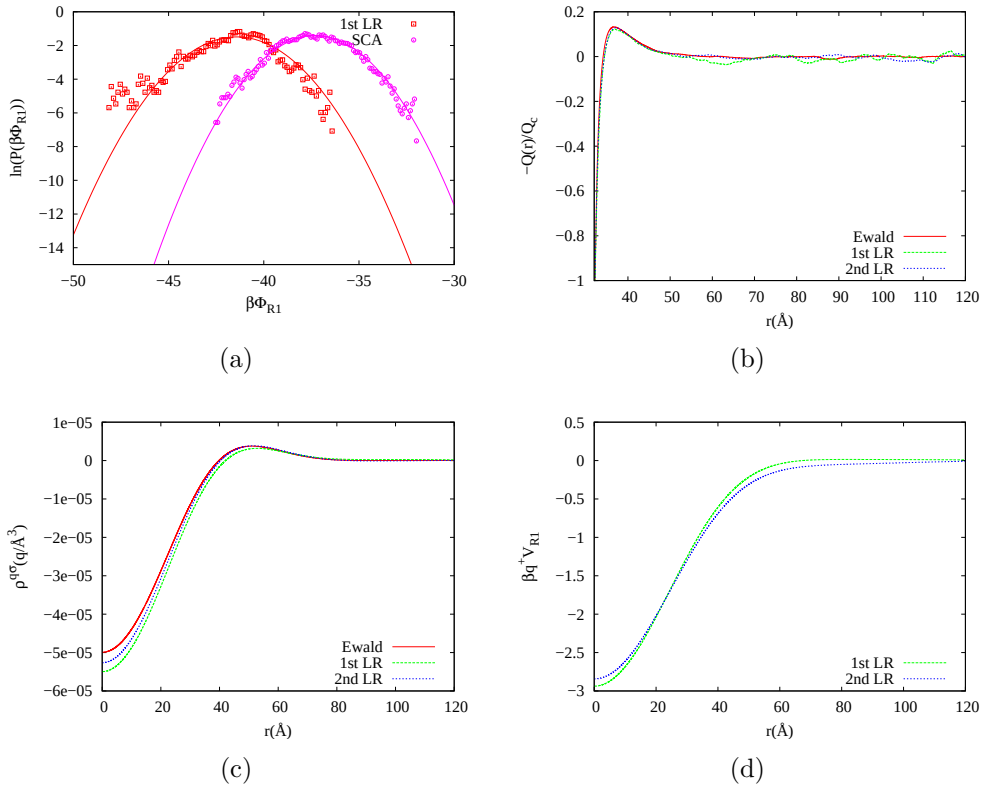

Figure 4.8: (a) Probability distributions of Φ_{R1} in configurations of SCA (magenta) and the simulation after the 1st LR iteration (red). Lines are drawn by fitting $\ln(\beta P(\Phi_{R1}))$ to a parabola function. (b) Integrated charge for Ewald (red), first linear response iteration (green) and second linear response iteration (blue). (c) Gaussian-smoothed charge density for Ewald (red), first linear response iteration (green) and second linear response iteration (blue). (d)Long-ranged part of potential energy for the first linear response (green) and second linear response iteration (blue).

In general, iterations via linear response gives much faster convergence by avoiding iteration through simulations. Moreover, inside the linear response iteration loop, the "stable" iteration method was used and this will force the charge density to conserve neutrality. Unlike iteration via simulations, where charge densities are calculated by sampling the instantaneous configurations and density fluctuations may produce apparent non-neutrality, the linear response method determines the "theoretical" charge density by modifying existing densities based on the sys-

tem's response to the perturbation from changes in external field. This reduces the random fluctuations and the predicted density better maintains neutrality.

4.6.3 The Choice of σ and Separation of Coulomb Potential

To ensure the convergence of LMF iterations, the separation of the Coulomb potential $v(r) = v_0(r;\sigma)+v_1(r;\sigma)$ should ensure that $v_0(r)$ includes the short-ranged forces and $v_1(r)$ is slowly varying over the nearest neighbor distances. Therefore the choice of σ should be at the scale of the average nearest neighbor distance, a. We have tested different choices of σ and found that the minimum σ that ensures convergence is $\sigma_{min} = 2a = 21.462$ Å. Choosing a smaller σ would allow for smaller cutoff radius in simulations and thus accelerate the speed of simulations. However, there is a tradeoff between the speed of simulation and the speed of convergence. A small σ would take more iterations to achieve convergence. In Fig. 4.9(a) we have shown the integrated charge of the mimic system with $\sigma = 21.462$ Å. It seems that at least two LR iterations are needed to obtain a good $Q(r)$, unlike the case of $\sigma = 26.828$ Å in Fig. 4.8(b), where only one LR iteration seems to be good enough.

The slower convergence for $\sigma = 21.462$ Å could also be interpreted with the help of the probability distribution of Φ_{R1}. In Fig. 4.9(b), we have plotted the probability distribution for $\beta\Phi_{R1}$ in configurations of SCA and configurations of the simulation after the 2nd LR. At first glance both two distributions are Gaussian and they overlap with each other. However, we could measure the overlapping between the $P(\Phi_{R1})$ of SCA, represented by $P_{\mathrm{SCA}}(\Phi_{R1})$ and that of the full LMF

system, represented by $P_{\phi_{R1}}(\Phi_{R1})$, by calculating the relative entropy[77, 78], which is defined as

$$D[P_{\rm SCA}(\Phi_{R1})||P_{\phi_{R1}}(\Phi_{R1})] \equiv \int d\Phi_{R1} P_{\rm SCA}(\Phi_{R1}) \ln[\frac{P_{\rm SCA}(\Phi_{R1})}{P_{\phi_{R1}}(\Phi_{R1})}] \geq 0 \qquad (4.27)$$

$D = 0$ is the case that two distributions are identical and $D \gg 1$ suggests there is little overlap between the two. We have calculated the relative entropy for the two distributions given in Fig. 4.9(b), and this gives $D = 3.3255$, while the relative entropy for case with $\sigma = 26.828$ Å, is 2.7441 for the two distributions in Fig. 4.8(a). This indeed indicates that there is more overlapping in configuration space between SCA and the full LMF system, therefore the iterations with $\sigma = 26.828$ Å converge faster.

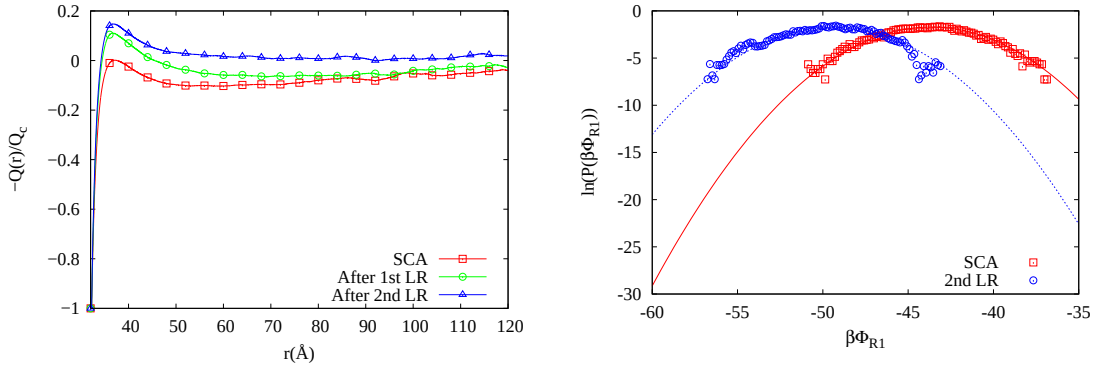

(a) (b)

Figure 4.9: (a)The integrated charge for mimic system with $\sigma = 21.462$ Å: SCA (red), simulation after the 1st LR (green) and simulation after the 2nd LR (blue). (b)Probability distribution of Φ_{R1} in configurations of SCA (red) and the simulation after the 2nd LR iteration (red) for mimic system with $\sigma = 21.462$ Å. Lines are draw by fitting $\ln(\beta P(\Phi_{R1}))$ to a parabola function.

Another issue with the Coulomb potential separation is the separation of the external Coulomb potential $\mathcal{V}(\mathbf{r}) = Q_c/\epsilon r$. In our previous discussion in Section 4.5,

we assumed that $\mathcal{V}(\mathbf{r})$ was generated from an external charge distribution ρ^q_{ext} that smears charge of Q_c uniformly over the spherical surface with radius R_c, expressed in Eq. (4.16), and then the $\mathcal{V}_0(\mathbf{r})$ in SCA is obtained by convoluting the ρ^q_{ext} with $v_0(r)$. However, according to the Gauss's law, as long as the total charge inside the sphere with radius R_c is Q_c, the electrostatic potential outside the sphere will be $\mathcal{V}(\mathbf{r})$, irrespective the specific form of the charge density ρ^q_{ext}. Therefore it is natural to think about the case where $\mathcal{V}(\mathbf{r})$ is generated purely by a point charge Q_c placed at the origin, and the $\mathcal{V}_0(\mathbf{r})$ in SCA is just

$$\mathcal{V}_0(\mathbf{r}) = \frac{Q_c}{\epsilon} v_0(r;\sigma). \tag{4.28}$$

This $\mathcal{V}_0(\mathbf{r})$ does not seem to be a very good choice, because if we compare this $\mathcal{V}_0(\mathbf{r})$ with $\sigma = 26.828$ Å with the one we used previously in Eq. (4.17) in Fig. 4.10(a), we see that the magnitude of this new $\mathcal{V}_0(\mathbf{r})$ is much smaller than the one we previously used. However, only the full Coulomb potential obeys Gauss' law and the convergence of an approximate theory like LMF theory depends on the choice of $\mathcal{V}_0$ and $\mathcal{V}_1$, where $\mathcal{V}_1(\mathbf{r}) \equiv \mathcal{V}(\mathbf{r}) - \mathcal{V}_0(\mathbf{r})$,with best results found when structural changes due to $\mathcal{V}_1$ are small. Using the $\mathcal{V}_0$ of Eq. (4.28) does not incorporate enough short ranged correlations for it to be a good starting point for our iterative process. This idea is indeed supported by results for the integrated charge using this $\mathcal{V}_0$, shown in Fig. 4.10(b). Due to the weak effective field of the colloid, counterions flooded into the region around the colloid surface, resulting in the peak value of integrated charge more than twice of the colloid charge! Although the result of this SCA indeed looks

ridiculous, we may still solve the LMF equation using this SCA as a starting point. For the iterative solution, we performed several LR iterations using configurations of the previous LR iteration. After LR has reached self-consistency, we used the $\mathcal{V}_R$ generated from the LR to do a new simulation, and with configurations from the new simulation we can do a LR again. Finally, we were able to reach the converged solution after nine iterations. Also shown in Fig. 4.10(b), the integrated charge of full LMF system is in good agreement with that of Ewald summation.

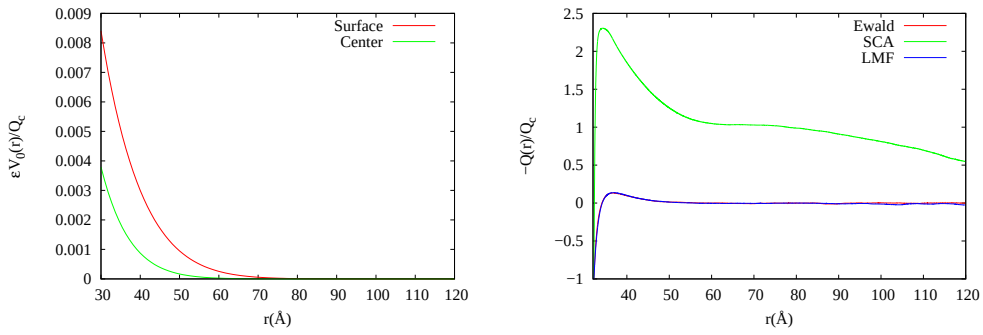

(a) (b)

Figure 4.10: (a) Comparison of $\mathcal{V}_0(\mathbf{r})$, scaled by Q_c/ϵ, for the case of an external charge smeared over the colloid surface ('surface', red) and placed at the center ('center', green). (b) The integrated charge for SCA (green) where $\mathcal{V}_0(\mathbf{r})$ is defined by Eq. (4.28), Ewald (red) and full LMF system (blue).

In this case, the iterative solution to the LMF equation still converges even though the SCA gives a very ridiculous initial guess of the structure. This is because our separation of Coulomb potential ($\sigma = 26.828$ Å) still satisfies those conditions that guarantee that LMF theory holds. Since overcharging is governed to a large extent by the correlations between counterions at the colloid surface, in SCA even if we did not incorporate the major correlations between the colloid and counterions, we have still captured the short-ranged correlations between ions. Therefore in

iterative solutions to the LMF equation, the correlations between the colloid and ions will be corrected gradually to reach convergence.

4.7 Summary and Conclusions

In this chapter, we have solved the LMF equation for the model system with charge inversion, using both simulations and linear response methods. The starting point of the iterative solution is the simulation with the strong-coupling approximation (SCA). In SCA, short-ranged correlations, the major factor that leads to overcharging, has been incorporated in the system, therefore SCA reproduces similar density profiles to the full system and gives overcharging around the colloid. However, by omitting long-ranged forces, SCA does not force the integrated charge $Q(r)$ to go back to zero as r increases. A self-consistent solution of the LMF equation will maintain neutrality and yield correct densities. Both simulations and the linear response method could iteratively solve the LMF equation effectively. The linear response method, which iterates using configurations only of the strong coupling system, can yield quick convergence without the need for further simulations, and is thus the method of choice in most cases. We have also looked at different ways of separating the Coulomb potential and the external potential of the colloid. Our simulations shows that as long as the potential separation obeys the conditions used in the derivation of the LMF equation, the LMF equation can be solved iteratively and yield the correct answer.

Chapter 5

LMF Treatment of Charge Inversion System: Solvation Free Energy

In this chapter, we will use simulations in the short-ranged mimic system only, to calculate the solvation free energy in the long-ranged full system. The model system is still the charge inversion system discussed in the last chapter.

5.1 Overview of The Solvation Free Energy Calculation Process

Since all the simulations were performed in NPT ensembles, the solvation free energy will be the Gibbs free energy difference between the system with the colloid solvated and the bulk. The solvation free energy in the full system is represented by the symbol ΔG_{sol}. The solvation free energy in the short-ranged mimic system, represented by the symbol $\Delta G_{R,sol}$, is defined as the free energy difference between the full LMF system that has already reached self-consistency and the bulk solution with only short-ranged pair interactions. Our goal is to obtain ΔG_{sol} by calculating $\Delta G_{R,sol}$ and adding a correction term ΔG_{LMF}, which comes from turning on the long-ranged part of Coulomb potential in pair interactions. The correction term ΔG_{LMF} can be obtained by either thermodynamic integration or approximations based on the LMF theory, as we shall discuss later.

The solvation free energy in the long-ranged full system ΔG_{sol} serves as the benchmark for our calculations in the mimic system. The procedure of ΔG_{sol} cal-

culation can be divided into two parts, as shown schematically in Fig. 5.1: First we will grow a neutral repulsive sphere with radius $R_c = 30$ Å in bulk salt solution, and this is the free energy change of inserting a hard sphere, ΔG_{HS}; then the sphere will be charged gradually from zero to $-110q$, and this part is the free energy of charging, ΔG_{charge}. Therefore $\Delta G_{sol} = \Delta G_{HS} + \Delta G_{\text{charge}}$.

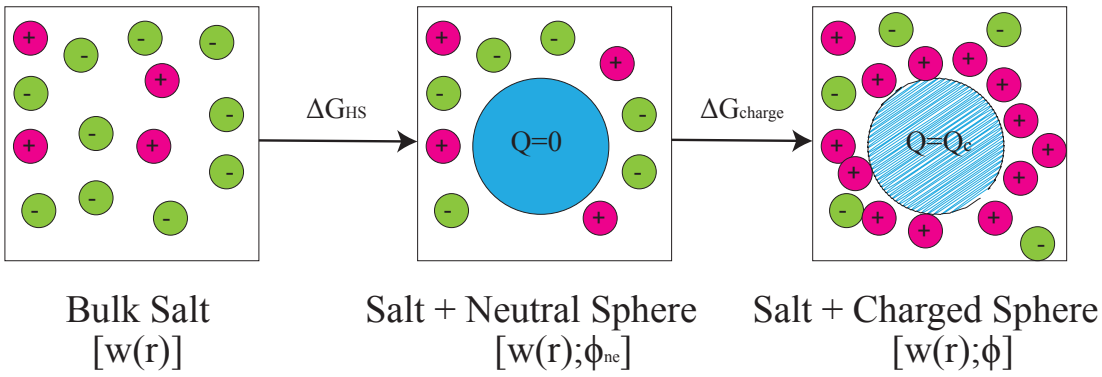

Figure 5.1: Illustration of the solvation free energy calculation process in the full system. The first box contains bulk salt with long-ranged pair interaction $w(r)$. The second box contains a neutral repulsive solute immersed in salt, and the external field ϕ_{ne} contains only non-electrostatic interactions. The third box contains a sphere with charge Q_c and salts, and the external field ϕ includes both non-electrostatic and electrostatic interactions.

The procedure of $\Delta G_{R,sol}$ calculation in the short-ranged system is similar to that of ΔG_{sol}, as shown schematically in Fig. 5.2. First we obtain the free energy of inserting a repulsive sphere: $\Delta G_{R,HS}$, then we charge the colloid gradually and obtain the free energy of charging: $\Delta G_{\text{R,charge}}$. At this stage we have reached the SCA system. Then the long-ranged part of the renormalized field, ϕ_{R1}, will be turned on such that the singlet density in the mimic system is the same as that in the full system. The free energy corresponding to ϕ_{R1} is $\Delta G_{\phi_{R1}}$. Therefore, $\Delta G_{R,sol} = \Delta G_{R,HS} + \Delta G_{\text{R,charge}} + \Delta G_{\phi_{R1}}$.

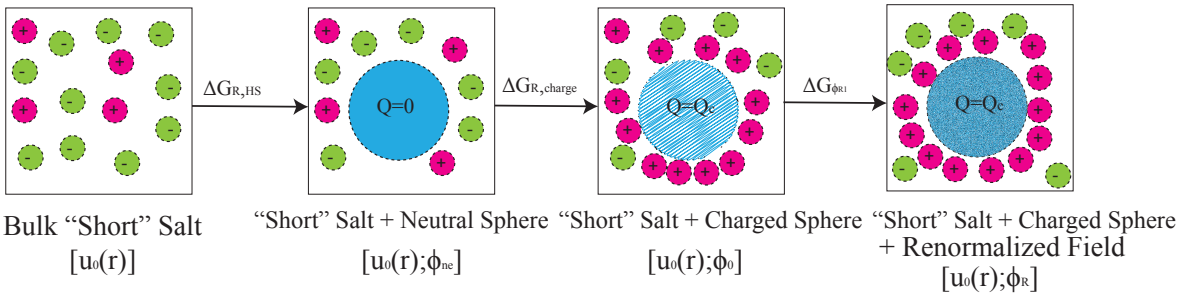

Figure 5.2: Illustration of the solvation free energy calculation process in the mimic system. The first box contains bulk salt with only short-ranged pair interaction $u_0(r)$. The second box contains a neutral repulsive solute immersed in salt, and the external field $\phi_{\rm ne}$ contains only non-electrostatic interactions. The third box contains a sphere with charge Q_c and salts, and the external field ϕ_0 includes both non-electrostatic interaction and only the short-ranged part of electrostatic interactions. The fourth box contains a sphere with charge Q_c and salts, and the renormalized external field $\phi_R = \phi_0 + \phi_{R1}$. Ions and the colloid are drawn in dashed lines to represent they are interacting only via the short-ranged part of the Coulomb potential.

In the next section we will derive the expression for ΔG_{LMF}, and then will proceed to the calculation of each component of the solvation free energy.

5.2 Derivation of ΔG_{LMF} Using LMF Theory

For convenience equations of solvation free energy are derived for grand canonical ensemble, but the results can be also applied to other ensembles. This section is based in part on results derived by Weeks[79].

We use the multi-component system described in Section 4.1 where both pair interactions and the external potential contain both electrostatic and non-electrostatic interactions. We will consider the free energy in the full system with external potential $\{\phi_i\}$ and the mimic system with renormalized external potential $\{\phi_{R,i}\}$, where $\{\phi_{R,i}\}$ is determined by the self-consistent LMF equation (4.7),

ensuring to a good approximation that both systems have the same singlet density

$$\rho_i(\mathbf{r};\{\phi_i\}) = \rho_{R,i}(\mathbf{r};\{\phi_{R,i}\}). \tag{5.1}$$

The total potential energy in the full system is

$$U_{\text{full}} = \sum_{i=1}^{M} \int d\mathbf{r}\rho_i(\mathbf{r})\phi_i(\mathbf{r}) + \frac{1}{2}\sum_{i=1}^{M}\sum_{j=1}^{M}\int d\mathbf{r}\int d\mathbf{r}'\rho_{ij}^{(2)}(\mathbf{r},\mathbf{r}')w_{ij}(|\mathbf{r}-\mathbf{r}'|), \tag{5.2}$$

while the total potential energy in the mimic system is

$$U_R = \sum_{i=1}^{M} \int d\mathbf{r}\rho_{R,i}(\mathbf{r})\phi_{R,i}(\mathbf{r}) + \frac{1}{2}\sum_{i=1}^{M}\sum_{j=1}^{M}\int d\mathbf{r}\int d\mathbf{r}'\rho_{R,ij}^{(2)}(\mathbf{r},\mathbf{r}')u_{0,ij}(|\mathbf{r}-\mathbf{r}'|), \tag{5.3}$$

The grand canonical free energy in the full and mimic systems, are presented by $\Omega[\{\phi_i\}]$ and $\Omega[\{\phi_{R,i}\}]$, respectively, both of which are functional of the external potential. To obtain the free energy difference between $\Omega[\{\phi_i\}]$ and $\Omega[\{\phi_{R,i}\}]$, we can construct an intermediate λ system described by a Hamiltonian

$$\mathcal{H}_\lambda = (1-\lambda)\mathcal{H}_R + \lambda\mathcal{H}_{\text{full}}\ (0 \le \lambda \le 1), \tag{5.4}$$

where $\mathcal{H}_R$ and $\mathcal{H}_{\text{full}}$ are the Hamiltonians for the mimic and the full system respectively. When $\lambda = 0$ it is the mimic system with total potential energy U_R, and $\lambda = 1$ represents the full system with total potential energy U_{full}. Then the relation between $\Omega[\{\phi_i\}]$and $\Omega[\{\phi_{R,i}\}]$ can be obtained exactly in principle by performing

the thermodynamic integration (TI)[36, 80]

$$\beta\Omega[\{\phi_i\}] = \beta\Omega[\{\phi_{R,i}\}] + \beta\sum_{i=1}^{M}\int d\mathbf{r}\rho_{R,i}(\mathbf{r})[\phi_i(\mathbf{r}) - \mu_i - \phi_{R,i}(\mathbf{r}) + \mu_{R,i}] + \frac{\beta}{2}\sum_{i=1}^{M}\sum_{j=1}^{M}\int_0^1 d\lambda\int d\mathbf{r}\int d\mathbf{r}'\rho^{(2)}_{\lambda,ij}(\mathbf{r},\mathbf{r}')u_{1,ij}(|\mathbf{r}-\mathbf{r}'|), \tag{5.5}$$

where

$$\phi_i(\mathbf{r}) = q_i\mathcal{V}(\mathbf{r}) + \phi_{\mathrm{ne},i}(\mathbf{r}), \tag{5.6}$$

$$\phi_{R,i}(\mathbf{r}) = q_i\mathcal{V}_R(\mathbf{r}) + \phi_{\mathrm{ne},i}(\mathbf{r}), \tag{5.7}$$

$$u_{1,ij}(|\mathbf{r}-\mathbf{r}'|) = \frac{q_iq_j}{\epsilon}v_1(|\mathbf{r}-\mathbf{r}'|) = \frac{q_iq_j}{\epsilon}\frac{\mathrm{erf}(\frac{|\mathbf{r}-\mathbf{r}'|}{\sigma})}{|\mathbf{r}-\mathbf{r}'|}, \tag{5.8}$$

$\rho^{(2)}_{\lambda,ij}$ is the pair correlation function for the ith and jth species in the system with Hamiltonian $\mathcal{H}_\lambda$, and μ_i and $\mu_{R,i}$ are chemical potentials of the ith species in the full and mimic system, respectively. Similarly, the free energy difference between the full and the mimic system in the bulk can be written as

$$\beta\Omega[\{\phi_i\}=0] = \beta\Omega[\{\phi_{R,i}\}=0] + \beta\sum_{i=1}^{M}\int d\mathbf{r}\rho_{B,i}[\mu_{R,i} - \mu_i] + \frac{\beta}{2}\sum_{i=1}^{M}\sum_{j=1}^{M}\int_0^1 d\lambda\int d\mathbf{r}\int d\mathbf{r}'\rho^{(2)}_{\lambda,ij}(|\mathbf{r}-\mathbf{r}'|;\{\phi_{\lambda,i}\}=0)u_{1,ij}(|\mathbf{r}-\mathbf{r}'|), \tag{5.9}$$

where $\rho_{B,i}$ is the bulk density of the ith species. Note that in the bulk $\rho^{(2)}_{\lambda,ij}(|\mathbf{r}-\mathbf{r}'|)$ will be a function only of $|\mathbf{r}-\mathbf{r}'|$. Subtracting Eq. (5.5) by Eq. (5.9) gives the

difference in solvation free energy between the full and mimic system

$$\beta\Omega_{sol}[\{\phi^i\}] = \beta\Omega_{R,sol}[\{\phi^i_R\}] + \beta\int d\mathbf{r}\rho^q_R(\mathbf{r})[\mathcal{V}(r) - \mathcal{V}_R(r)] + \beta\sum_{i=1}^{M}\int d\mathbf{r}[\rho_{R,i}(\mathbf{r}) - \rho_{B,i}][\mu_{R,i} - \mu_i]$$
$$+ \frac{\beta}{2}\sum_{i=1}^{M}\sum_{j=1}^{M}\int_0^1 d\lambda\int d\mathbf{r}\int d\mathbf{r}'[\rho^{(2)}_{\lambda,ij}(\mathbf{r},\mathbf{r}') - \rho^{(2)}_{\lambda,ij}(|\mathbf{r}-\mathbf{r}'|;\{\phi_{R,i}=0\})]u_{1,ij}(|\mathbf{r}-\mathbf{r}'|), \tag{5.10}$$

It is useful to rewrite Eq. (5.10) in terms of the intrinsic free energy W, a functional of the densities $\{\rho_i\}$ and related to Ω by a Legendre transformation[81]

$$W[\{\rho_i\}] = \Omega[\{\phi_i\}] - \sum_{i=1}^{M}\int d\mathbf{r}\rho_i(\mathbf{r})[\phi_i(\mathbf{r}) - \mu_i], \tag{5.11}$$

so that

$$W_{sol}[\{\rho_i\}] = \Omega_{sol}[\{\phi_i\}] - \sum_{i=1}^{M}\int d\mathbf{r}\rho_i(\mathbf{r})\phi_i(\mathbf{r}) + \sum_{i=1}^{M}\mu_i\int d\mathbf{r}[\rho_i(\mathbf{r}) - \rho_{B,i}], \tag{5.12}$$

$$W_{R,sol}[\{\rho_{R,i}\}] = \Omega_{R,sol}[\{\phi_{R,i}\}] - \sum_{i=1}^{M}\int d\mathbf{r}\rho_{R,i}(\mathbf{r})\phi_{R,i}(\mathbf{r}) + \sum_{i=1}^{M}\mu_{R,i}\int d\mathbf{r}[\rho_{R,i}(\mathbf{r}) - \rho_{B,i}]. \tag{5.13}$$

Combining Eq. (5.12), (5.13) and (5.10) yields

$$\beta W_{sol}[\{\rho_i\}] - \beta W_{R,sol}[\{\rho_{R,i}\}]$$
$$= \frac{\beta}{2}\sum_{i=1}^{M}\sum_{j=1}^{M}\int_0^1 d\lambda\int d\mathbf{r}\int d\mathbf{r}'[\rho^{(2)}_{\lambda,ij}(\mathbf{r},\mathbf{r}') - \rho^{(2)}_{\lambda,ij}(|\mathbf{r}-\mathbf{r}'|;\{\phi_{R,i}\}=0)]u_{1,ij}(|\mathbf{r}-\mathbf{r}'|) \tag{5.14}$$

The useful feature of Eq. (5.14) is that we can take a functional derivative of

W with respect to $\rho_i(\mathbf{r})$ using

$$\frac{\delta\beta W[\{\rho_i\}]}{\delta\rho_i(\mathbf{r})} = \beta\mu_i - \beta\phi_i(\mathbf{r}), \tag{5.15}$$

and get a formally exact expression for the conjugate field. This gives

$$\begin{aligned}\beta\mu_i - \beta\phi_i(\mathbf{r}) = \beta\mu_{R,i} - \beta\phi_{R,i}(\mathbf{r}) \\ + \frac{\delta}{\delta\rho_{R,i}(\mathbf{r})}\{\beta\sum_{j\neq i}^{M}\int_0^1 d\lambda\int d\mathbf{r}\int d\mathbf{r}'[\rho^{(2)}_{\lambda,ij}(\mathbf{r},\mathbf{r}') - \rho^{(2)}_{\lambda,ij}(|\mathbf{r}-\mathbf{r}'|;\{\phi_{R,i}\}=0)]u_{1,ij}(|\mathbf{r}-\mathbf{r}'|) \\ + \frac{\beta}{2}\int_0^1 d\lambda\int d\mathbf{r}\int d\mathbf{r}'[\rho^{(2)}_{\lambda,ii}(\mathbf{r},\mathbf{r}') - \rho^{(2)}_{\lambda,ii}(|\mathbf{r}-\mathbf{r}'|;\{\phi_{R,i}\}=0)]u_{1,ii}(|\mathbf{r}-\mathbf{r}'|)\},\end{aligned} \tag{5.16}$$

which is equivalent to

$$\begin{aligned}\beta\phi_{R,i}(\mathbf{r}) = \beta\phi_i(\mathbf{r}) \\ + \frac{\delta}{\delta\rho_{R,i}(\mathbf{r})}\{\beta\sum_{j\neq i}^{M}\int_0^1 d\lambda\int d\mathbf{r}\int d\mathbf{r}'[\rho^{(2)}_{\lambda,ij}(\mathbf{r},\mathbf{r}') - \rho^{(2)}_{\lambda,ij}(|\mathbf{r}-\mathbf{r}'|;\{\phi_{R,i}\}=0)]u_{1,ij}(|\mathbf{r}-\mathbf{r}'|) \\ + \frac{\beta}{2}\int_0^1 d\lambda\int d\mathbf{r}\int d\mathbf{r}'[\rho^{(2)}_{\lambda,ii}(\mathbf{r},\mathbf{r}') - \rho^{(2)}_{\lambda,ii}(|\mathbf{r}-\mathbf{r}'|;\{\phi_{R,i}\}=0)]u_{1,ii}(|\mathbf{r}-\mathbf{r}'|) \\ + \int d\mathbf{r}[\rho_{R,i}(\mathbf{r}) - \rho_{B,i}][\beta\mu_{R,i} - \beta\mu_i]\}.\end{aligned} \tag{5.17}$$

Up to this point the expression in Eq. (5.17) provides a complicated but exact relation between $\phi_i(\mathbf{r})$ and $\phi_{R,i}(\mathbf{r})$. Now we will introduce the LMF theory to make approximations to the second term on the right hand side of Eq. (5.17).

The LMF equation, derived independently of Eq. (5.17) by integrating the balance of forces as given by the YBG hierarchy, also relates the conjugate field as

$$\beta\phi_{R,i}(\mathbf{r}) = \beta\phi_i(\mathbf{r}) + \beta\sum_{j=1}^{M}\int d\mathbf{r}'\rho_{R,j}(\mathbf{r}')u_{1,ij}(|\mathbf{r}-\mathbf{r}'|), \tag{5.18}$$

which can be rewritten as

$$\beta\phi_{R,i}(\mathbf{r}) = \beta\phi_i(\mathbf{r}) + \frac{\delta}{\delta\rho_{R,i}(\mathbf{r})}\{\beta\sum_{j\neq i}^{M}\int d\mathbf{r}\int d\mathbf{r}'[\rho_{R,j}(\mathbf{r}')-\rho_{B,j}][\rho_{R,i}(\mathbf{r})-\rho_{B,i}]u_{1,ij}(|\mathbf{r}-\mathbf{r}'|)$$
$$+\frac{\beta}{2}\int d\mathbf{r}\int d\mathbf{r}'[\rho_{R,i}(\mathbf{r}')-\rho_{B,i}][\rho_{R,i}(\mathbf{r})-\rho_{B,i}]u_{1,ii}(|\mathbf{r}-\mathbf{r}'|)\}. \quad (5.19)$$

Subtracting Eq. (5.19) from Eq. (5.17) we can formally integrate the right hand side and get to a good approximation if the LMF equation is accurate

$$\begin{aligned}
&\beta\sum_{j\neq i}^{M}\int_0^1 d\lambda\int d\mathbf{r}\int d\mathbf{r}'[\rho^{(2)}_{\lambda,ij}(\mathbf{r},\mathbf{r}')-\rho^{(2)}_{\lambda,ij}(|\mathbf{r}-\mathbf{r}'|;\{\phi_{R,i}\}=0)]u_{1,ij}(|\mathbf{r}-\mathbf{r}'|)\\
&+\frac{\beta}{2}\int_0^1 d\lambda\int d\mathbf{r}\int d\mathbf{r}'[\rho^{(2)}_{\lambda,ii}(\mathbf{r},\mathbf{r}')-\rho^{(2)}_{\lambda,ii}(|\mathbf{r}-\mathbf{r}'|;\{\phi_{R,i}\}=0)]u_{1,ii}(|\mathbf{r}-\mathbf{r}'|)\\
=&-\int d\mathbf{r}[\rho_{R,i}(\mathbf{r})-\rho_{B,i}][\beta\mu_{R,i}-\beta\mu_i]\\
&+\beta\sum_{j\neq i}^{M}\int d\mathbf{r}\int d\mathbf{r}'[\rho_{R,j}(\mathbf{r}')-\rho_{B,j}][\rho_{R,i}(\mathbf{r})-\rho_{B,i}]u_{1,ij}(|\mathbf{r}-\mathbf{r}'|)\\
&+\frac{\beta}{2}\int d\mathbf{r}\int d\mathbf{r}'[\rho_{R,i}(\mathbf{r}')-\rho_{B,i}][\rho_{R,i}(\mathbf{r})-\rho_{B,i}]u_{1,ii}(|\mathbf{r}-\mathbf{r}'|). \quad (5.20)
\end{aligned}$$

We can do similar treatment for all M components and this will give M equations in the form of Eq. (5.20). Then we can transform back to the grand canonical ensemble (Eq. (5.10)) and get a simplified expression for the solvation free energy

$$\beta\Omega_{sol}[\{\phi^i\}] = \beta\Omega_{R,sol}[\{\phi^i_R\}] + \beta\int d\mathbf{r}\rho^q_R(\mathbf{r})[\mathcal{V}(r)-\mathcal{V}_R(r)] + \beta\sum_{i=1}^{M}\int d\mathbf{r}[\rho_{R,i}(\mathbf{r})-\rho_{B,i}][\mu_{R,i}-\mu_i]$$
$$+\sum_{i=1}^{M}\{-\int d\mathbf{r}[\rho_{R,i}(\mathbf{r})-\rho_{B,i}][\beta\mu_{R,i}-\beta\mu_i]\}$$
$$+\frac{\beta}{2}\sum_{i=1}^{M}\sum_{j=1}^{M}\int d\mathbf{r}\int d\mathbf{r}'\rho_{R,i}(\mathbf{r})\rho_{R,j}(\mathbf{r}')u_{1,ij}(|\mathbf{r}-\mathbf{r}'|). \quad (5.21)$$

We see that the chemical potential terms cancel exactly. This means that we do not have to know the exact value of chemical potential when we are computing the solvation free energy difference between the full and mimic systems. Using the LMF equation (5.18) and noting that $\phi_{R,i}(\mathbf{r})-\phi_i(\mathbf{r}) = q_i[\mathcal{V}_R(\mathbf{r})-\mathcal{V}(\mathbf{r})]$, Eq. (5.21) can

finally be written in the very simple form

$$\begin{aligned}\beta\Omega_{sol}[\{\phi^i\}] &= \beta\Omega_{R,sol}[\{\phi^i_R\}] + \beta\int d\mathbf{r}\rho^q_R(\mathbf{r})[\mathcal{V}(r) - \mathcal{V}_R(r)] \\ &+ \frac{\beta}{2}\sum_{i=1}^{M}\int d\mathbf{r}\rho_{R,i}(\mathbf{r})[\phi_{R,i}(\mathbf{r}) - \phi_i(\mathbf{r})] \\ &= \beta\Omega_{R,sol}[\{\phi^i_R\}] - \frac{\beta}{2}\int d\mathbf{r}\rho^q_R(\mathbf{r})[\mathcal{V}_R(\mathbf{r}) - \mathcal{V}(\mathbf{r})]. \end{aligned} \tag{5.22}$$

This is the final result we are using to calculate the solvation free energy difference between the full system and the mimic system. For the NPT ensemble, Eq. (5.22) becomes

$$\beta\Delta G_{LMF} \equiv \Delta G_{sol} - \Delta G_{R,sol} = -\frac{\beta}{2}\int d\mathbf{r}\rho^q_R(\mathbf{r})[\mathcal{V}_R(\mathbf{r}) - \mathcal{V}(\mathbf{r})]. \tag{5.23}$$

5.3 Calculating the Solvation Free Energy in Practice

All of our simulations in both full and mimic systems are performed in NPT ensembles. For the full systems, the pressure is 7.37 atm and the pressure in the mimic systems is 7.59 atm. Such choice of pressure will ensure that in the bulk the concentration of +3 counterion will be equal to 0.106 M. For simulations in the mimic systems, we choose $\sigma = 26.828$ Å for the Coulomb potential split.

5.3.1 The Free Energy of Inserting a Repulsive Sphere: ΔG_{HS} and $\Delta G_{R,HS}$

For the solvation free energy of growing a neutral sphere, the Bennett Acceptance Ratio (BAR) method was used[36, 82]. The BAR is an algorithm for estimating the free energy difference between two states using configurations from

both states. For state 0 with energy U_0 and state 1 with energy U_1, in the canonical ensemble the Helmholtz free energy difference between state 1 and state 0 can be written as

$$\exp(\beta\Delta F) = \frac{Q_0}{Q_1} = \frac{\langle w \exp(-\beta U_0)\rangle_1}{\langle w \exp(-\beta U_1)\rangle_0}, \tag{5.24}$$

where w is an arbitrary function. In BAR, the function w is chosen in a way that minimizes the variance of ΔF. Then the ΔF is given by

$$\exp(\beta\Delta F) = \frac{Q_0}{Q_1} = \frac{\langle f(U_0 - U_1 + C)\rangle_1}{\langle f(U_1 - U_0 - C)\rangle_0} \exp(\beta C), \tag{5.25}$$

where f is the Fermi-Dirac function $f(x) = 1/(1 + \exp(\beta x))$ and the optimal choice for C is

$$C = \ln(\frac{Q_0}{Q_1}) = \Delta F. \tag{5.26}$$

Then Eq. (5.25) and (5.26) are solved iteratively for convergence of C and ΔF. Those equations above are derived in canonical ensembles, but the basic principle can be applied to our systems with NPT ensembles as well.

For our calculation of ΔG_{HS} and $\Delta G_{R,HS}$, we grew a neutral repulsive sphere from radius 0 to the radius 30 Å with an increment 0.5 Å. For simulations of each increment, 20000 configurations were saved.

Our calculation gives $\Delta G_{HS} = 28.01\ k_BT$ and $\Delta G_{R,HS} = 28.07\ k_BT$, i.e. $\Delta G_{HS} \simeq \Delta G_{R,HS}$. This is not very surprising because in the bulk, the full system and the short-ranged system have almost the same structure, due to cancellation of long-ranged forces. Therefore when a repulsive hard sphere is inserted into the bulk salt, the change of structure and energy only arises from the hard core repulsion between the hard sphere and ions with the same hard sphere diameter while elec-

trostatic correlations in the two system are still identical to each other. As a result the free energy change due to insertion of a hard sphere should be the same in both the full and short-ranged systems.

5.3.2 Solvation Free Energy of Charging

The conventional way of calculating the solvation free energy of charging is the thermodynamic integration (TI)[36, 83]. In the full system with the long-ranged Coulomb potential, this starts with the total energy of the system, which depends on the charge of the colloid Q

$$U(Q) = U_{\text{pair}} + \sum_{i=1}^{M} \sum_{n=1}^{N_i} \frac{Q q_i}{\epsilon r_{i,n}}, \tag{5.27}$$

where U_{pair} is the pair interaction term and N_i is the number of particles for the ith species. Then the free energy of charging the colloid from $Q = 0$ to $Q = Q_c$ can be calculated by TI

$$\Delta G_{\text{charge}} = G(Q = Q_c) - G(Q = 0) = \int_0^{Q_c} dQ \langle \frac{\partial U}{\partial Q} \rangle_Q. \tag{5.28}$$

Eq. (5.28) can be written in discretized form if we perform the charging process from 0 to Q_c in K steps with a charge increment $\Delta Q \equiv Q_c/K$

$$\Delta G_{\text{charge}} \simeq \sum_{l=1}^{K} \langle \sum_{i=1}^{M} \sum_{n=1}^{N_i} \frac{\Delta Q q_i}{\epsilon r_{i,n}} \rangle_{Q=l\Delta Q}. \tag{5.29}$$

However, special treatment of electrostatic interactions during the charging process is required if Ewald sums are to be used. Ewald sums requires neutrality so as to perform lattice sums, whereas for NPT or NVT ensemble the system is not neutral while charging the colloid. A commonly used method to handle this problem is to place a uniform charge background in the system for each step that

will neutralize the increment in the solute charge. Correspondingly, a self-interaction term will be added to the total of electrostatic energy[83, 84]. For example, if we charge the solute from Q_0 to Q_1, the change in electrostatic energy ΔU calculated by this method will be

$$\Delta U = (Q_1 - Q_0)\phi_{\mathrm{EW}} + \frac{1}{2\epsilon L}\xi(Q_1^2 - Q_0^2), \tag{5.30}$$

where ϕ_{EW} is the electrostatic potential from Ewald sums, and L is the length of the cubic simulation box and $\xi = -2.837297$. The second term on the right hand side of Eq. (5.30) gives the correction from the neutralizing background. With this neutralizing charge background, we may make ΔQ arbitrarily small so as to ensure the accuracy of TI. TI with this neutralizing background is very useful in the solvation free energy calculation of a solute in dielectrics (usually water), where the free energy change corresponding to a small change in the solute charge can be very large. This method has been successfully applied to various free energy calculations, such as ion solvation energy in water[83, 85, 86].

Another way of maintaining neutrality during the charging process is to use a grand canonical (μVT) ensemble. Particles can be added or removed during the charging process. However, if we want to perform TI in the grand canonical ensemble, the increment ΔQ can only be an integer multiple of the minimum ion charge and sometimes the accuracy of TI might not be guaranteed.

In our calculation of free energy of charging in the full system, simulations are performed in the NPT ensemble. We charge the colloid from 0 to $-110q$ with the increment $\Delta Q = -1q$. However, during the charging process, we did not add

a neutralizing background to the system. This is because the colloid is strongly charged with $Q_c = -110q$ and we do not know whether the structure of system would be disturbed by this huge neutralizing charge background. Instead, our approach is like doing the charging process in a "quasi"grand canonical ensemble. In general, for each step we keep the system neutral by removing a -1 anion when the charge of the colloid has increased by $-1q$. In other words, the total number of ions is not constant during the whole charging process.

For any step of our charging process, the charge of the colloid is completely screened after r goes beyond a certain radius, say, R_{cut}. Since we have chosen the pressure of the system to be that of the bulk, the region outside the sphere of radius R_{cut} is essentially bulk-like, while the region inside the sphere can be viewed as a grand canonical ensemble interacting with a particle reservoir outside. Since the free energy of charging only depends on the structure inside the sphere, for the calculation of colloid-ion interaction energy change ΔU of each step

$$\Delta U = \sum_{i=1}^{M} \sum_{n=1}^{N_i} \frac{\Delta Q q_i}{\epsilon r_{i,n}}, \tag{5.31}$$

we may only consider ions inside the sphere of radius R_{cut}. In our case $R_{\text{cut}} = 110$ Å, which is large enough to ensure that the region outside the sphere is bulk-like. Then the change of charging free energy from Q_0 to $Q_1 = Q_0 + \Delta Q$ can be calculated via the free energy perturbation (FEP)[77, 87]

$$\begin{aligned} \beta \Delta G_{\text{charge}}(Q_0 \to Q_1) &= -\ln \langle e^{-\beta \Delta U} \rangle_{Q_0} \\ &= \ln \langle e^{\beta \Delta U} \rangle_{Q_1}. \end{aligned} \tag{5.32}$$

Furthermore, as we will show later, the probability distribution of ΔU is can be

well approximated by a Gaussian distribution, so that the ensemble averages in Eq. (5.32) can be further written as

$$\begin{aligned}\beta\Delta G_{\text{charge}}(Q_0 \to Q_1) &= \beta\langle\Delta U\rangle_{Q_0} - \frac{\beta^2}{2}\langle(\delta\Delta U)^2\rangle_{Q_0} \\ &= \beta\langle\Delta U\rangle_{Q_1} + \frac{\beta^2}{2}\langle(\delta\Delta U)^2\rangle_{Q_1},\end{aligned} \tag{5.33}$$

where $\delta\Delta U = U - \langle U\rangle$. In our calculations, we are using both of the equivalent forms in Eq. (5.33) to calculate the free energy of charging and then take the average of them, i.e.

$$\beta\Delta G_{\text{charge}}(Q_0 \to Q_1) = \frac{1}{2}\beta[\langle\Delta U\rangle_{Q_0} + \langle\Delta U\rangle_{Q_1}] + \frac{1}{4}\beta^2[\langle(\delta\Delta U)^2\rangle_{Q_1} - \langle(\delta\Delta U)^2\rangle_{Q_0}]. \tag{5.34}$$

Then the total energy of charging is just the sum of a series of $\Delta G_{\text{charge}}(Q_0 \to Q_1)$

$$\Delta G_{\text{charge}} = \sum_{Q=0}^{-109} \Delta G_{\text{charge}}(Q \to Q-1). \tag{5.35}$$

Therefore the free energy of charging in the long-ranged full system can be calculated by FEP with Gaussian approximation directly, without doing thermodynamic integrations.

For the charging process in the short-ranged system, in which the simulations are in the SCA regime, although the charge of the colloid is not completely screened due to neglect of long-ranged interactions, as described in Section 4.5, the charge density has reached zero after a certain distance away from the colloid and this enables us to calculate the ΔU for each configuration by only counting particles inside a sphere of radius $R_{\text{cut}} = 110$ Å as well. Therefore the free energy of charging can be also calculated using the method for the full system, except that ΔU is

defined as

$$\Delta U = \sum_{i=1}^{M} \sum_{n=1}^{N_i} \frac{\Delta Q q_i}{\epsilon} \cdot \frac{\mathrm{erfc}(\frac{r_{i,n}}{\sigma})}{r_{i,n}}. \tag{5.36}$$

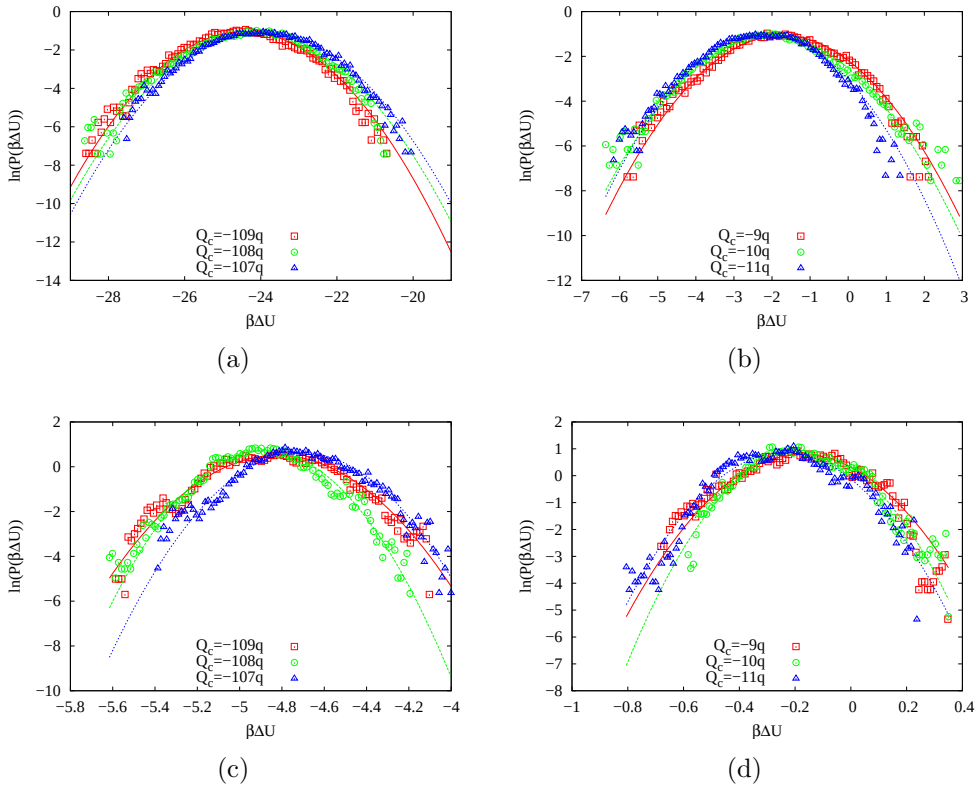

Figure 5.3: (a) Probability distribution of ΔU for full system with $Q_c = -109q$ (red square), $-108q$ (green circle) and $-107q$ (blue triangle), respectively. (b) Probability distribution of ΔU for full system with $Q_c = -9q$ (red square), $-10q$ (green circle) and $-11q$ (blue triangle), respectively. (c) Probability distribution of ΔU for short-ranged system with $Q_c = -109q$ (red square), $-108q$ (green circle) and $-107q$ (blue triangle), respectively. (d) Probability distribution of ΔU for short-ranged system with $Q_c = -9q$ (red square), $-10q$ (green circle) and $-11q$ (blue triangle), respectively. For all figures, lines are drawn by fitting points to a parabola function.

In Fig. 5.3, we have shown the probability distribution of $\beta\Delta U$ for charged systems with $Q_c = -9q, -10q, -11q, -107q, -108q$ and $-109q$ in the full system (Fig. 5.3(a) and 5.3(b)) and short-ranged mimic system (Fig. 5.3(c) and 5.3(d)). We can see that for our selected charged states, either in the full or the short-ranged

mimic system, the probability distribution of their ΔU can be well approximated by the Gaussian distribution. This indeed shows that the Gaussian approximation in Eq. (5.33) is a reasonable approximation to the charging free energy. We have also used the formula of FEP in Eq. (5.32) to calculate the solvation free eneryg of charging and this gives almost identical results to that obtained with the Gaussian approximation.

Therefore, using Eq. (5.33) and (5.35) we have calculated the free energy of charging in the full system and short-ranged mimic system respectively. In the full system $\Delta G_{\text{charge}} = -1322.16\ k_BT$ and in the mimic system $\Delta G_{\text{R,charge}} = -239.52\ k_BT$. Apparently, neglecting long-ranged interactions makes the magnitude of charging free energy in the mimic system much smaller than that in the full system.

5.3.3 $\Delta G_{\phi_{R1}}$, ΔG_{LMF} and $\Delta G_{R,sol}$

As shown in Section 4.6.2, for the mimic system with $\sigma = 26.828$ Å, we could do two linear response iterations to make the LMF equation converge to self-consistency. Moreover, in Fig. 4.8(a) we have shown that the probability distribution of Φ_{R1} in both the SCA system and the mimic system with ϕ_{R1} are Gaussian and there is good overlap between the two Gaussian distributions. Therefore we may use the Gaussian approximation in Eq. (5.33) again to calculate the contribution to the solvation free energy from ϕ_{R1}, i.e.

$$\beta\Delta G_{\phi_{R1}} = \frac{\beta}{2}[\langle\Phi_{R1}\rangle_{\phi_0} + \langle\Phi_{R1}\rangle_{\phi_{R1}}] + \frac{\beta^2}{4}[\langle(\delta\Phi_{R1})^2\rangle_{\phi_{R1}} - \langle(\delta\Phi_{R1})^2\rangle_{\phi_0}], \qquad (5.37)$$

where $\delta\Phi_{R1} \equiv \Phi_{R1} - \langle\Phi_{R1}\rangle$. With this Gaussian approximation, we obtained the contribution to solvation free energy from $\mathcal{V}_{R1}$: $\Delta G_{\phi_{R1}} = -32.49\ k_BT$.

Then the correction term from turning on the long-ranged part of the Coulomb potential is obtained by the direct integration

$$\beta\Delta G_{LMF} = -\frac{\beta}{2}\int d\mathbf{r}\rho_R^q(\mathbf{r})[\mathcal{V}_R(\mathbf{r}) - \mathcal{V}(\mathbf{r})], \tag{5.38}$$

and this gives $\Delta G_{LMF} = -1048.65\ k_BT$.

Now we can list all the components of $\Delta G_{R,sol}$ together with ΔG_{LMF} in Table 5.1.

$\beta\Delta G_{R,HS}$	$\beta\Delta G_{\mathrm{R,charge}}$	$\beta\Delta G_{\phi_{R1}}$	$\beta\Delta G_{R,sol}$	$\beta\Delta G_{LMF}$	$\beta[\Delta G_{R,sol} + \Delta G_{LMF}]$
28.07	-239.52	-32.49	-243.94	-1048.65	-1292.59

Table 5.1: Components of $\Delta G_{R,sol}$ together with ΔG_{LMF}, in unit of k_BT.

We may also list components of solvation free energy in the full system ΔG_{sol} in Table 5.2

$\beta\Delta G_{HS}$	$\beta\Delta G_{\mathrm{charge}}$	$\beta\Delta G_{sol}$
28.01	-1322.16	-1294.15

Table 5.2: Components of ΔG_{sol} in the full system, in unit of k_BT.

We can see that the value of $\beta[\Delta G_{R,sol} + \Delta G_{LMF}]$ is very close to that of $\beta\Delta G_{sol}$, which indicates that our approach of solvation free energy calculation in the short-ranged mimic system indeed obtains very good estimate of the solvation free energy in the full system. In our calculation in the short-ranged systems, the major contribution to the solvation free energy comes from ΔG_{LMF}, the free energy change from turning on long-ranged part of the Coulomb potential, while the free energy of turning on only short-ranged part of the Coulomb potential, $\Delta G_{\mathrm{R,charge}}$,

only contributes less than a quarter of the total solvation free energy, even though by turning on the short-ranged interactions we can obtain most features of the fluid structure, as described in Section 4.5.

Compared with calculating the solvation free energy directly in the full system using the Ewald summation, the advantage of solvation free energy calculations in the short-ranged system is in its charging process. For each step in the charging process in the full system, a simulation with Ewald summation is required. The CPU time scales as $\mathcal{O}(N^2)$ for standard Ewald summation, or $\mathcal{O}(N \ln N)$ for particle-mesh Ewald[36], which does not scale well in massively parallel simulations[88]. However, for the charging process in the short-ranged system, the CPU time only scales linearly with N, thus saving lots of computational resources.

5.4 The Charging Free Energy's Quadratic Dependence on the Colloid Charge

As a byproduct of the charging free energy calculation, in the full system we can calculate the free energy of charging the colloid from 0 to an arbitrary integer charge Q between 0 and $Q_c = -110q$, and thus to look at the ΔG_{charge} as a function of Q. We have plotted ΔG_{charge} as a function of Q in Fig. 5.4(a). We tried to fit $\Delta G_{\text{charge}}(Q)$ to a quadratic function using the method of least squares, which gives $\Delta G_{\text{charge}}(Q) = -0.1132Q^2$ (blue line). It seems that the quadratic function gives a good description of ΔG_{charge}'s dependence on Q. We have also calculated the error of the fitting function, shown in Fig. 5.4(b). The magnitude of the error

does not increase monotonically as Q increases or look very large compared with the magnitude of ΔG_{charge}.

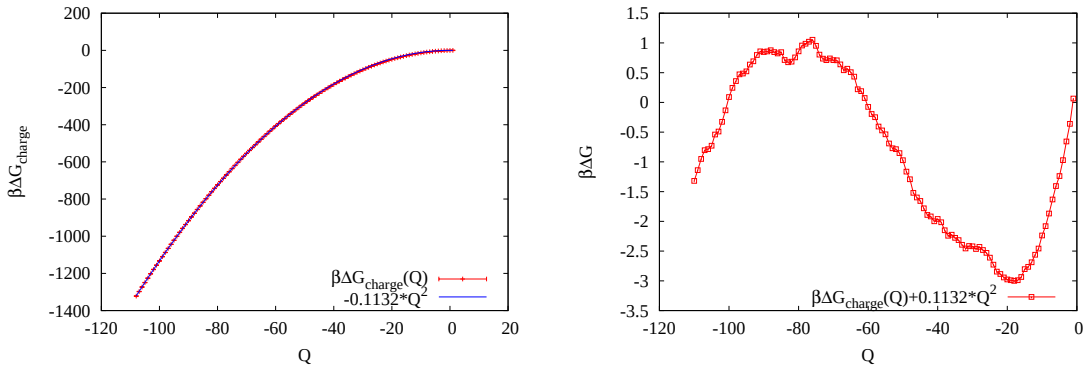

(a) (b)

Figure 5.4: (a) The free energy of charging ΔG_{charge} in the full system as a function of the colloid charge Q (red), with error bars given, and the quadratic fit of $\Delta G_{\text{charge}}(Q)$ (blue). (b) The error of the quadratic fit.

The quadratic dependence of ΔG_{charge} on Q looks interesting, and perhaps surprising. When Q is small, since the correlation between the colloid and ions is not strong, the charge density and electrostatic potential can be approximated by the Debye-Hückel theory. Then one could perform a Debye charging process[44, 75] and this indeed gives a charging free energy that has quadratic dependence on Q. However, as Q increases, the Debye-Hückel theory breaks down and we do not know whether the free energy of charging would still have a quadratic dependence on Q.

We also looked at the dependence on Q for components of $\Delta G_{\text{R,sol}}$, i.e. $\Delta G_{\text{R,charge}}$, $\Delta G_{\phi_{R1}}$ and ΔG_{LMF}. To obtain a complete set of $\Delta G_{\phi_{R1}}$ and ΔG_{LMF}, for each Q, we started from the SCA and performed two linear response iterations to ensure convergence, then the corresponding $\Delta G_{\phi_{R1}}$ and ΔG_{LMF} are calculated.

A quadratic fit and its errors for $\Delta G_{LMF}(Q)$, $\Delta G_{\phi_{R1}}(Q)$ and $\Delta G_{\text{R,charge}}(Q)$

are given in Fig. 5.5, 5.6 and 5.7, respectively. All of them can be fit by quadratic functions of Q, while for $\Delta G_{\phi_{R1}}(Q)$, the error of fitting is large compared to the magnitude of the free energy. Moreover, for $\Delta G_{\mathrm{R,charge}}(Q)$, the error of fitting grows as the magnitude of Q increases.

The quadratic dependence on Q in $\Delta G_{\phi_{R1}}$ and ΔG_{LMF} is what we expected to see. This is because

$$\begin{aligned}\beta\Delta G_{LMF} &= -\frac{\beta}{2}\int d\mathbf{r}\rho_R^q(\mathbf{r})[\mathcal{V}_R(\mathbf{r})-\mathcal{V}(\mathbf{r})] \\ &= -\frac{\beta}{2}\int d\mathbf{r}\rho_R^q(\mathbf{r})[\frac{1}{\epsilon}\int d\mathbf{r}'\rho_R^q(\mathbf{r}')v_1(|\mathbf{r}-\mathbf{r}'|)],\end{aligned} \tag{5.39}$$

and it has been shown previously[28] that the profile of $\mathcal{V}_R(\mathbf{r})-\mathcal{V}(\mathbf{r})$ is dominated by the long-ranged part of $\rho_R^q(\mathbf{r})$, and we may even replace the $\rho_R^q(\mathbf{r})$ in Eq. (5.39) with a Debye charge density in the form of Eq. (4.12) that satisfies the Stillinger-Lovett zeroth and second moment conditions[76] to get a very good estimate of $\mathcal{V}_R(\mathbf{r})-\mathcal{V}(\mathbf{r})$. Therefore ΔG_{LMF} should have quadratic dependence on the charge of the colloid Q. Similar arguments should also hold for $\Delta G_{\phi_{R1}}$. As we showed in Table 5.1, since the major contribution to the free energy of charging comes from ΔG_{LMF}, which has quadratic dependence on Q, then it is not so surprising that $\Delta G_{\mathrm{charge}}$ of the full system has to a good approximation quadratic dependence on Q as well.

5.5 Summary and Conclusions

In this chapter, we used simulations in the short-ranged mimic system, combined with LMF theory, to calculate the solvation free energy of the colloid in the

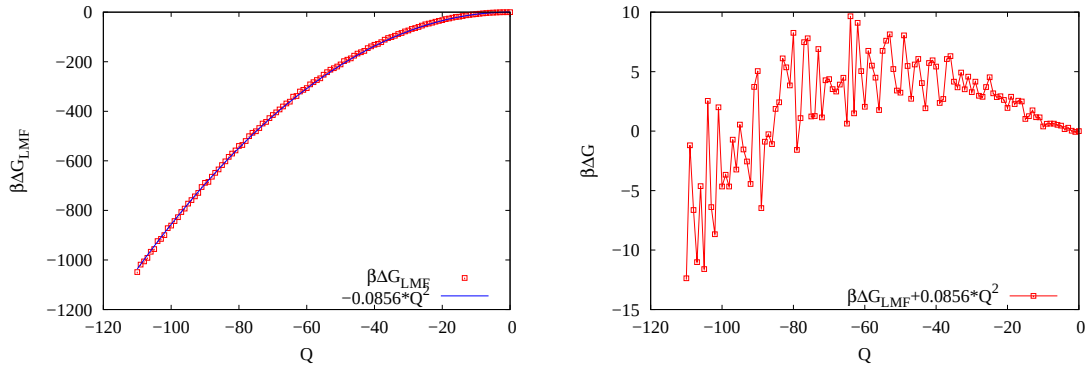

(a) (b)

Figure 5.5: (a) ΔG_{LMF} as a function of the colloid charge Q (red), and the quadratic fit of $\Delta G_{\mathrm{LMF}}(Q)$ (blue). (b) The error of the quadratic fit.

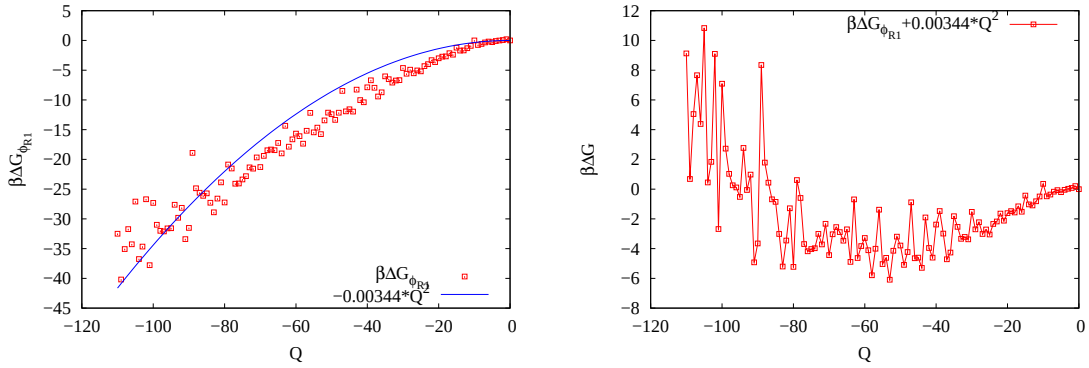

(a) (b)

Figure 5.6: (a) $\Delta G_{\phi_{R1}}$ as a function of the colloid charge Q (red), and the quadratic fit of $\Delta G_{\phi_{R1}}$ (blue). (b) The error of the quadratic fit.

model system we discussed in the last chapter. By dividing the solvation free energy into different parts, we were able to obtain the solvation free energy in the full system and our result is in good agreement with that in the full system. Moreover, because all of our simulations are performed in the short-ranged systems, it takes less CPU time to perform simulations than in the long-ranged full system. Finally we tried to fit the solvation free energy of charging to a quadratic function of the charge Q. Our fitting shows that the free energy of charging in the full system, $\Delta G_{\mathrm{charge}}$, can

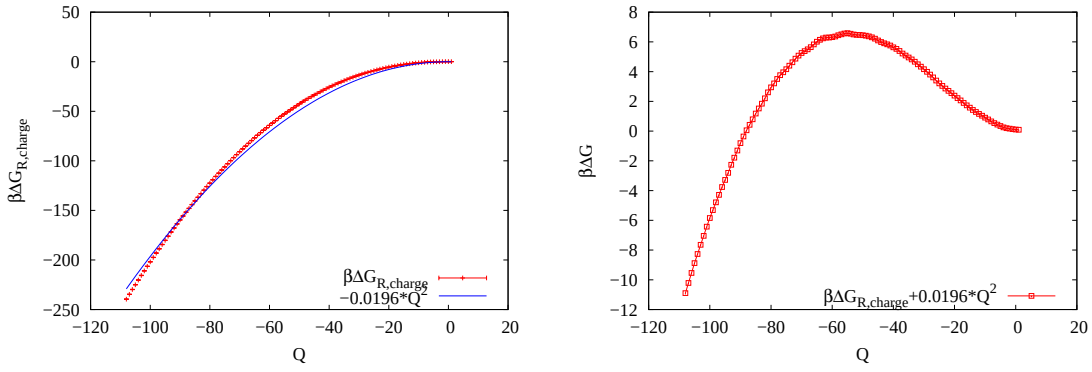

(a) (b)

Figure 5.7: (a) The free energy of charging $\Delta G_{\mathrm{R,charge}}$ in the short-ranged system as a function of the colloid charge Q (red), with error bars given, and the quadratic fit of $\Delta G_{\mathrm{R,charge}}(Q)$ (blue). (b) The error of the quadratic fit.

be fit to a quadratic function of Q not only in the weak coupling limit, where Q is small, but also in the case where the colloid is strongly charged. Moreover, by fitting $\Delta G_{\mathrm{R,charge}}$, $\Delta G_{\phi_{R1}}$ and ΔG_{LMF}, we find they all have quadratic dependence on the charge Q as well.

Chapter 6

Conclusions and Future Work

In this thesis, simulations are performed to study two nonuniform systems with different geometries.

The first system is amphiphiles (propionitrile and methanol, respectively) on a planar hydrophilic silica surface. The organization of amphiphiles at the hydrophilic surface is basically determined by the two competing forces: polar interactions between the molecules and the surface (via hydrogen bonding) and the packing of hydrocarbon groups (hydrophobic interactions). Our goal is to compare the simulation results with previous simulation of acetonitrile so as to see each specific group's influence on interfacial structure. Our simulation results for propionitrile show that hydrocarbon groups in the liquid/solid interface region are more closely packed than in acetonitrile, due to the extra methyl group in propionitrile molecule. This favorable hydrocarbon packing makes the liquid/solid interfacial structure quite different from that of acetonitrile in several aspects, such as dipole orientation and molecule density in interfacial sublayers. For the methanol/silica interface, serving as both H-bond donor and acceptor greatly enhanced the interaction between methanol and the silica surface, and this almost breaks up the bilayer-like structure observed at the acetonitrile/silica surface. Strong hydrogen bonding with the surface has also induced a series of effects, such as extremely slow reorientation dynamics, long H-bond

lifetime and screening of the dipole field from the silica surface.

Our simulation studies of amphiphile/silica systems are in qualitative agreement with nonlinear spectroscopy experiments performed at the interface. In fact simulations can do something more to interpret spectroscopy data. Recently we have calculated some time-correlation functions to study the reorientation effects in VSFG signals for acetonitrile at silica surface[89], and achieved very good agreement with experiments. Similar calculations for propionitrile are under way, and this time-correlation function study can be further extended to methanol as well.

Aside from density, orientation and time correlation functions, the dielectric permittivity $\underline{\epsilon}$ is also an interesting quantity to characterize interfacial structures. This is because if molecules are strongly bound to the surface, the dielectric relaxation would be slow and correspondingly the dielectric permittivity would be relatively small. Recently, dielectric permittivity for molecules in slab geometry has been calculated[90, 91] via simulations. It has been found that for water at a hydrophilic surface, the parallel component of the dielectric permittivity tensor, $\epsilon_{\parallel}$, is smaller than that of the hydrophobic surface, indicating slow dielectric relaxation in the direction parallel to the surface. In our spectroscopy experiments at the methanol/silica surface, very slow dielectric relaxation has also been observed[52, 92], therefore it would be interesting to calculate its dielectric permittivity and compare it with that of other interfaces.

The second system is a highly charged colloid with trivalent counterions and monovalent coions around it. The sign of total charge will be inverted inside the shear plane and this is called the "charge inversion". Our goal is to use the LMF

theory to fully reproduce its properties, including both structure and thermodynamics, in our short-ranged mimic system. Using SCA as a starting point, we can immediately capture overcharging by including most nearest neighbor correlations in SCA. Then using the linear response method, we can solve the LMF equation for the system in an efficient way and obtain the same structure as the full system. We also calculated the solvation free energy of the colloid by running simulations only in the short-ranged system, and our calculated solvation free energy is very close to that calculated in the full system but the whole calculation process is more computationally efficient. This again shows that as long as the LMF theory can obtain the correct structure, it will also give accurate results in thermodynamics.

However, some issues are still not quite clear in this charge inversion model system. We have calculated the free energy of charging the colloid from zero to Q and looked at its dependence on charge Q. Surprisingly, the free energy of charging, ΔG_{charge} can be fitted to a quadratic function $\Delta G_{\text{charge}}(Q) = CQ^2$, even when $|Q|$ is very large. This suggest that the free energy of charging might not heavily depend on the local charge distribution near the colloid, but may be largely determined by the long-ranged part of the charge density. Finding an expression for the fitting coefficient C might provide some helpful insight into this universal quadratic dependence.

Moreover, in Section 4.6.1, we have mentioned that greater fluctuations are observed in the full LMF system than that in the Ewald and we interpret this as a result of overdamped fluctuation in the Ewald system. This overdamping effect from image charges may drive the system quickly to the equilibrium value and may

suggest fast dynamics in the Ewald. Recently some TCFs have been constructed[93] and the calculation indeed shows that the TCFs of the Ewald system decay very fast. For the LMF theory, we plan to construct some similar TCFs to characterize its dynamics, which is likely to be slower. What the proper dynamics for a realistic non periodic system with Coulomb interactions is remains a challenging open question.

Appendix A

Stable k-space solution of LMF equation

This appendix depends partially on J. M. Rodger's Ph.D thesis[32] and a recent note by Prof. Weeks[94].

Consider the LMF equation for Coulomb systems, which has already been shown in Eq. (4.19)

$$\begin{aligned}\mathcal{V}_{R1}(\mathbf{r}) &= \frac{1}{\epsilon}\int d\mathbf{r}'\rho^{q}_{R,tot}(\mathbf{r}')\cdot v_1(|\mathbf{r}-\mathbf{r}'|) \\ &= \frac{1}{\epsilon}\int d\mathbf{r}'\rho^{q\sigma}_{R,tot}(\mathbf{r}')\cdot\frac{1}{|\mathbf{r}-\mathbf{r}'|},\end{aligned} \tag{A.1}$$

In k-space, where $\hat{f}(\mathbf{k})$ indicates the Fourier transform of $f(\mathbf{r})$ and our convention is to have $1/(2\pi)^3$ in the k-space to r-space transform, we may write the LMF equation (4.19) as

$$\hat{\mathcal{V}}_{R1}(\mathbf{k}) = \frac{1}{\epsilon}\hat{\rho}^{q}_{R,tot}(\mathbf{k})\exp\left(-\frac{k^2\sigma^2}{4}\right)\frac{4\pi}{k^2}. \tag{A.2}$$

For systems with spherical geometry the underlying difficulty of this equation is that when we have the correct $\mathcal{V}_R$ we expect

$$\hat{\rho}^{q}_{R,tot}(k) \approx 0 + \frac{b}{4\pi}k^2 + \mathcal{O}(k^4), \tag{A.3}$$

where the initial 0 arises from global neutrality. However, unless we have the correct $\mathcal{V}_R$, we instead may have

$$\hat{\rho}^{q}_{R,tot}(k) \approx C + \frac{b}{4\pi}k^2 + \mathcal{O}(k^4), \tag{A.4}$$

and this constant C causes iteration of the LMF equation in k-space to diverge. Even if one tries to integrate in r-space this long-ranged difficulty will likely show

up because $\mathcal{V}_{R1}(\mathbf{r})$ will not go to zero when r is large.

To get the iterative solution of the LMF equation to converge better, we can separate the Coulomb potential in the same way

$$\begin{aligned}\frac{1}{r} &= \frac{\mathrm{erfc}(r/l)}{r} + \frac{\mathrm{erf}(r/l)}{r} \\ &\equiv v_0^l(r,\sigma) + v_1^l(r,\sigma),\end{aligned} \tag{A.5}$$

where l is a parameter that is at the scale of σ that we use. Then we may rewrite the LMF equation (A.1) as

$$\begin{aligned}\mathcal{V}_{R1}(\mathbf{r}) &= \frac{1}{\epsilon}\int d\mathbf{r}'\rho_{R,\mathrm{tot}}^{q\sigma}(\mathbf{r}')[v_0^l(|\mathbf{r}-\mathbf{r}'|) + v_1^l(|\mathbf{r}-\mathbf{r}'|)] \\ &\equiv \mathcal{V}_{R1}^A(\mathbf{r}) + \mathcal{V}_{R1}^B(\mathbf{r}).\end{aligned} \tag{A.6}$$

The $\mathcal{V}_{R1}^A$ in real space could be rewritten as

$$\begin{aligned}\mathcal{V}_{R1}^A(\mathbf{r}) &= \frac{1}{\epsilon}\int d\mathbf{r}'\rho_{R,tot}^{q\sigma}(\mathbf{r}')v_0^l(|\mathbf{r}-\mathbf{r}'|) \\ &= \frac{1}{\epsilon}\int d\mathbf{r}'\rho_{R,tot}^{q}(\mathbf{r}')[v_1^\sigma(|\mathbf{r}-\mathbf{r}'|) - v_1^{\tilde{l}}(|\mathbf{r}-\mathbf{r}'|)],\end{aligned} \tag{A.7}$$

where $\tilde{l} = \sqrt{l^2+\sigma^2}$. Because of the short-ranged $v_0^l(r)$ in its expression, $\mathcal{V}_{R1}^A$ will not be sensitive to error in the charge density at large r.

Now look at $\mathcal{V}_{R1}^B$, in real space it is can be rewritten as

$$\mathcal{V}_{R1}^B(\mathbf{r}) = \frac{1}{l^3\pi^{3/2}}\int d\mathbf{r}'\mathcal{V}_{R1}(\mathbf{r}')\exp\left(-\frac{|\mathbf{r}-\mathbf{r}'|^2}{l^2}\right). \tag{A.8}$$

The Gaussian factor in Eq. (A.8) will decay very rapidly therefore $\mathcal{V}_{R1}^B$ will be zero for large r. Combining Eq. (A.7) and (A.8), now Eq. (A.6) can be written as

$$\begin{aligned}\mathcal{V}_{R1}(\mathbf{r}) = \frac{1}{\epsilon}\int d\mathbf{r}'\rho_{R,tot}^{q}(\mathbf{r}')\left\{\frac{\mathrm{erf}\left(\frac{|\mathbf{r}-\mathbf{r}'|}{\sigma}\right)}{|\mathbf{r}-\mathbf{r}'|} - \frac{\mathrm{erf}\left(\frac{|\mathbf{r}-\mathbf{r}'|}{\tilde{l}}\right)}{|\mathbf{r}-\mathbf{r}'|}\right\} \\ + \frac{1}{l^3\pi^{3/2}}\int d\mathbf{r}'\mathcal{V}_{R1}(\mathbf{r}')\exp\left(-\frac{|\mathbf{r}-\mathbf{r}'|^2}{l^2}\right).\end{aligned} \tag{A.9}$$

This is the "stable"iteration formula we are using. In practice, $\rho_{R,\mathrm{tot}}^q$ and $\mathcal{V}_{R1}$ from

the previous iteration will be inserted into the right hand side of Eq. (A.9) to obtain the $\mathcal{V}_{R1}$ for the next iteration. Such iteration will drive both $\rho^q_{R,\mathrm{tot}}$ and $\mathcal{V}_{R1}$ to self-consistency even if the initial $\rho^q_{R,\mathrm{tot}}$ is not correct.

Now we will consider another way of doing the stable iteration. Consider the $\mathcal{V}^B_{R1}$ in k space

$$\mathcal{V}^B_{R1}(\mathbf{k}) = \frac{1}{\epsilon}\rho^q_{R,\mathrm{tot}}(\mathbf{k}) e^{\frac{-k^2\sigma^2}{4}} e^{\frac{-k^2 l^2}{4}} \frac{4\pi}{k^2}. \tag{A.10}$$

For a $\rho^q_{\mathrm{R,tot}}(\mathbf{k})$ that obeys neutrality and has the correct form shown in Eq. (A.3), and the parameter l is large enough to ensure that only the quadratic term of the density expansion in Eq. (A.3) is important, then $\mathcal{V}^B_{R1}(\mathbf{k})$ can be approximated by

$$\mathcal{V}^B_{R1}(\mathbf{k}) \simeq \frac{b}{\epsilon} e^{\frac{-k^2\sigma^2}{4}} e^{\frac{-k^2 l^2}{4}} \frac{4\pi}{k^2}, \tag{A.11}$$

or in r-space

$$\mathcal{V}^B_{R1}(\mathbf{r}) \simeq \frac{b}{\epsilon} \frac{1}{\pi^{3/2}\tilde{l}^3} \exp\left(-\frac{r^2}{\tilde{l}^2}\right). \tag{A.12}$$

Then the formula for this stable iteration method can be written as

$$\mathcal{V}_{R1}(\mathbf{r}) = \frac{1}{\epsilon}\int d\mathbf{r}' \rho^q_{R,tot}(\mathbf{r}') \left\{ \frac{\mathrm{erf}\left(\frac{|\mathbf{r}-\mathbf{r}'|}{\sigma}\right)}{|\mathbf{r}-\mathbf{r}'|} - \frac{\mathrm{erf}\left(\frac{|\mathbf{r}-\mathbf{r}'|}{\tilde{l}}\right)}{|\mathbf{r}-\mathbf{r}'|} \right\}$$
$$+ \frac{b}{\epsilon}\frac{1}{\pi^{3/2}\tilde{l}^3} \exp\left(-\frac{r^2}{\tilde{l}^2}\right). \tag{A.13}$$

During the iteration process, $\rho^q_{R,\mathrm{tot}}$ and b from the previous iteration is inserted into the right hand side of Eq. (A.13), where b is determined by the $\mathcal{V}_{R1}(\mathbf{r})$ from the previous iteration

$$b = \epsilon \mathcal{V}_{R1}(\mathbf{k}=0) = \epsilon \int d\mathbf{r} \mathcal{V}_{R1}(\mathbf{r}). \tag{A.14}$$

This iteration method will also drive $\rho^q_{R,tot}$ and $\mathcal{V}_{R1}$ to self-consistency.

Bibliography

[1] F. Ding, Z. Hu, Q. Zhong, K. Manfred, R. R. Gattass, M. R. Brindza, J. T. Fourkas, R. A. Walker, and J. D. Weeks. Interfacial organization of acetonitrile: Experiment and theory. *J. Phys. Chem. C*, 114:17651–17659, 2010.

[2] S. R. Hatch, R. S. Dougal, and P. Rabinowitz. Surface vibrational spectroscopy of the vapor solid and liquid solid interface of acetonitrile on ZrO_2. *Chem. Phys. Lett.*, 196:97, 1992.

[3] S. R. Hatch, R. S. Dougal, and P. Rabinowitz. In-situ surface vibrational spectroscopy of the vapor solid and liquid-solid interface of acetonitrile on ZrO_2. *J. Vac. Sci. Tech.*, 11:2232, 1993.

[4] M. C. Henry, E. A. Piagessi, and M. C. Messmer. Sum-frequency observation of solvent structure at model chromatographic interfaces: Acetonitrile-water and methanol-water systems. *Langmuir*, 21:6521, 2005.

[5] Zhonghan Hu and John D. Weeks. Acetonitrile on silica surfaces and at its liquid-vapor interface: Structural correlations and collective dynamics. *J. Phys. Chem. C*, 114(22):10202–10211, 2010.

[6] B. J. Loughnane, R. A. Farrer, and J. T. Fourkas. Geometric effects in the dynamics of a nonwetting liquid in microconfinement: An optical kerr effect study of methyl iodide in nanoporous glasses. *J. Phys. Chem. B*, 102:5409–5412, 1998.

[7] B. J. Loughnane, A. Scodinu, R. A. Farrer, J. T. Fourkas, and U. Mohanty. Exponential intermolecular dynamics in optical kerr effect spectroscopy of small-molecule liquids. *J. Chem. Phys.*, 111:2686–2694, 1999.

[8] M. R. Strunk and C. T. Williams. Aliphatic nitrile adsorption on Al_2O_3 and ZrO_2 as studied by total internal reflection sum-frequency spectroscopy. *Langmuir*, 19:9210–9215, 2003.

[9] S. B. Waldrup and C. T. Williams. In situ investigation of acetonitrile adsorption on Al_2O_3-coated CaF_2 using sum-frequency spectroscopy. *J. Phys. Chem. B*, 110:16633, 2006.

[10] D. Zhang, J. Gutnow, and K. B. Eisenthal. Vibrational-spectra, orientations, and phase-transitions in long-chain amphiphiles at the air-wate-interface - probing the head and tail groups by sum-frequency generation. *J. Phys. Chem.*, 98:13729, 1994.

[11] D. Zhang, J. Gutnow, K. B. Eisenthal, and T. F. Heinz. Sudden structure-change at an air binary-liquid interface - sum frequency study of the air acetonitrile-water interface. *J. Chem. Phys.*, 98:5099, 1993.

[12] X. Zhu, Q. Zhong, and J. T. Fourkas. Orientational diffusion of n-alkyl cyanides. *J. Phys. Cond. Matt.*, 17:S4105, 2005.

[13] J. Zhang and J. Jonas. NMR study of the geometric confinement effects on the anisotropic rotational diffusion of acetonitrile-d3. *J. Phys. Chem.*, 97:8812–8815, 1993.

[14] B. J. Loughnane, A. Scodinu, R. A. Farrer, and J. T. Fourkas. Dynamics of a wetting liquid in nanopores: An optical kerr effect study of the dynamics of acetonitrile confined in sol-gel glasses. *J. Chem. Phys.*, 111:5116–5123, 1999.

[15] R. D. Mountain. Molecular dynamics study of thin water-acetonitrile films. *J. Phys. Chem. B*, 105:6556–6561, 2001.

[16] S. Paul and A. Chandra. Molecular dynamics study of the liquid-vapor interface of acetonitrile: Equilibrium and dynamical properties. *J. Phys. Chem. B*, 109:20558–20564, 2005.

[17] C. Morales and W. H. Thompson. Simulations of infrared spectra of nanoconfined liquids: Acetonitrile confined in nanoscale, hydrophilic silica pores. *J. Phys. Chem. A*, 113:1922–1933, 2009.

[18] T. S. Gulmen and W. H. Thompson. Grand canonical monte carlo simulations of acetonitrile filling of silica pores of varying hydrophilicity/hydrophobicity. *Langmuir*, 25:1103–1111, 2009.

[19] R. D. Mountain. Microstructure and hydrogen bonding in water-acetonitrile mixtures. *J. Phys. Chem. B*, 114:16460–16464, 2010.

[20] H. Bertagnolli, P. Chieux, and M. D. Zeidler. A neutron-diffraction study of liquid acetonitrile. *Mol. Phys.*, 32:1731–1736, 1976.

[21] H. Bertagnolli and M. D. Zeidler. Molecular pair-correlation function of liquid acetonitrile from X-ray and neutron-diffraction studies. *Mol. Phys.*, 35:177–192, 1978.

[22] F. Ding, Q. Zhong, K. Manfred, X. He, M. Brindza, R. A. Walker, and J. T. Fourkas. Structure of liquid propionitrile at interfaces. 2. experiment. *J. Phys. Chem. C*, 116:4019–4025, 2012.

[23] F. Brettschneider, V. Jankowski, T. Gnthner, S. Salem, M. Nierhaus, A. Schulz, W. Zidek, and J. Jankowski. Replacement of acetonitrile by ethanol as solvent in reversed phase chromatography of biomolecules. *J. Chromatogr. B*, 878:763 – 768, 2010.

[24] J. D. Weeks. Connecting local structure to interface formation: A molecular scale van der waals theory of nonuniform liquids. *Annu. Rev. Phys. Chem.*, 53:533–562, 2002.

[25] Y.-G. Chen, C. Kaur, and J. D. Weeks. Connecting systems with short and long ranged interactions: Local molecular field theory for ionic fluids. *J. Phys. Chem. B*, 108:19874–19884, 2004.

[26] Y.-G. Chen and J. D. Weeks. Local molecular field theory for effective attractions between like charged objects in systems with strong coulomb interactions. *Proc. Nat. Acad. Sci. (USA)*, 103:7560–7565, 2006.

[27] J. M. Rodgers, C. Kaur, Y. G. Chen, and J. D. Weeks. Attraction between like-charged walls: Short-ranged simulations using local molecular field theory. *Phys. Rev. Lett*, 97:097801, 2006.

[28] N. A. Denesyuk and J. D. Weeks. A new approach for efficient simulation of coulomb interactions in ionic fluids. *J. Chem. Phys.*, 128:124109, 2008.

[29] J. M. Rodgers and J. D. Weeks. Local molecular field theory for the treatment of electrostatics. *J. Phys.: Cond. Matt.*, 20:494206, 2008.

[30] J. M. Rodgers and J. D. Weeks. Interplay of local hydrogen-bonding and long-ranged dipolar forces in simulations of confined water. *Proc. Nat. Acad. Sci. (USA)*, 105:19136–19141, 2008.

[31] J. M. Rodgers and J. D. Weeks. Accurate thermodynamics for short-ranged truncations of coulomb interactions in site-site molecular models. *J. Chem. Phys.*, 131:244108, 2009.

[32] J. M. Rodgers. *Statistical Mechanical Theory for and Simulations of Charged Fluids and Water*. PhD thesis, University of Maryland, College Park, 2008.

[33] K. Katsov and J. D. Weeks. On the mean field treatment of attractive interactions in the nonuniform simple fluids. *J. Phys. Chem. B*, 105:6738–6744, 2001.

[34] K. Katsov and J. D. Weeks. Incorporating molecular scale structure into the van der waals theory of the liquid-vapor interface. *J. Phys. Chem. B*, 106:8429–8436, 2002.

[35] J. D. Weeks, R. L. B. Selinger, and J. Q. Broughton. Self-consistent treatment of repulsive and attractive forces in nonuniform liquids. *Phys. Rev. Lett.*, 75:2694–2697, 1995.

[36] D. Frenkel and B. Smit. *Understanding Molecular Simulation: From Algorithms to Applications*. Academic Press, New York, 2nd edition, 2002.

[37] A. Y. Toukmaji and J. A. Board. Ewald summation technique in perspective: A survey. *Comp. Phys. Comm.*, 95:73–92, 1996.

[38] R. R. Netz. Electrostatics of counter-ions at and between planar charged walls: From poisson-boltzmann to the strong-coupling theory. *Eur. Phys. J. E*, 5:557–574, 2001.

[39] A. G. Moreira and R. R. Netz. Simulations of counterions at charged plates. *Eur. Phys. J. E*, 8:33–58, 2002.

[40] J. Valleau, R. Ivkov, and G. Torrie. Colloid stability: The forces between charged surfaces in an electrolyte. *J. Chem. Phys.*, 95:520–532, 2000.

[41] A. Fernandez-Nieves, A. Fernandez-Barbero, F. J. de las Nieves, and B. Vincent. Ionic correlations in highly charge-asymmetric colloidal liquids. *J. Chem. Phys.*, 123:054905, 2005.

[42] A. Kubíčková, T. Křížek, P. Coufal, M. Vazdar, E. Wernersson, J. Heyda, and P. Jungwirth. Overcharging in biological systems: Reversal of electrophoretic mobility of aqueous polyaspartate by multivalent cations. *Phys. Rev. Lett.*, 108:186101, 2012.

[43] A. Y. Grosberg, T. T. Nguyen, and B. I. Shklovskii. Colloquium: The physics of charge inversion in chemical and biological systems. *Rev. Mod. Phys.*, 74:329–345, 2002.

[44] Y. Levin. Electrostatic correlations: from plasma to biology. *Rep. Prog. Phys.*, 65:1577–1632, 2002.

[45] S. Liu, Z. Hu, J. D. Weeks, and J. T. Fourkas. Structure of liquid propionitrile at interfaces. 1. molecular dynamics simulations. *J. Phys. Chem. C*, 116:4012–4018, 2012.

[46] S. H. Lee and P. J. Rossky. A comparison of the structure and dynamics of liquid water at hydrophobic and hydrophilic surfaces-a molecular dynamics simulation study. *J. Chem. Phys.*, 100:3334–3345, 1994.

[47] I.-C. Yeh and M. L. Berkowitz. Ewald summation for systems with slab geometry. *J. Chem. Phys.*, 111:3155–3162, 1999.

[48] M. L. Price, D. Ostrovsky, and W. L. Jorgensen. Gas-phase and liquid-state properties of esters, nitriles, and nitro compounds with the opls-aa force field. *J. Comput. Chem*, 22:1340–1352, 2001.

[49] W. Smith, C. Young, and P. Rodger. DL_POLY: Application to molecular simulation. *Mol. Simul.*, 28:385–471, 1996.

[50] A. M. Nikitin and A. P. Lyubartsev. New six-site acetonitrile model for simulations of liquid acetonitrile and its aqueous mixtures. *J. Comput. Chem.*, 28:2020, 2007.

[51] J. M. Rodgers, Z. Hu, and J. D. Weeks. On the efficient and accurate short-ranged simulations of uniform polar molecular liquids. *Mol. Phys.*, 109:1195–1211, 2011.

[52] D. Roy, S. Liu, A. R. Siler, B. L. Woods, J. T. Fourkas, J. D. Weeks, and R. A. Walker. Nonpolar adsorption at the silica/methanol interface: Surface mediated polarity and solvent density across a strongly associating solid/liquid boundary. submitted.

[53] C. Alba-Simionnesco R. Guegan, D. Morineau. Interfacial structure of an h-bonding liquid confined into silica nanopore with surface silanols. *Chem. Phys.*, 317:236–244, 2005.

[54] E. M. Dolores, J. Rodrigues, and D. Laria. Structure and dynamics of liquid methanol confined within functionalized silica nanopores. *J. Chem. Phys.*, 133:154707, 2010.

[55] E. M. Dolores, J. Rodrigues, and D. Laria. Liquid methanol confined within functionalized silica nanopores. 2. solvation dynamics of coumarin 153. *J. Phys. Chem. B*, 115:12859–12867, 2011.

[56] W. L. Jorgensen, D. S. Maxwell, and J. TiradoRives. Development and testing of the OPLS all-atom force field on conformational energetics and properties of organic liquids. *J. Am. Chem. Soc.*, 118(45):11225–11236, 1996.

[57] P. Ball. Water as an active constituent in cell biology. *Chem. Rev.*, 108:74–108, 2008.

[58] W. L. Jorgensen. Structure and properties of liquid methanol. *J. Am. Chem. Soc*, 102:543–549, 1980.

[59] M. Haughney, M. Ferrario, and I. R. McDonald. Molecular dynamics of liquid methanol. *J. Phys. Chem.*, 91:4934–4940, 1987.

[60] A. Luzar and D. Chandler. Effect of environment on hydrogen bond dynamics in liquid water. *Phys. Rev. Lett.*, 76:928–930, 1996.

[61] H. Tanaka Y. Tamai and K. Nakanishi. Molecular dynamics study of polymer-water interaction in hydrogels. 2. hydrogen-bond dynamics. *Macromolecules*, 29:6761–6769, 1996.

[62] Z. Hu and J. D. Weeks. Effective solutions of self-consistent mean field equations for dewetting and electrostatics in nonuniform liquids. *Phys. Rev. Lett.*, 105:140602, 2010.

[63] G. M. Torrie and J. P. Valleau. Electrical double-layers. 1. Monte-Carlo study of a uniformly charged surface. *J. Chem. Phys.*, 73:5807–5816, 1980.

[64] M. Lozada-Cassou, R. Saavedra-Barrera, and D. Henderson. The application of hypernetted-chain approximation to the electrical double-layer - comparison with monte-carlo results for symmetric salts. *J. Chem. Phys.*, 77:5150–5156, 1982.

[65] A. Diehl and Y. Levin. Smoluchowski equation and the colloidal charge reversal. *J. Chem. Phys.*, 125:054902, 2006.

[66] M. Quesada-Pérez, E. González-Tovar, A. Martín-Molina, M. Lozada-Cassou, and R. Hidalgo-Álvarez. Overcharging in colloids: beyond the poisson-boltzmann approach. *Chem. Phys. Chem.*, 4:234–248, 2003.

[67] V. I. Perel and B. I. Shklovskii. Screening of a macroion by multivalent ions: a new boundary condition for the poisson-boltzmann equation and charge inversion. *Physica A*, 274:446–453, 1999.

[68] B. I. Shklovskii. Screening of a macroion by multivalent ions: Correlation induced inversion of charge. *Phys. Rev. E*, 60:5802–5811, 1999.

[69] M. C. Barbosa S. Pianegonda and Y. Levin. Charge reversal of colloidal particles. *Europhys. Lett.*, 85:1568–1571, 2000.

[70] A. Yu. Grosberg T. T. Nguyen and B. I. Shklovskii. Macroions in salty water with multivalent ions: giant inversion of charge. *Phys. Rev. Lett.*, 85:1568–1571, 2000.

[71] R. Messina, E. Gonzá-Tovar, M. Lozada-Cassou, and C. Holm. Overcharging: the crucial role of excluded volume. *Europhys. Lett.*, 60:383–389, 2002.

[72] D. Antypov, M. C. Barbosa, and C. Holm. Incorporation of excluded-volume correlations into poisson-boltzmann theory. *Phys. Rev. E*, 71:061106, 2005.

[73] J. D. Weeks, D. Chandler, and H. C. Andersen. Role of repulsive forces in determining equilibrium structure of simple liquids. *J. Chem. Phys.*, 54:5237–5247, 1971.

[74] H. J. C. Berendsen, J. P. M. Postma, W. F. van Gunsteren, A. Dinola, and J. R. Haak. Molecular-dynamics with coupling to an external bath. *J. Chem. Phys.*, 81:3684–3690, 1984.

[75] D. A. McQuarrie. *Statistical Mechanics*. University Science Books, Sausalito, California, 3rd edition, 2006.

[76] F. H. Stillinger and R. Lovett. General restriction on distribution of ions in electrolytes. *J. Chem. Phys.*, 49:1991–1994, 1968.

[77] A. Pohorille, C. Jarzynski, and C. Chipot. Good practices in free-energy calculations. *J. Phys. Chem. B*, 114:10235–10253, 2010.

[78] S. Kullback and R. A. Leibler. On information and sufficiency. *Ann. Math. Statist.*, 22:79–86, 1951.

[79] J. D. Weeks. private communication, 2012.

[80] J. D. Weeks. External fields, density functionals, and the Gibbs inequality. *J. Stat. Phys.*, 110:1209–1218, 2003.

[81] J.-P. Hansen and I. R. McDonald. *Theory of Simple Liquids*. Academic Press, New York, 2nd edition, 2006.

[82] C. H. Bennett. Efficient estimation of free energy differences from monte carlo data. *J. Comp. Phys.*, 22:245–268, 1976.

[83] G. Hummer, L. R. Pratt, and A. E. Garcia. Free energy of ionic hydration. *J. Phys. Chem.*, 100:1206–1215, 1996.

[84] T. L. Beck, M. E. Paulaitis, and L. R. Pratt. *The Potential Distribution Theorem and Models of Molecular Solutions*. Cambridge University Press, Cambridge, 2006.

[85] G. Hummer, L. R. Pratt, and A. E. Garcia. Molecular theories and simulation of ions and polar molecules in water. *J. Phys. Chem. A.*, 102:7885–7895, 1998.

[86] T. L. Beck. Hydration free energies by energetic partitioning of the potential distribution theorem. *J. Stat. Phys.*, 145:335–354, 2011.

[87] R. W. Zwanzig. High-temperature equation of state by a perturbation method. I. nonpolar gases. *J. Chem. Phys.*, 22:1420–1426, 1954.

[88] R. Schulz, B. Lindner, L. Petridis, and J. C. Smith. Scaling of multimillion-atom biological molecular dynamics simulation on a petascale supercomputer. *J. Chem. Theory Comput.*, 5:2798–2808, 2009.

[89] S. Liu and J. T. Fourkas. Orientational time correlation functions for vibrational sum-frequency generation. 1. acetonitrile. *J. Phys. Chem. A*, 2012. to appear.

[90] S. Gekle D. J. Bonthuis and R. R. Netz. Dielectric profile of interfacial water and its effect on double-layer capacitance. *Phys. Rev. Lett.*, 107:166102, 2011.

[91] V. Ballenegger and J. P Hansen. Dielectric permittivity profiles of confined polar fluids. *J. Chem. Phys.*, 122:114711, 2005.

[92] A. R. Siler and R. A. Walker. Effects of solvent structure on interfacial polarity at strongly associating silica/alcohol interfaces. *J. Phys. Chem. C*, 115:9637–9643, 2011.

[93] N. A. Denesyuk and J. D. Weeks. unpublished, 2012.

[94] J. D. Weeks. unpublished, 2011.